Fall 2013

Design and analysis of an open-ended waveguide probe for material characterization

Matthew Alan Kempin

DESIGN AND ANALYSIS OF AN OPEN-ENDED WAVEGUIDE PROBE FOR

MATERIAL CHARACTERIZATION

by

MATTHEW ALAN KEMPIN

A THESIS

Presented to the Faculty of the Graduate School of the

MISSOURI UNIVERSITY OF SCIENCE AND TECHNOLOGY

In Partial Fulfillment of the Requirements for the Degree

MASTER OF SCIENCE IN ELECTRICAL ENGINEERING

2013

Approved by

Dr. Reza Zoughi, Advisor
Dr. Daryl Beetner
Dr. Kristen Donnell

ABSTRACT

Nondestructive evaluation of stratified (layered) composite structures at microwave and millimeter wave frequencies is of great interest in many applications where simultaneous determination of the complex dielectric properties and thicknesses of multiple layers is desired. Open-ended rectangular waveguide probes are effective tools for this purpose. The technique requires a full-wave electromagnetic model that accurately calculates the complex reflection coefficient as a function of frequency and material properties. Subsequently, this information is used in conjunction with the measured complex reflection coefficient to evaluate the sought for material properties. This thesis presents simulated and measured data to investigate the influence that measurement system noise, which contaminates the measured complex reflection coefficient, has on estimating material properties. It will be shown however, that the foremost contributor to errors in estimating material properties is not due to system noise, but rather, is due to an inconsistency between the electromagnetic model and the measurement setup. More specifically, the electromagnetic model assumes an infinite waveguide flange while measurements are conducted using a finite-size flange. Consequently, the results of the model and those from measurements may not be sufficiently alike for accurate dielectric property and thickness evaluation. The work presented here investigates the effect of using an open-ended waveguide with a standard finite-sized flange on the error in evaluating the complex dielectric properties of a composite structure. Additionally, the design of a novel flange that markedly reduces this undesired effect by producing very similar electric field properties, at the flange aperture, to those created by an infinite flange will be presented and verified in measurement.

ACKNOWLEDGMENTS

TABLE OF CONTENTS

LIST OF ILLUSTRATIONS

LIST OF TABLES

1. INTRODUCTION

In the past two decades, complex composite structures have been increasingly utilized in a wide variety of applications involving civil structures, surface transportation, and space/aerospace vehicles, to name a few [1]-[6]. Consequently, the capability to accurately and non-invasively characterize and evaluate composite material properties (i.e. dielectric, magnetic and geometrical properties) has become essential to areas such as manufacturing quality control and life-cycle monitoring of composite structures. Microwave and millimeter-wave frequencies of the electromagnetic spectrum lend themselves well to making these material property measurements. This is due to their ability to penetrate into composite structures as well as their sensitivity to complex dielectric and magnetic materials properties [7].

Once the dielectric properties of a material are known, they may be directly related to its physical and chemical properties through the use of dielectric mixing models [8]-[10]. For example, [11] has shown that for polymer composites, the porosity level and the dielectric constant have a nearly linear relationship. Therefore, if the dielectric constant can be accurately obtained, an accurate estimation of the porosity of the composite material may also be made. Next, it has been shown that due to the dielectric properties of rust/corrosion, it is possible to detect and evaluate the severity of corrosion under a layer(s) of a composite material(s) [12]-[13]. This ability is particularly important in the aerospace industry for the detection of corrosion underneath thin layers of paint. Another example is the detection of a disbonded layer in a composite structure such as an aircraft radome [1]. A disbond introduces an unintended layer of air (or pockets of air) into the composite structure which may risk the structural or operational integrity of the radome. This layer of air changes the dielectric properties of the structures, which may be detected via measurement techniques. Finally, the dielectric properties of concrete and mortar have been shown to be related to the free chloride content as well as water distribution and its temporal movement in the material [14]-[17]. The ability to detect chloride levels is important as chloride intrusion can initiate corrosion and depassivation of the steel reinforcements inside the material. In addition,

evaluation of the water distribution in cement-based materials is essential for evaluating the curing and long-term performance of the material.

The complex relative dielectric constant is defined as ($\varepsilon_r = \varepsilon_r' - j\varepsilon_r''$), where ε_r' is the relative permittivity and ε_r'' is the relative loss factor. The relative permittivity indicates the ability of a material to store energy in an electric field (relative to that of free-space), while the loss factor indicates the ability of the material to absorb electromagnetic energy. The term $-j\varepsilon_r''$ must always be less than zero to satisfy the conservation of energy [18]. The loss in a material may also be expressed as the ratio between the loss factor and the relative permittivity, denoted as the loss tangent ($\tan\delta = \frac{\varepsilon_r''}{\varepsilon_r'}$). The magnetic property of a material, namely, the complex relative permeability may be defined in a similar manner ($\mu_r = \mu_r' - j\mu_r''$), where μ_r' is the relative (to free-space) permeability, and μ_r'' is the magnetic loss factor [18]. However, since the majority of dielectric materials are non-magnetic, it will be assumed in this thesis that $\mu_r' = 1$ and $\mu_r'' = 0$. It is important to note that both the dielectric constant and the relative permeability are functions of frequency. In addition, the dielectric constant is a macroscopic quantity that can be described as a weighted average of the individual constituents present in a material (assuming the wavelength is much larger than the size of the dielectric constituents). Therefore, if the ratio of the constituents in a material changes or a new constituent is introduced, the dielectric constant will also change [9].

A number of techniques have been developed to determine the complex dielectric constant of materials. These techniques vary in their implementation approaches (e.g., destructive vs. nondestructive), the accuracy by which various parameters may be determined, and their applicability to the geometry of a particular material (e.g., extended infinite half-space vs. sheet materials that may be cut to place inside of a waveguide) [8], [19]-[22]. For instance, the loaded transmission line technique involves cutting and shaping a sample to precisely fit inside either a coaxial line or a waveguide. Subsequently, a broadband measurement of the scattering parameters for the loaded transmission line is made via a vector network analyzer (VNA), and from the scattering parameters, the material properties may be retrieved [19], [21]. A major advantage to using a coaxial line is its ability to sustain transverse electromagnetic (TEM) waves from

DC to relatively high frequencies. However, it is challenging to machine a sample to precisely fit the geometry of a coaxial line. Consequently, any small air gap between the dielectric and the coaxial line conductors creates a discontinuity in the radial electric field which introduces a significant measurement uncertainty [19], [21]. Using a loaded waveguide sacrifices some bandwidth for simplifying the shape of the sample under test (SUT) as well as decreasing the severity of the consequences of slight air gaps [23]. It is assumed that only the dominant waveguide mode propagates; however, any inclusion, machining error, or non-uniformity of the sample will couple energy to higher-order modes and introduce uncertainty in the measurement. Regardless, the loaded transmission line technique can achieve very good accuracies (assuming a good fit of the SUT) and evaluate the complex dielectric constant as function of frequency. However, this technique requires the SUT be machined to fit a specific geometry [19], [21].

The most accurate measurement techniques for evaluating the complex dielectric constant of a material are resonance techniques [21], [23]. However, the materials being evaluated must be relatively low loss so as to promote resonant behavior inside the cavity or dielectric resonator. One of the most frequently used techniques employs a cylindrical cavity operating in the TE_{011} mode while the SUT is shaped to be a thin cylindrical disc. This technique conveniently places the SUT so that any air gaps between the dielectric and the cavity are parallel to the electric field. Due to the electric field continuity across the dielectric/air boundary, the errors introduced by the air gaps are minimized [21], [23]. An electromagnetic model is necessary to evaluate the material properties of the SUT. A common approach is the perturbation technique which assumes that the introduction of a small dielectric sample minimally affects the field setup inside the cavity. Consequently, the fractional change in the resonant frequency can then be related to the introduced material properties. The major drawback to cavity techniques comes from the requirement of specific, precise sample geometries, samples that are homogenous (typically cannot evaluate layered structures), and evaluation of the dielectric properties at a single frequency. In addition to cavities, dielectric resonators have also shown utility in material characterization. Instead of using a conductive cavity to contain the electromagnetic energy, the dielectric sample itself contains the energy. An example is described by a cylindrical SUT with parallel conducting plates "capping" the two ends of

the cylinder. The TE_{011} mode is excited in the dielectric and, due to its tightly bound field structure, more than 90% of the energy is held in the dielectric [23]. It is important that the energy be held in the dielectric structure so that the interaction between the electromagnetic fields and the dielectric material is maximized. Other dielectric resonator structures are also used; however, they depend on numerical techniques for evaluation as there are not closed form solutions to Maxwell's equations describing the fields within the dielectric resonators [23]. However, dielectric resonators suffer from the same drawbacks as do cavity resonators.

Another group of measurement techniques are free-space measurements. These measurements are performed in free space using two antennas. The transmission and/or reflection coefficients (scattering parameters) are measured with the two antennas facing one another and the sample placed between the antennas. It is required that the sample be planar with its size larger than the antenna beam widths. This size requirement is to minimize diffracted/scattered fields at the edges of the sample [24]. However, electromagnetic fields typically diverge from an aperture antenna (e.g. horn antenna), thus, the necessary sample size may be very large. To overcome this requirement, dielectric lenses or concave mirrors are commonly used to focus the radiated fields [23]. An assumption is typically made that the fields incident on the sample are planar although they are more correctly defined with a spherical wave front. Due to this assumption along with disregarding the finite sample size and difficulty in calibration, the accuracy capabilities of this technique are severely limited [21].

Lastly, there are open-ended transmission line techniques. First is the open-ended coaxial line. In this technique, a coaxial aperture is cut into an infinite ground plane and the aperture is pressed against a planar SUT [21], [25]. A VNA is used to measure the reflection coefficient (S_{11}) which is a function of the complex dielectric constant, complex permeability, and thickness of each layer in a generally layered structure. The layered structure may be terminated into either an infinite half-space or a conductor. In order to evaluate the complex relative dielectric properties and thickness of one or more layers, a robust full-wave electromagnetic model describing the interaction between the electromagnetic waves and the composite structure is required. This electromagnetic model may be computationally intensive [25]. A drawback of this technique is the

inefficiency of the aperture radiation, making the measurement only sensitive to the material layers that are very near aperture. This is due to the tightly bound incident TEM waves which produce a strong wave impedance mismatch at the aperture. As a result, much of the incident energy is reflected as opposed to radiated into the material. Consequently, the illuminating field away from the aperture may be very weak which reduces the sensitivity of the measurement [25].

Finally, the open-ended waveguide technique may be used for material characterization purposes [1]-[2], [7], [22], [26]-[27]. The waveguide generally has a rectangular or circular cross-section due to the closed form of their modal solutions. It is assumed that the waveguide aperture is cut into an *infinite ground plane* or *flange* and is radiating into a generally planar, stratified composite structure which is terminated in either a conductor or an infinite half-space. The complex reflection coefficient, which is a function of the properties (electric, magnetic, and geometrical) of each layer in the structure is measured [28]. Like the open-ended coaxial case, a robust full-wave electromagnetic model of the wave interaction with the structure is required to evaluate the material characteristics of a layer(s) in the composite structure. This method is more robust than an open-ended coaxial line as it more efficiently radiates energy into the structure, which allows for penetration into thicker and higher loss structures. The biggest advantage of using the open-ended waveguide technique is its non-invasive nature as the SUT need not be cut or shaped to fit inside a transmission line or cavity. In addition, it can be used to simultaneously evaluate the properties of multiple layers in a structure with an arbitrary number of layers and either a conductor or an infinite half-space backing [29]. Lastly, it provides an accuracy improvement over the free space method using two focused antennas and the open-ended coaxial method thanks to its superior radiation capabilities.

The goal of the investigation presented here is to further develop an understanding of the sensitivity of the open-ended rectangular waveguide technique as it pertains to measurement noise. In Section 2, an overview of the technical aspects of using the open-ended waveguide technique for material characterization is presented. In Section 3, an effort is made to quantify the advantage gained by using high end measurement equipment as opposed to cheaper, noisier alternatives. Simulated data is presented to

show the effect that complex Gaussian noise (at varying power levels), introduced into the reflection coefficient, has on the evaluated material properties. In addition, measurements made using an Agilent 8510C VNA and a VNA made in-house for a substantially lower cost are compared.

However, in Section 4 it will be shown that the foremost contributor to error in both the measured complex reflection coefficient and the evaluated material properties is not caused by measurement noise, but rather by the assumption of an infinite ground plane in the electromagnetic model, as presented in [28], [30]. This is contrasted by measurements which are made using a finite-sized, standard waveguide flange as the ground plane. The edges of the waveguide flange introduce a discontinuity thereby causing the radiated electromagnetic fields to be partially reflected, an effect that is not accounted for in the model [30]. The effect of different material types (i.e. low loss versus high loss) and different material backings (i.e. conductor-backed versus infinite air half-space) on the errors introduced by the finite-sized flange will be evaluated.

In Section 5 a modification to the geometry of a standard waveguide flange is presented that markedly improves the accuracy of the open ended waveguide technique [30]. This improvement is accomplished by more closely matching the surface current density on the probe and the electric field directly in front of the waveguide aperture to that of an infinite flange (as is assumed in the electromagnetic model). This improvement can be obtained by modifying the standard, 90°-edges on the flange with a more gradual function such as a linear, circular, or elliptical taper.

2. MATERIAL CHARACTERIZATION USING THE OPEN-ENDED WAVEGUIDE TECHNIQUE

2.1. INTRODUCTION

The open-ended waveguide is a very attractive tool for NDT&E (nondestructive testing and evaluation) applications partially due to its ability to non-invasively evaluate the material characteristics (i.e., dielectric and geometrical properties) of a single layer or multiple layers in a composite structure [1]-[2], [7], [22], [27]-[28]. As mentioned earlier, the SUT does not need to be cut or shaped to fit inside a specific geometry. Moreover, only one side of the sample needs to be accessible since this technique involves only a reflection measurement. This is another attractive feature of this measurement technique which, for example, allows structures such as an aircraft fuselage and an aircraft radome to be evaluated in the field without being removed from its assembly. In addition, when evaluating the complex dielectric constant of a material, this technique is capable of providing it as a function of frequency [28]. However, this technique suffers from accuracy degradation when compared with completely-filled transmission line techniques. The susceptibility of the measurement accuracy to noise has not been rigorously investigated. Furthermore, it will be shown that an error is introduced by assuming the interrogating waveguide is terminated by an infinite flange in the electromagnetic model [28]. These topics will be discussed in more detail in following sections.

Measurements using the open-ended waveguide technique are typically easy to perform. The measurement setup is straightforward and simple although it should be tediously inspected because non-ideal effects such a waveguide aperture that is not exactly parallel to or flat against the sample can have significant effects on the measurements. The sample under test should be planar, or at least locally planar, and may be a generally stratified composite structure with an arbitrary number of layers. The structure may be terminated by either an infinite half-space or a conductor-backing. A schematic of an open-ended rectangular waveguide radiating into a generally layered composite structure can be seen in Figure 2.1 [28].
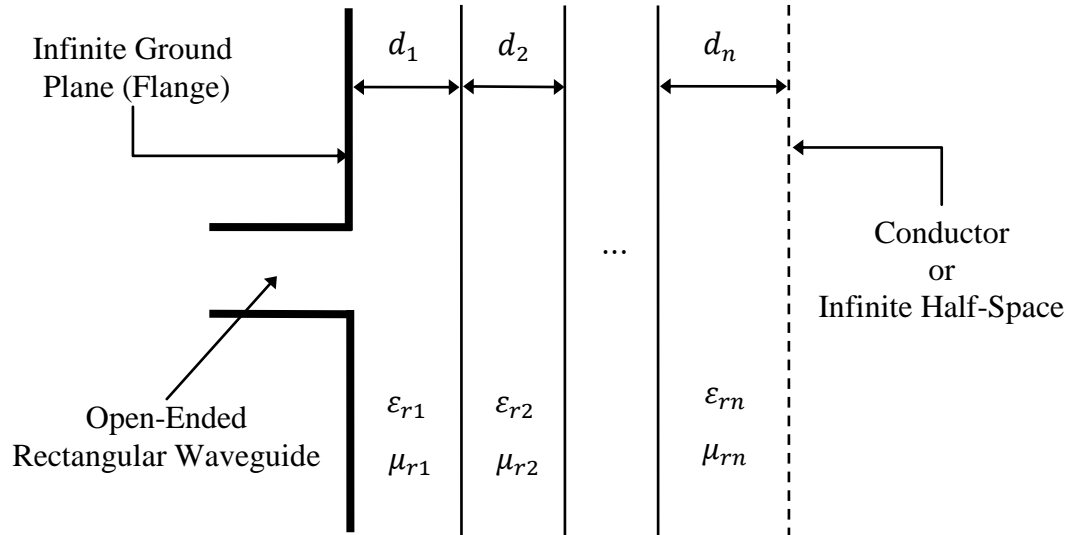
Figure 2.1. Schematic of open-ended waveguide radiating into an arbitrary layered structure.

2.2. ELECTROMAGNETIC MODEL

In order to evaluate the complex relative dielectric properties and thickness of one or more layers in a composite structure, a full-wave electromagnetic model that accurately describes the interaction between the open-ended rectangular waveguide and the structure is required. The results of the model must accurately match those measured, for example, by a VNA. This is commonly referred to as the forward model [30]. Such a comprehensive model was recently developed [28] by expanding a previous model [2] to account for higher-order modes that are generated at the waveguide aperture. The technique to include higher-order modes is described in [22] but is extended include a generally layered structure as opposed to a dielectric infinite half-space. The electromagnetic model presented in [28] has been employed in this study. A brief discussion of the strategy to develop the analytical formulation will be presented here. For more detail or exact expressions the reader is directed to [28].

This model employs Fourier analysis [22], [31] to develop an exact solution for the reflection coefficient at a rectangular waveguide aperture that is cut into an infinite ground plane and radiates into a generally layered structure. In order to construct an

analytical solution, it was first assumed that the incident electric field is in the form of the dominant waveguide TE$_{10}$ mode [28]. This is an accurate assumption as standard waveguide frequency bands and dimensions are chosen to allow propagation of only the TE$_{10}$ mode (higher-order modes in the waveguide are evanescent) [32]. Next, a general solution for the reflected fields in the waveguide, as well as the transmitted and reflected fields inside the dielectric structure, is constructed in the form of electric and magnetic Herztian potentials. The reflected waves in the waveguide are in the form of an infinite summation, using higher-order waveguide modes as basis functions. The transmission and reflection coefficients between each dielectric layer are recursively evaluated, starting from the last layer which assumes either no reflection (infinite half-space) or total reflection (perfect electric conductor). By enforcing the continuity of the tangential electric and magnetic fields at the aperture of the waveguide, a system of linear equations is formed to determine the complex amplitude coefficients for each waveguide mode.

The system of linear equations resulting from the process described above and shown in [28] becomes very cumbersome and is not repeated here. It can be seen however, that the reflection coefficient is a function of the thickness and complex dielectric constant of each layer in the SUT, the operating frequency, and the size of the waveguide aperture [28]. In addition, the material properties are embedded multiple times inside non-invertible integrals and consequently cannot be directly evaluated through inversion algorithms. This means that although the exact reflection coefficient for a given composite structure may be calculated, the model cannot be used in the opposite (inverse) fashion. For a given reflection coefficient, the material parameters cannot be directly evaluated.

2.3. EVALUATION OF MATERIAL PARAMETERS

In order to use this electromagnetic model to determine material properties from a measured reflection coefficient, an optimization algorithm may be incorporated to form a forward iterative solver that is used to retrieve the unknown layer(s) material properties or thicknesses [22], [28]-[29]. This process is accomplished by constructing a cost-function that compares the measured reflection coefficient with that predicted by the full-wave electromagnetic model. The parameters being sought for (as defined by the user)

are then varied from an initial guess value that is supplied by the user, according to the optimization algorithm (e.g. conjugate gradient descent [29]). The choice of the initial guess value will be discussed later. As the parameters are changed, the reflection coefficient is recalculated for each parameter value until the cost-function reveals that the difference between the measured reflection coefficient and that calculated by the model is below a user defined tolerance level. A flow diagram of the optimization process can be seen in Figure 2.2. In this endeavor, the MATLAB® function *fminsearch* [33] was used almost exclusively as the optimization algorithm.
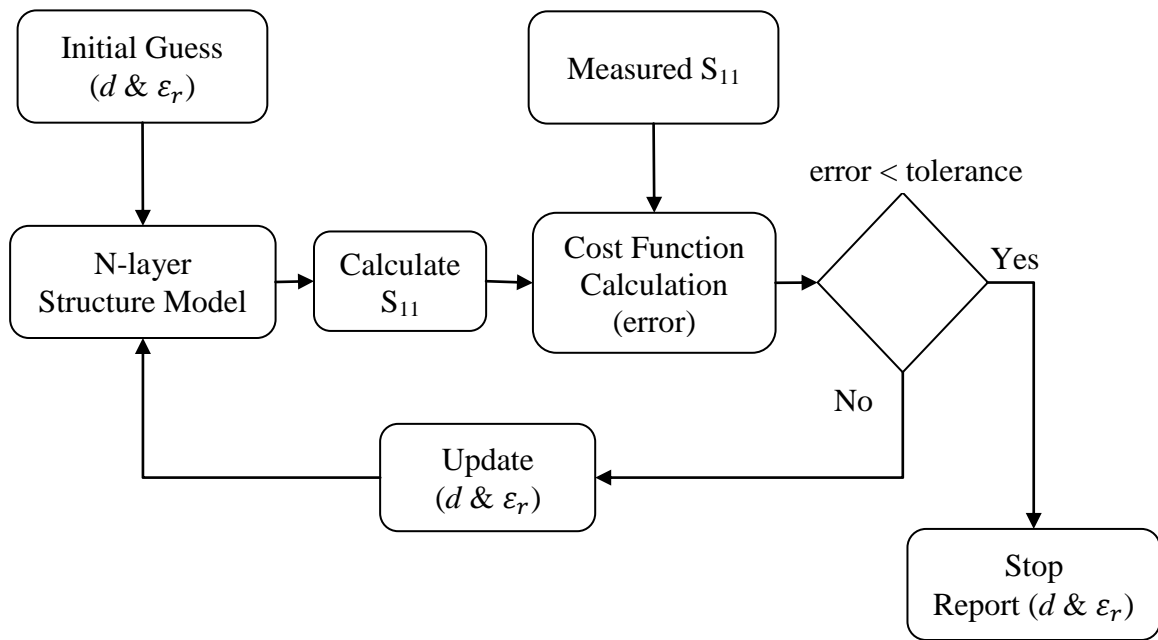
Figure 2.2. Flow chart of the optimization process to evaluate material properties given a reflection coefficient.

This optimization process can be performed to solve for the properties of an arbitrary number of layers simultaneously. Moreover, it can be performed for an arbitrary number of frequencies. There are two distinct options when defining the cost-function with respect to how the operating frequency is used. First, the sought-for parameters may

be evaluated as functions of frequency [28]-[29]. Doing so means that at each discrete frequency, the optimization process is performed and the material properties are evaluated independent of the results at all other frequencies. This cost-function can be written:

$$F = \left| \Gamma_m \left(f_i, d, \varepsilon_r, \mu_r \right) - \Gamma_c \left(f_i, d, \varepsilon_r, \mu_r \right) \right|^2 \tag{1}$$

where, f_i is the discrete frequency point, d is the layer(s) thickness(es), Γ_m is the measured reflection coefficient and Γ_c is the calculated reflection coefficient. The second option is to assume that material properties (complex dielectric constant) are constant as a function of frequency [28]. This cost-function can be written:

$$F = \frac{1}{N_f} \sum_{i=1}^{N_f} \left| \Gamma_m \left(f_i, d, \varepsilon_r, \mu_r \right) - \Gamma_c \left(f_i, d, \varepsilon_r, \mu_r \right) \right|^2 \tag{2}$$

where, N_f is the number of discrete frequency points in the reflection coefficient. Using this cost-function evaluates the fit of the calculated reflection coefficient to the measured reflection coefficient, while assuming material properties that are constant with respect to frequency. This is an advantageous approach when working with complex structures (i.e., multilayer composites). When many layers are present, the solution landscape (error values as the sought for parameters form an n-dimensional solution space where n is the number of parameters being evaluated) for a material property may contain many sharp local minima. By assuming constant parameters and leveraging the frequency diversity of the measurement, the solution landscape may be simplified by this approach (i.e., becomes more smooth) significantly [28].

The optimization process can have many other subtle complications. Since there is only one equation linking the reflection coefficient with the material parameters; when solving for more than one material property, the system becomes underdetermined. In cases such as these, taking advantage of the frequency diversity of the measurement has

proven to be very useful. Using the frequency diversity introduces N_f independent equations that can be used to yield a more accurate result [28].

A question that must be considered when employing an optimization algorithm deals with how to select the initial guess of a parameter value. In general, the answer to this question is case dependent. Most importantly, it depends on what type of information can be known about the structure or material being tested. For instance, in a structural health monitoring scenario, it is assumed that the properties of the ideal, virgin structure are available. In this case, these values may be used as the initial guess values, and if the structure has begun to degrade in its physical or chemical properties, the evaluated parameters will reflect this change. If the parameters of the structure or material are unknown, an educated guess may be made via a dielectric mixing model [9]-[10] and it is recommended to first assume the material properties are constant functions of frequency. Subsequently, the result of the static optimization procedure may be used as the initial guess when assuming the properties are functions of frequency [28].

Another property that can play a large role in the accuracy of the evaluated parameters is the number of modes that are assumed to be generated at the waveguide aperture. It was previously explained that the electromagnetic model produces an infinite summations of generated waveguide modes. The energy coupled into the higher-order modes at the aperture is highly dependent on the structure, as explained in [28]. In addition, it has also been shown that six modes is generally enough to produce negligible errors in the reflection coefficient [22], [28]. This assumption is used unless otherwise stated. The only exceptions are made for complex structures containing many thin, low loss layers that require extreme accuracy to provide meaningful results.

The optimization technique to evaluate material properties outlined here can be a very powerful tool, if used correctly. It is important to understand the electromagnetic model and what assumptions are made along with why a specific number of modes are necessary. The next step in this work will be to evaluate how noise in the measured reflection coefficient affects the accuracy with which parameters may be evaluated. Simulated data will be shown in which the forward electromagnetic model is used to generate the exact reflection coefficient, for a given structure. Next, complex Gaussian noise at varying power levels is injected into the reflection coefficient to simulate

measurement noise. Finally, material characteristics will be evaluated from the noisy reflection coefficient, providing insight into the extent to which noise degrades the property estimates. Furthermore, measured data will be shown comparing a high quality Agilent 8510C VNA with a more cost effective, in-house built VNA that has inferior noise performance.

3. OPEN-ENDED WAVEGUIDE TECHNIQUE AND SYSTEM NOISE

3.1. INTRODUCTION

In the previous sections, the open-ended waveguide technique for material characterization was introduced. Due to the nondestructive nature of this technique, it is versatile and applicable to many NDT problems. However, the effect of system noise, which contaminates the measured reflection coefficient, on the evaluated material properties has not been thoroughly evaluated. Consequently, the effect of system noise will be investigated here. In order to accomplish this, simulations will be presented in which the calculated reflection coefficient, generated by the forward electromagnetic model, is contaminated with varying noise power levels. The noise is assumed to follow a zero mean complex Gaussian (normal) distribution. Finally, the iterative optimization technique, which was outlined in Section 2, is employed to evaluate the material characteristics. Due to the stochastic nature of the injected noise, this process was repeated until the change in the mean value and standard deviation of the evaluated material properties converged to a specified tolerance level.

Subsequently, measurements will be presented to compare with these simulations. First, an Agilent 8510C VNA was used to measure the complex reflection coefficient of a sample. By cascading a rotary-vane waveguide attenuator between the VNA port and the open-ended waveguide, the dynamic range capabilities of the VNA could be controlled. In addition, an in-house built, non-coherent VNA will be compared with an Agilent 8510C VNA, comparing their accuracies in evaluating material properties. Finally, it will be shown that the dominating factor in material evaluation errors is not due to random system noise, but rather the effect of using a finite-sized waveguide flange when making reflection coefficient measurements.

3.2. SIMULATION OVERVIEW

3.2.1. Assumption of Gaussian Noise Distribution. The complex reflection coefficient, measured at the aperture of the waveguide, is a function of the operating

frequency as well as the material properties of the sample being evaluated. The measured reflection coefficient may be written as:

$$\Gamma_m\left(f_i,d,\varepsilon_r\right)=\Gamma_c\left(f_i,d,\varepsilon_r\right)+\gamma_i \tag{3}$$

where Γ_m is the measured reflection coefficient, Γ_c is the actual value of the reflection coefficient (i.e. calculated using the forward electromagnetic model where the waveguide flange is assumed to have infinite spatial extent), f_i represents the discrete operating frequencies, d is the dielectric thickness, ε_r is the complex dielectric constant, and γ_i is the noise/uncertainty contaminating the reflection coefficient measurement for the ith frequency. These uncertainties include discrepancies in the nominal values of the dielectric constants and material thicknesses along with system noise and calibration errors [5], [28]. Since these uncertainties are typically independent of one another and the system noise is generated from a collection of small events [34], their joint probability distribution may be modeled by a complex Gaussian distribution. This assumption is supported by the central limit theorem [5], [35].

3.2.2. Simulation Procedure. Simulations were constructed to investigate the effects of system noise, which contaminates the measured complex reflection coefficient, on the uncertainty associated with evaluated material properties. First, given the geometrical and electrical properties of a dielectric structure, the electromagnetic model [28] was used to calculate the actual complex reflection coefficient vector, $\mathbf{\Gamma_c}$, for N discrete frequency. Next, a complex noise vector defined by:

$$z_i = x_i + jy_i \tag{4}$$

with:

$$i \in \left\{1,2,\ldots,N\right\} \tag{5}$$

is generated with $x_i, y_i \in \mathbb{R}$ where $\mathbb{R}$ denotes the set of real numbers. In addition, it is assumed that x and y are independent variables and each follow a zero mean Gaussian (normal) distribution. Finally, the variance of x and y are assumed to be equal. This creates a circularly symmetric complex normal distribution whose relation matrix is zero and the covariance matrix is simply:

$$\Sigma(z) = \sigma^2 \mathbf{I} \tag{6}$$

Where $\mathbf{I}$ is the identity matrix and σ^2 is the variance. Consequently, the variance was chosen to be:

$$\sigma^2 = \frac{N_p}{2} \tag{7}$$

for each dimension, so that the total power in the complex noise vector is N_p. The noise power (N_p) that was added to the reflection coefficient was calculated with respect to the maximum reflection coefficient (magnitude of 1). By adding the noise with respect to the maximum refection coefficient, it simulates the effect of a measurement system's noise floor or the finite sensitivity of the receiver. It is also possible to select the noise power level for a specific signal-to-noise ratio. However, the former is more conducive to the simulations shown here as it more closely emulates the effect of different measurement systems having varying levels of dynamic range. In addition, it can be used to evaluate the effects of different measurement settings. For instance a typical VNA allows trade-offs to be made between measurement time and the noise floor level by optimizing settings such as the intermediate frequency (IF) bandwidth or the number of individual measurements that are averaged. An example that will be investigated here is a comparison between an Agilent 8510C VNA and a less expensive and simpler one-port reflectometer [36]. The reflectometer has a significant cost advantage; however, due to its simplified non-coherent detection architecture, it sacrifices system dynamic range and exhibits a higher noise floor.

Once the noise vector has been constructed, it is added to the calculated reflection coefficient to create the (simulated) measured reflection coefficient, Γ_m. Finally, the

forward-iterative optimization technique is invoked to evaluate material properties. Due to the stochastic nature of the noise vector, this process should be repeated in order provide a better estimate of the uncertainty introduced by the pseudo-system noise. Each repetition of this process is referred to as a trial, T. A block diagram depicting this process can be seen in Figure 3.1. In addition, a simulated example for Γ_m can be seen in Figure 3.2. The green dot in the center of the figure corresponds to the actual value of the reflection coefficient for the given structure and operating frequency. The "simulated" measurements for 1000 trials and three different noise power levels have also been plotted and are distributed around the actual value with circular contours of equal probability with a probability density function represented by:

$$ f\left(\Gamma_m; \mu, \Sigma\right) = \frac{1}{\pi N_p} exp\left[-\frac{\left|\Gamma_m - \Gamma_c\right|^2}{N_p} \right] \tag{8} $$

3.2.3. Simulation Results. In order to test the efficacy of this method, a thick, conductor-backed structure was evaluated. The noise power was assumed to be -60 dB which can be achieved using a VNA such as the Agilent 8510C. In literature, it has been previously shown through extensive measurements that low-loss and conductor-backed materials create the most significant measurement errors [28]. Consequently, the first simulation was performed for a conductor-backed dielectric sheet being interrogated by a WR-90 waveguide (22.86 mm x 10.16 mm) at 101 discrete frequency points evenly spaced between 8.2 GHz and 12.4GHz (X-band). The dielectric sheet was assumed to have a complex dielectric constant of $\varepsilon_r = 2 - j0.002$ and an electrical thickness of 4λ (82.4 mm), where λ is the wavelength of the mid-band frequency (10.3 GHz) in the dielectric material. In addition, 250 trials were performed to ensure convergence of the mean and standard deviation of the evaluated material properties.

In general, 101 discrete frequency points is beyond sufficient to find the envelope of the uncertainty associated with a given dielectric structure and noise power. Figure 3.3 shows the evaluated material properties. The error bars are placed at 3 standard deviations, which correspond to a 99% confidence interval.
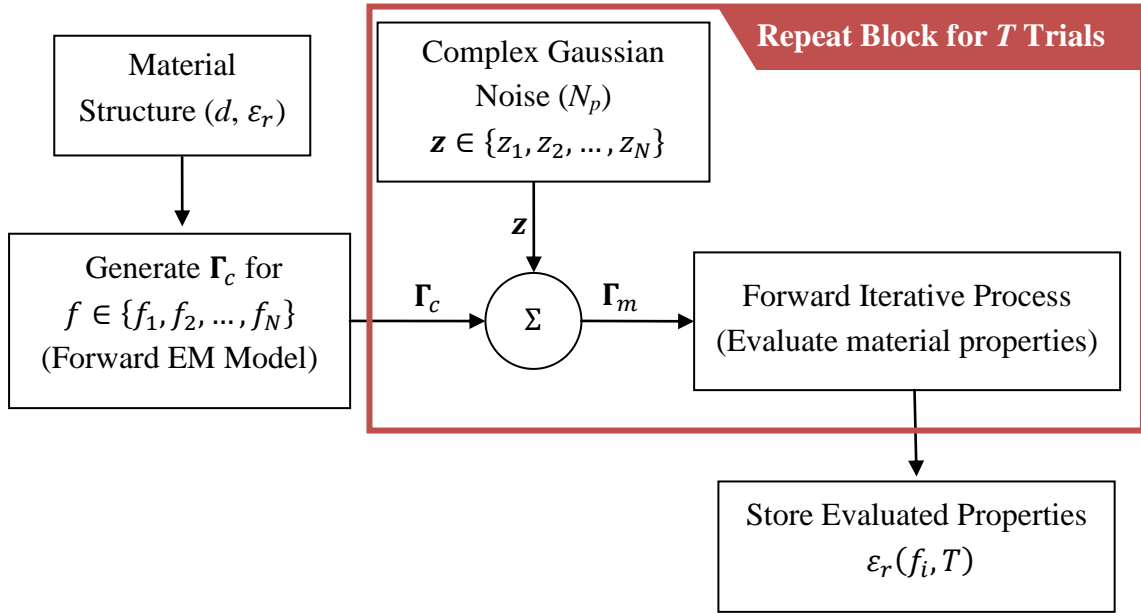
Figure 3.1. Block diagram of simulation to investigate the effect of system noise on the evaluation of material properties.
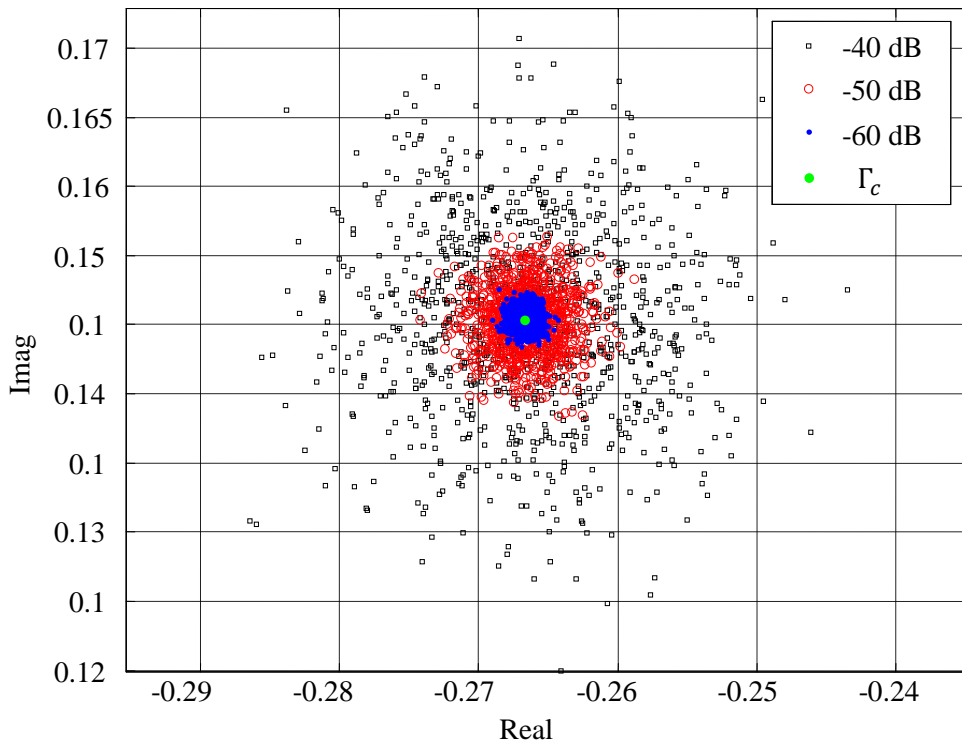
Figure 3.2. Calculated reflection coefficient (green dot) along with Γ_m for $T = 1000$ trials and three different noise power levels.

It can be seen that the uncertainties for both the permittivity (Figure 3.3a) and the loss factor (Figure 3.3b) are frequency dependent, as expected. The maximum uncertainty for this case occurs at $d/\lambda \approx 3.2$; however, the permittivity only deviates by approximately 1.75%. The loss factor, on the other hand, shows extreme deviations that are greater than 100%. However, this result was expected, as it is known that this technique does not provide accurate loss factor measurements [28]. The pattern in which minimum uncertainty occurs at $\lambda/2$ intervals is specific for this example and is generally not recurring. The reflection coefficient is a non-linear function of multiple properties (e.g. dielectric constant, thickness, and frequency) and consequently the uncertainty generally displays unpredictable behavior. In additional simulations for different material thicknesses, no general trend for the uncertainty envelops were recognized (results not shown here).

Next, a 0.238λ-thick (3.175 mm) conductor-backed sample with $\varepsilon_r = 4.8 - j0.17$ was simulated. The material characteristics of this sample correspond to those of a sample available in the laboratory for measurement. Once again, this sample was chosen to inspect a material setup that has proven difficult to measure in literature (thin and conductor-backed). In this simulation, 250 trials were performed for 3 different noise power levels at 21 discrete frequencies across the X-band frequency range. The uncertainty bounds can be seen in Figure 3.4 for (a) the permittivity and (b) the loss factor. As was seen in the previous case, the loss factor errors are much more significant than the errors in the permittivity. For this simulation setup, it can be seen that the uncertainty decreases as the frequency increases. Since the sample is much thinner than the previous scenario, the electrical thickness does not vary as significantly and thus there is not an undulating effect in the uncertainty bounds. Since the phase variation in the interrogating signal is significantly smaller (dielectric is much thinner) than the previous case, the errors are much higher. However, for a quality VNA, these simulations predict very accurate measurement results as the uncertainty bounds are quite small. In the next section, this measurement will be performed by a VNA with comparable noise power levels and the results will be compared. Additional uncertainty simulations for materials with varying thicknesses and dielectric constants (results not shown here) were performed. The uncertainty envelope for all these simulations was seen to be quite small

for noise power levels on the order of -50 dB. The uncertainty magnitudes shown in Figures 3.3 and 3.4 were typical for all the simulations that were performed.

(a)

(b)
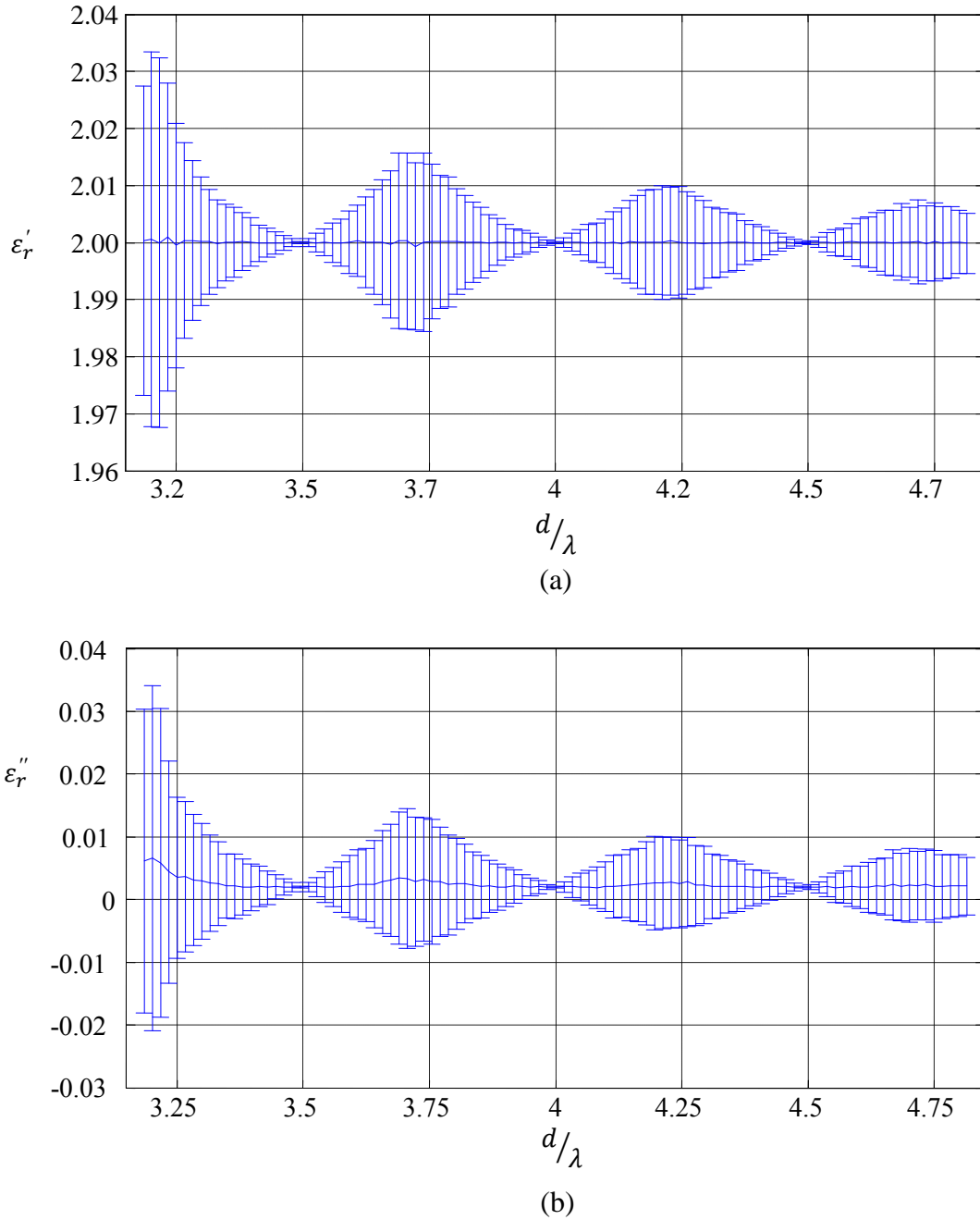
Figure 3.3. Uncertainty simulation for a WR-90 waveguide interrogating a 4λ-thick dielectric sheet with $\varepsilon_r = 2 - j0.002$, (a) permittivity and (b) loss factor.
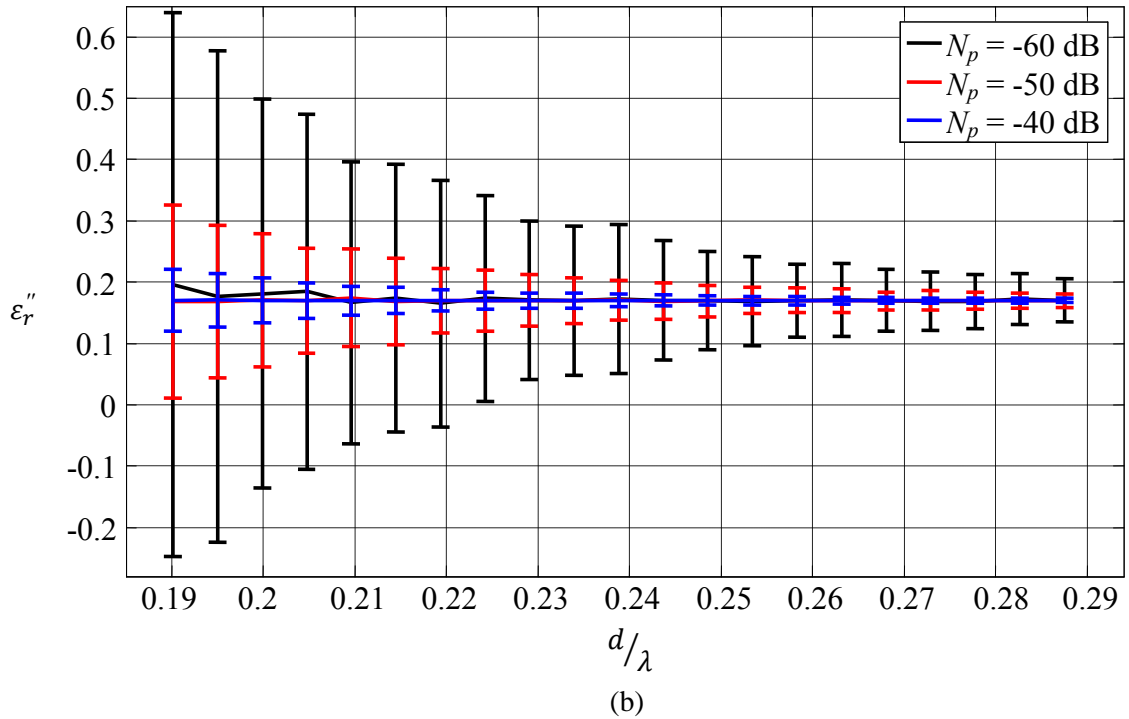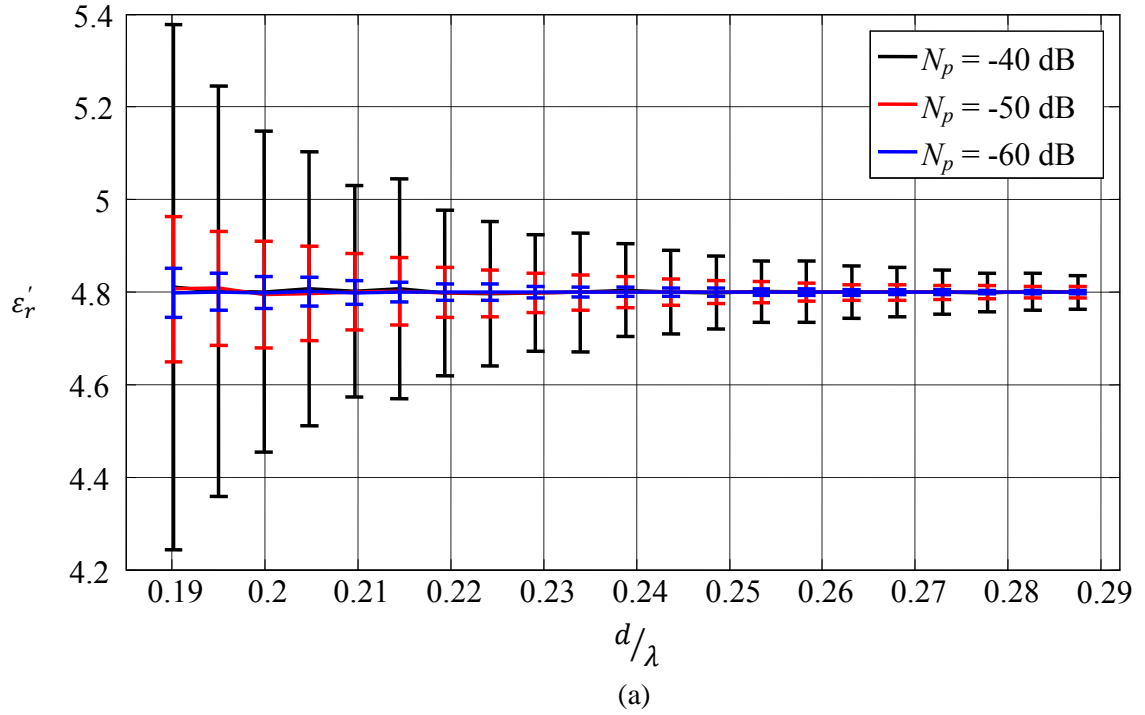
Figure 3.4. Uncertainty simulation for a WR-90 waveguide interrogating a 0.238λ-thick dielectric sheet with $\varepsilon_r = 4.8 - j0.17$ for: (a) permittivity and (b) loss factor.

3.3. MEASUREMENT VERIFICATION

In order to verify the simulated data, measurements were performed using an Agilent 8510C VNA and an in-house built X-band VNA that employs a non-coherent detection scheme. Due to the different detection architectures, the two systems have quite different noise characteristics. This measurement section will be split into two subsections. First, measurements made in which the noise floor of the 8510C VNA is manipulated by introducing a variable attenuation will be presented, and second, a comparison between the 8510 VNA and the in-house built VNA will be shown. The in-house built VNA will be referred to as the XVNA as it was built specifically for the X-band frequency range.

3.3.1. Agilent 8510C with Rotary-Vane Attenuator. In order to be able to manipulate the noise floor of the 8510C VNA, an X-band rotary-vane attenuator was cascaded between the VNA port and the open-ended waveguide. Consequently, by increasing the attenuation that is introduced into the reflection measurement path, the dynamic range of the system could be decreased, and its effect on recalculating material properties could be investigated. The open-ended waveguide was calibrated using the standard three waveguide loads (short, short-shim, matched load). The waveguide employed was a standard WR-90 waveguide and was terminated into a large custom flange with dimensions 152 mm x 152 mm. The large flange was used because it has been shown that a standard waveguide flange has the potential to introduce frequency dependent errors into the measured complex reflection coefficient [28].

To gain insight into the expected noise floor levels, 100 measurements with the waveguide terminated in the matched load were recorded with the attenuator set to introduce 0 dB, 10 dB, and 20 dB of total attenuation. It is important to remember that since this is a reflection measurement, the attenuation introduced is increased by a factor of 2 to account for the round trip propagation. Figure 3.5 shows the average magnitude of the 100 independent measurements, taken at 201 frequency points, for each of the three attenuation levels. It quickly becomes apparent that although the system was re-calibrated each time the attenuation was changed, the noise floor followed the same undulating trend and was shifted in the anticipated 10 dB steps. The apparent undulating trend in the noise floor, which is seen to be a function of frequency, is due to the finite directivity of

the VNA system as well as the imperfect matched load calibration standard. Consequently, the noise does not follow a Gaussian distribution that is completely independent of frequency. However, this does not render the simulations meaningless as they still provide a good estimate of the uncertainties that can be expected from a specified noise floor level.
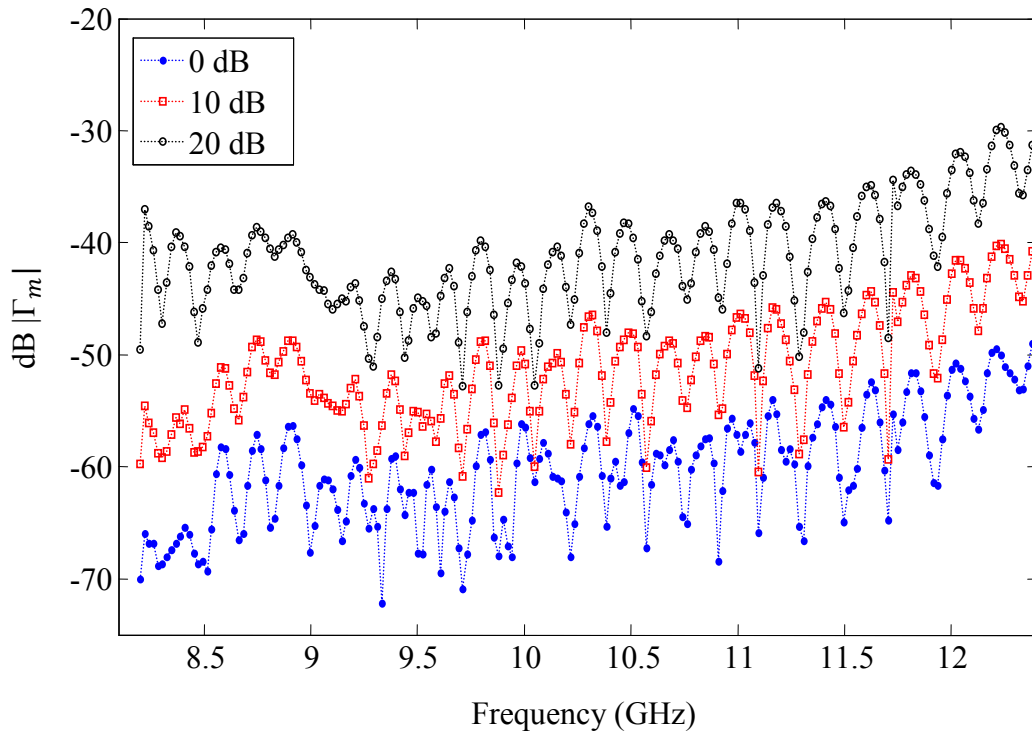
Figure 3.5. Noise floor of 8510C VNA with varying levels of attenuation introduced.

Next, a 3.175 mm-thick, conductor-backed rubber sheet was measured with the attenuator at the same three levels. Once again 100 measurements were taken so that a fair sample of the system noise would be obtained. Figure 3.6 shows the measurement noise for all three attenuator levels, plotted on the complex plane. The noise was calculated as:

$$z(f_i,n) = \Gamma_m(f_i,n) - \frac{1}{N}\sum_{n=1}^{100}\Gamma_m(f_i,n) \qquad (9)$$

where, N is the total number of independent measurements, and n is the measurement index, where $n \in \{1,2,...,N\}$. It can be seen in Figure 3.6 that that distribution of the noise has radial extensions where the noise is concentrated. These concentrated spurs are due to the frequency dependence of the noise.
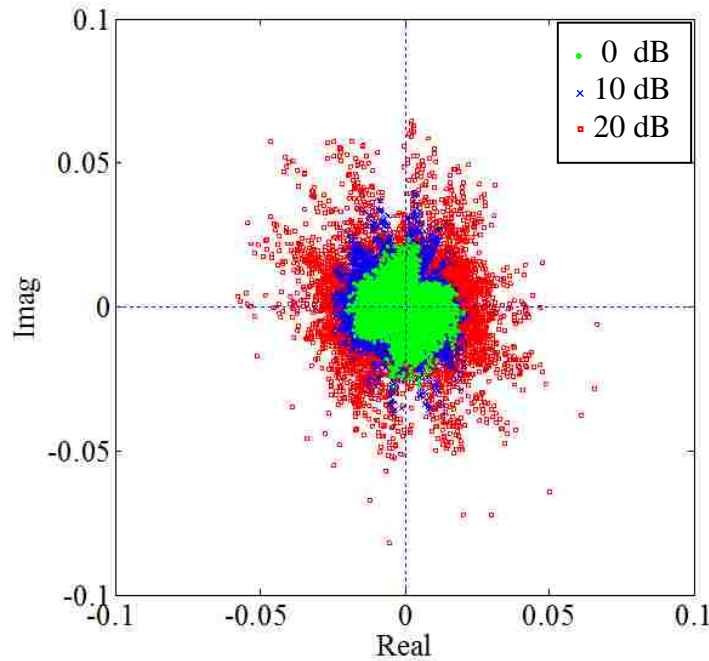
Figure 3.6. Noise in the measurement of a conductor-backed dielectric sheet.

The average reflection coefficient from the 100 measurements at each attenuation level along with the calculated reflection coefficient from the electromagnetic model can be seen in Figure 3.7. Upon first glance it becomes apparent that the system noise is not the dominating factor in the measurement error. Instead, there are strong, looping deviations between the calculated reflection coefficient and the measured reflection coefficient whose magnitudes are well above the noise power level for all three measurements. In addition, as the attenuation is increased, these deviations tend to decreases. This is because as the attenuation is increased, the power available at the aperture of the flange is decreased and therefore less power is radiated into the dielectric. It will be shown in the following chapters that these deviations are due to reflections

generated by the edges of the finite-sized flange. Since less power is radiated into the dielectric when the attenuation is high, the strength of the unaccounted for reflection from the edges of the flange are decreased and these deviations are not quite as severe.

Next, the material properties from what would be assumed to be the best case measurement (i.e. no additional attenuation was introduced and $N_p \approx$ -60 dB) was used to evaluate the complex dielectric constant of the rubber sheet. These results, along with the uncertainty bounds seen before are shown in Figure 3.8. It can be seen that the evaluated material properties from the measurements ($N_p \approx$ -60 dB) deviate well outside the 3 standard deviation bounds for the -40 dB noise level uncertainty bounds. Consequently, it is quite clear that the most significant errors in this measurement are not due to system noise, but rather are introduced by the finite-sized flange. In sections 4 and 5, the errors introduced by the finite-sized flange will be investigated and a correction method will be introduced.
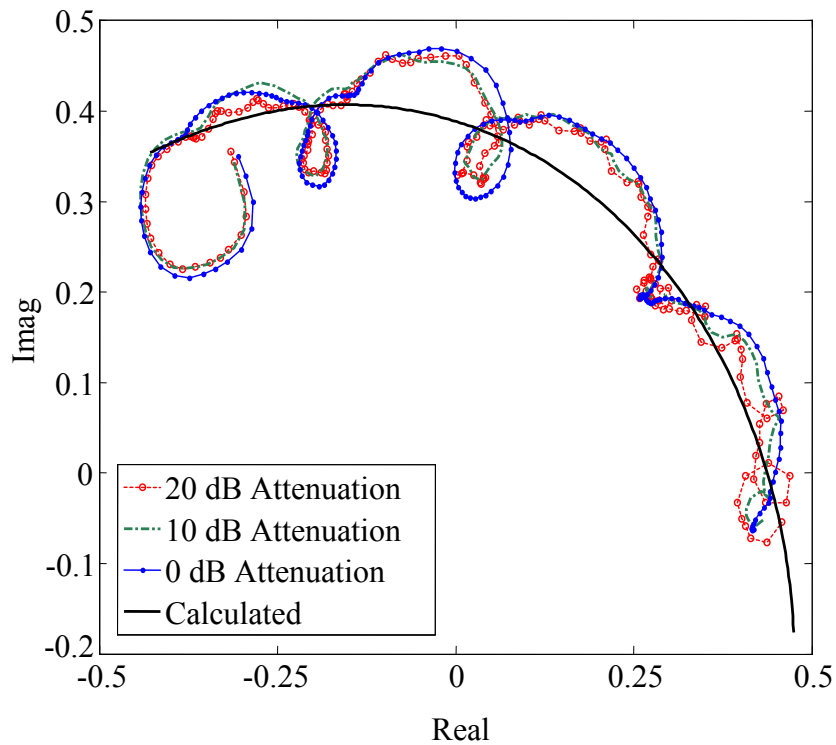
Figure 3.7. Measured reflection coefficient for 3.175 mm-thick conductor-backed dielectric with $\varepsilon_r = 4.8 - j0.17$.
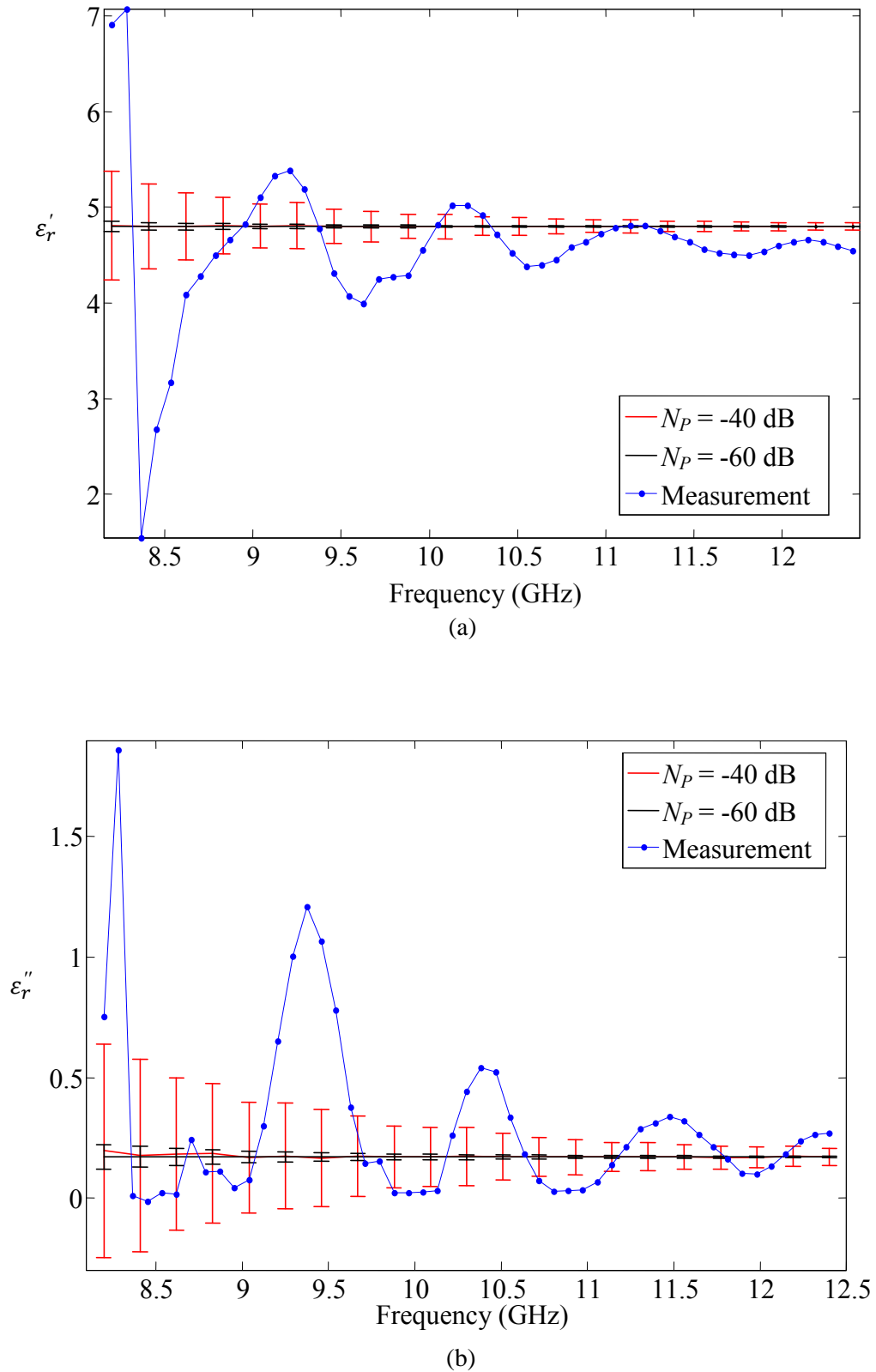
Figure 3.8. Evaluated material properties from measurement along with 99% confidence interval from uncertainty simulations for: (a) permittivity and (b) loss factor.

3.3.2. Comparison Between Agilent 8510C and Non-Coherent 1-Port VNA.
In the previous subsection, the noise characteristics of the 8510C VNA were manipulated using a variable attenuator. It was shown that the finite-sized flange introduced errors in the measured reflection coefficient that were significantly larger than the noise floor of the Agilent VNA. Consequently, for comparing the 8510C VNA with the XVNA, the measurements were *restricted* to lossy, air-backed materials that have been documented to be much less sensitive to the effect of the finite-sized flange [28], [30].

The measurements presented here were all made at X-Band using a WR-90 waveguide terminated into the same large custom flange. The measurement setup for a single dielectric sheet and a stacked two layer structure can be seen in Figure 3.9. The first measurement was of a 4.42 mm-thick air-backed rubber sheet with $\varepsilon_r = 7.28 - j0.275$. The actual value of the dielectric constant (and all dielectric constants reported as the actual value in this section) was acquired by using the completely-filled waveguide technique [8], [19] and was assumed to be a constant over the X-band frequency range [28]. The complex reflection coefficient was measured for 201 frequency points using the 8510C and the XVNA. The measured complex reflection coefficient, plotted on the complex plane can be seen in Figure 3.10.

(a)   (b)
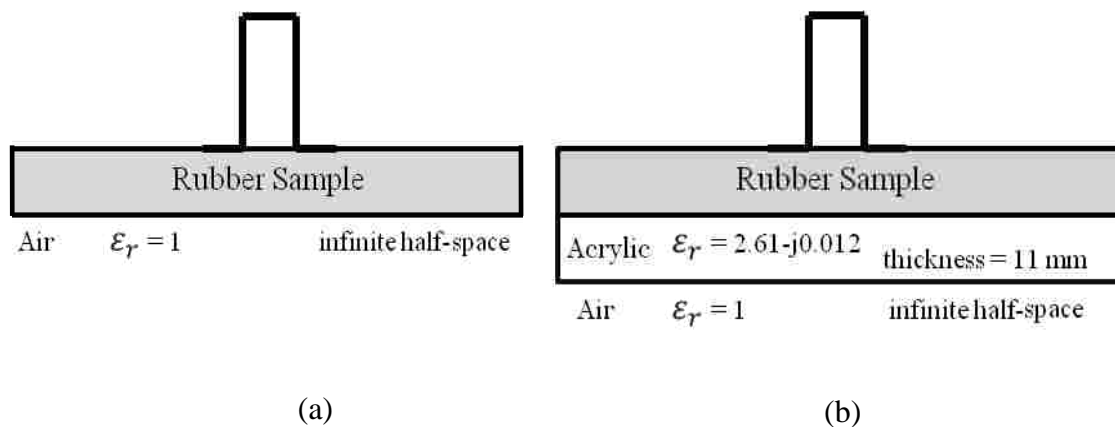
Figure 3.9. Measurement setup for material property evaluation for: (a) Tables 1,2 and (b) Tables 3,4.
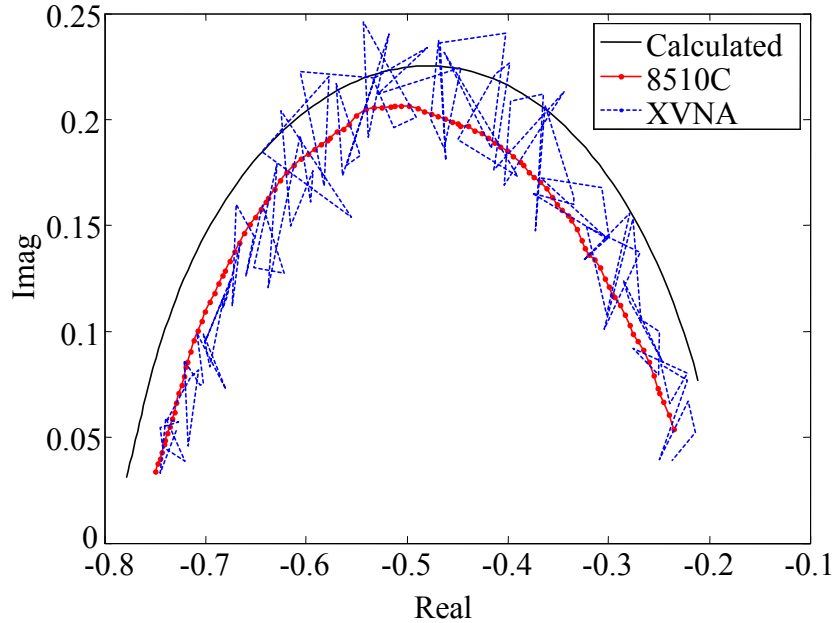
Figure 3.10. Simulated and measured complex reflection coefficient for a 4.42 mm-thick air-backed dielectric with $\varepsilon_r = 7.28 - j0.275$.

It can be seen that the 8510C VNA provides a very smooth reflection coefficient due to its excellent noise performance. The reflection coefficient is shifted from the calculated case which may be attributed to slight errors in the material characteristics or other measurement related problems. The XVNA on the other hand provided a relatively noisy reflection coefficient with a noise power of approximately -40 dB. It can be seen that the noisy reflection coefficient is generally centered about that measured by the 8510C. This relatively high noise level was expected since the XVNA employs a diode detector which allows broadband noise to be sampled along with the intended sinusoidal signal (as opposed to a coherent heterodyning system).

The evaluated material properties for both measured signals can be seen in Figure 3.11. The forward iterative optimization process was performed for 100 discrete frequency points and the material properties were assumed to be functions of frequency. As is expected, the 8510C material properties are accurate and have a low standard deviation. The properties evaluated from the reflection coefficient measured with the XVNA have a high standard deviation, but are centered about the value estimated from the 8510C. Once again the loss factor estimates are very poor and are generally

overestimated as reported in [28]. However, in general the XVNA provides results that give a good estimate of the permittivity even though it is a much noisier system. The mean value and standard deviation of the complex dielectric constant from each system can be found in Table 1.

This measurement process was repeated for an additional air-backed rubber sheet whose results can be seen in Table 2. Two additional measurements were made of a rubber sheet stacked on top of an acrylic sheet, as was shown previously in Figure 3.9b. Tables 3 and 4, provide the evaluated material properties for the rubber and acrylic sheets. In Tables 1-4 it can be seen that the mean values of the 8510C and XVNA are always quite similar. However, the standard deviation for the XVNA is always worse, with the exception of the loss factor values. The loss factor values present substantial errors and are in general void of useful information.
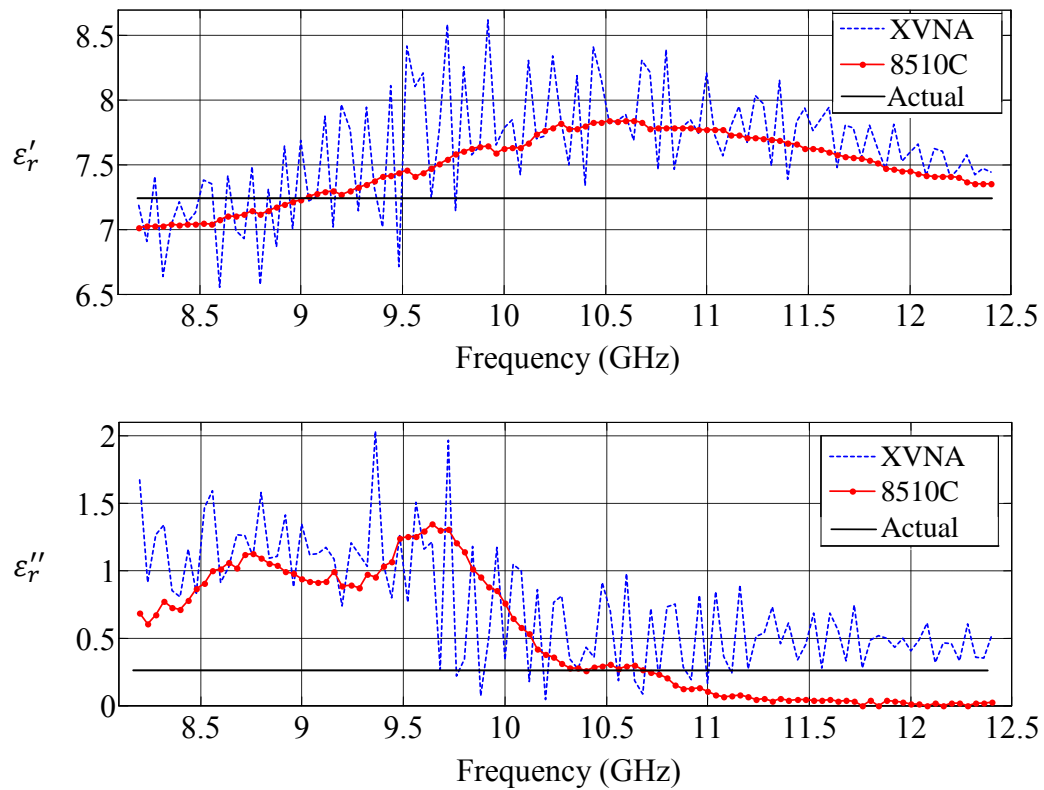
Figure 3.11. Evaluated material characteristics for rubber sheet backed by air.

Table 3.1 Evaluated material characteristics for rubber sheet backed by air with $\varepsilon_r = 7.28 - j0.275$.

VNA	Actual d (mm)	Actual ε_r	Estimated ε_r'		Estimated ε_r''	
			Avg.	Stan. Dev	Avg.	Stan. Dev
8510C	4.42	7.28 - j0.275	7.4887	0.2545	0.6989	0.1076
XVNA	4.42	7.28 - j0.275	7.6248	0.4355	0.748	0.4334

Table 3.2 Evaluated material characteristics for rubber sheet backed by air with $\varepsilon_r = 4.8 - j0.17$.

VNA	Actual d (mm)	Actual ε_r	Estimated ε_r'		Estimated ε_r''	
			Avg.	Stan. Dev	Avg.	Stan. Dev
8510C	3.175	4.80- j0.17	4.5662	0.1078	0.1101	0.0704
XVNA	3.175	4.80- j0.17	4.4366	0.3114	0.2343	0.2109

Table 3.3 Evaluated material characteristics for rubber sheet ($\varepsilon_r = 7.28 - j0.275$) stacked on an acrylic sheet and backed by air.

VNA	Actual d (mm)	Actual ε_r	Estimated ε_r'		Estimated ε_r''	
			Avg.	Stan. Dev	Avg.	Stan. Dev
8510C	3.175	4.80- j0.17	4.3727	0.138	0.0192	0.0263
8510C	11	2.61 - j0.012	2.2636	0.2708	0.1297	0.184
XVNA	3.175	4.80- j0.17	4.5663	0.3201	0.0637	0.1026
XVNA	11	2.61 - j0.012	2.3199	0.2943	0.0721	0.1171

Table 3.4 Evaluated material characteristics for rubber sheet ($\varepsilon_r = 4.8 - j0.17$) stacked on an acrylic sheet and backed by air.

VNA	Actual d (mm)	Actual ε_r	Estimated ε_r'		Estimated ε_r''	
			Avg.	Stan. Dev	Avg.	Stan. Dev
8510C	4.42	7.28 - j0.275	7.4201	0.3431	0.5054	0.4531
8510C	11	2.61 - j0.012	2.8203	0.2798	0.0705	0.1308
XVNA	4.42	7.28 - j0.275	7.4099	0.5344	0.4273	0.4354
XVNA	11	2.61 - j0.012	2.758	0.3062	0.086	0.1929

3.4. CONCLUSION

It was shown that when evaluating thin and low loss materials which have been reported to be difficult to measure, the deterministic errors introduced by the finite-sized flange dominate the errors. However, for lossy and thick air-backed materials, the advantage of expensive, high quality test equipment is relatively small. By comparing an Agilent 8510C VNA with an in-house VNA with a significantly higher noise level, it was shown that their average material estimations were in very good agreement. However, the 8510C has a much smaller standard deviation in the material property estimations. Due to the current restriction on the materials that may be evaluated (i.e. lossy and thick) the following sections of this thesis will investigate the errors introduced by the finite-sized flange as well as propose a modification to the standard waveguide flange that markedly reduces these errors.

4. ERRORS INTRODUCED BY THE FINITE-SIZED GROUND PLANE

4.1. INTRODUCTION

The accuracy by which material properties are evaluated is directly dependent upon the degree by which the measured complex reflection coefficient matches the results predicted by the electromagnetic (forward) model. In general, thin and low-loss conductor-backed structures have proven to be the most difficult to accurately characterize using an open-ended waveguide [28], [30], [37]. In Section 3, it was shown that these types of structures are more sensitive to measurement system noise than thick and higher loss structures. However, there are other more critical factors that contribute to recalculation inaccuracy when evaluating material properties.

The dominating error in estimating material properties has to do with the fact that the forward model assumes the rectangular waveguide aperture to be terminated into an infinitely-extended ground plane or flange [28], [30]. However, in practice the measurements are commonly conducted using a standard, finite-sized flange that is designed to primarily attach waveguide sections together. Consequently, the edges of the standard flange introduce an unwanted discontinuity thereby causing the radiated electromagnetic fields to partially reflect back, into the probing waveguide. Given that the full-wave, forward electromagnetic model assumes an infinite flange, this reflected field is not accounted for in the model [30].

In addition, a finite-sized sample may also create a similar reflected wave. It will be shown that the reflection caused by the finite-sized flange plays a more significant role in measuring the complex reflection coefficient and masks the reflections from a finite-sized sample. A schematic showing the reflections accounted for in the electromagnetic model along with those not accounted for can be seen in Figure 4.1.
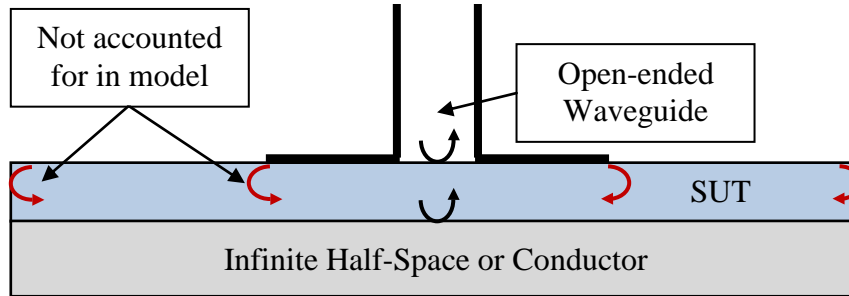
Figure 4.1. Reflections accounted for (black) and not accounted for (red) in the full-wave forward electromagnetic model.

4.2. FIELD STRUCTURES

The magnitude of the reflected waves which are generated at the edges of the finite-sized waveguide flange and the finite-sized sample depend on the magnitude and distribution of the incident electromagnetic fields. For example, large errors in the measured reflection coefficient can be expected in thin, low-loss and conductor-backed materials. This is because the boundary conditions of the two parallel conductors (the flange and the conductor backing) confine the electromagnetic energy to within the dielectric region between them. This resulting parallel plate wave guiding structure causes strong fields to be incident on the flange and sample edges. Although samples backed by an infinite half-space of air or another dielectric material do not have this parallel plate wave guiding structure, the dielectric material operates as a grounded dielectric sheet/slab [32], sustaining surface waves where the flange acts as the ground structure. The term grounded dielectric sheet/slab was coined in [32] and simply describes a dielectric material with a conductor on one side and air on the other. Like the parallel plate waveguide for conductor-backed structures, the grounded dielectric sheet can cause strong fields to be guided to the flange edges. When the electrical thickness (function of actual thickness and permittivity) of the dielectric becomes thick with respect to wavelength, the electromagnetic energy is allowed to disperse into a larger area and therefore the flange edges do not play as significant of a role.

To provide a graphical example of the wave guiding nature of these structures, a WR-90 waveguide with an 80 mm square flange was simulated using CST [38]. The

open-ended waveguide was evaluated radiating into both an air-backed and a conductor-backed dielectric sheet with a thickness of 5 mm and a complex dielectric constant of $\varepsilon_r = 5 - j0.05$. The material was specifically chosen to be low loss so that the electric field components would undergo little attenuation and therefore can be easily seen. In addition, the dielectric sample and the conductor backing were assumed to have infinite spatial extent in their lateral directions. This assumption was made because these simulations are intended to shown the field structures set up in the air-/conductor-backed dielectric structure and are not intended to evaluate the effects of a finite-sized sample.

Figure 4.2 shows a two dimensional plot of the vector electric field distribution in the dielectric sheet when backed by (a) a half-space of air and (b) a perfect electrical conducting (PEC) plane. The two dimensional plot was made by cutting through the center of the waveguide in the direction that is perpendicular to its broad dimension. Figure 4.2a illustrates that when the dielectric sheet is backed by an air half-space, the electric field propagates away from the aperture with a field structure that would be expected from a horn or open-ended waveguide operating as an antenna. More importantly, the dielectric material is shown to operate as a grounded dielectric sheet [38], guiding fields with substantial energy parallel to and along the surface of the flange, as highlighted in Figure 4.2a. At the edge of the flange a discontinuity is present in the fields guided by the dielectric sheet. The electric field is shown to fringe around the edge of the flange where a wave impedance mismatch is introduced as the ground structure is no longer present. In order to satisfy the wave impedance boundary condition, a reflected field is generated, which propagates back toward the probing waveguide aperture.

In Figure 4.2b, the electric field radiated from an open-ended rectangular waveguide into a conductor-backed dielectric sheet can be seen. In order to satisfy the PEC boundary conditions, the electric field inside the dielectric must rotate so that it is normal to the PEC planes. The electric field is then guided between the two conductors which operate as a parallel plate waveguide. This structure confines the energy radiated by the waveguide and guides it to the edges of the flange. Consequently, strong fields are incident at the discontinuity introduced by the flange edges. Once again this can be viewed as a wave impedance mismatch between the incident electric field which is guided between the parallel plates, and the wave impedance of the fields radiated out,

away from the flange. Consequently, this causes a reflected field that is guided back toward the probing waveguide aperture in the parallel plate structure. For very thin dielectric sheets, the fields in the parallel plate structure are tightly bound and therefore a significant portion of the energy incident on the flange edges is reflected.
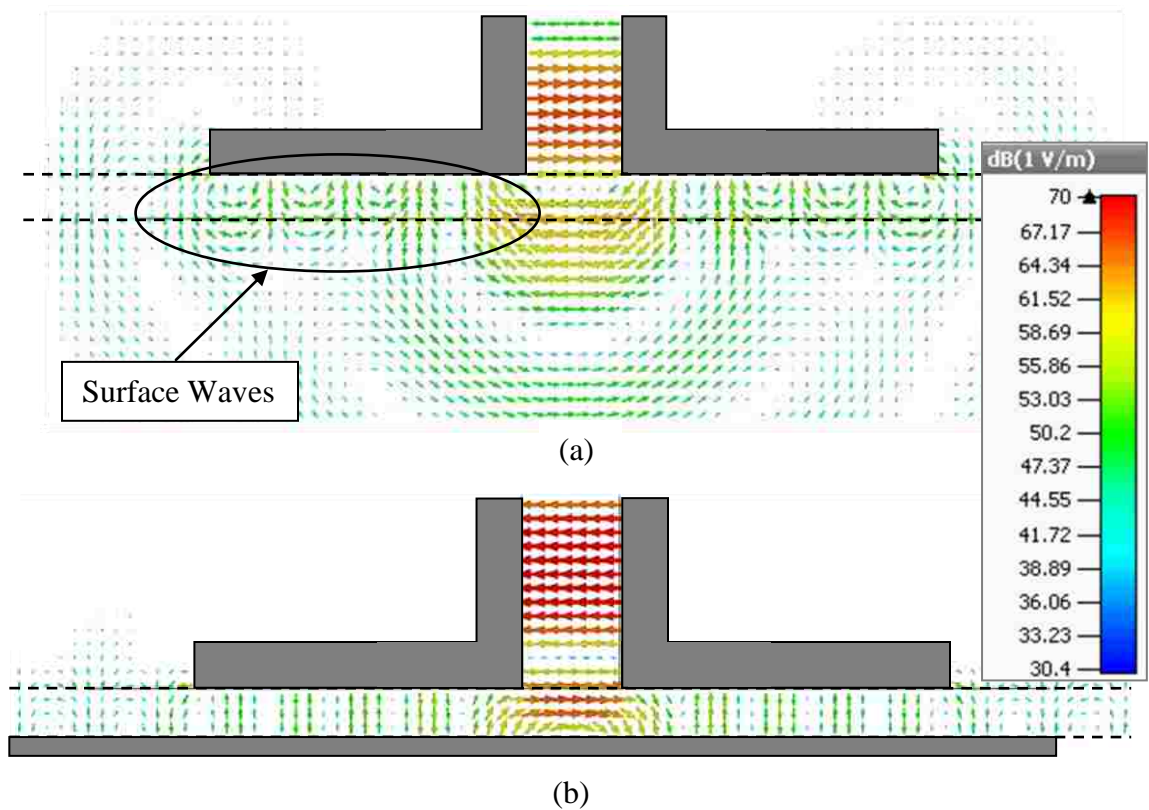
Figure 4.2. Electric field in a 5 mm thick dielectric with $\varepsilon_r = 5 - j0.05$ and backed by (a) an air infinite half-space and (b) a PEC conductor plane.

The geometry of a thin conductor-backed dielectric lends itself to an analogy very similar to the cavity model of a patch antenna as presented in [39]. Since the reflections from the edges of the flange are expected to be relatively strong, large standing waves or cavity modes will be formed between the flange and the conductor backing. Consequently, the dielectric region may be viewed as a cavity with perfect magnetic conductor (PMC) walls that are approximated by the strong impedance mismatch at the edges of the flange. Therefore, it is expected that measurements of thin conductor-backed

sheets will have significant reflections from the flange edges. This will translate to relatively large errors in the reflection coefficient at the waveguide aperture, when compared to that which is calculated by the forward model. Finally, these errors will cause inaccuracies in the estimated material properties.

4.3. FINITE-SIZED FLANGE VS. FINITE-SIZED SAMPLE

It was previously stated that a finite-sized sample causes reflected waves from its edges that are not accounted for by the forward electromagnetic model [30]. Consequently, to maximize the accuracy of this technique it is important to understand whether the reflection from the finite-sized flange or the finite-sized SUT has a greater influence on the measured complex reflection coefficient. With this understanding, the appropriate steps may be taken to correct for and/or minimize the most critical sources of errors.

To this end, CST Microwave Studio [38] was employed to simulate an open-ended rectangular waveguide with both a finite and infinite flange radiating into a dielectric sample with finite and infinite lateral (parallel to the waveguide flange) dimensions. The simulations were performed with WR-90 waveguides (22.86 mm x 10.16 mm) which operate in the X-band frequency range (8.2 − 12.4 GHz). The 5 mm-thick dielectric sample had a complex dielectric constant of ($\varepsilon_r = 5 - j0.05$). The simulations were conducted for both an air infinite half-space and a conductor-backing.

4.3.1. Dielectric with Infinite Half-Space Backing. First, the dielectric sheet backed by an infinite half-space of air will be discussed. The following simulations were performed at 10.3 GHz, corresponding to the center of the operating frequency for WR-90 waveguides. For all four cases, the electric field distributions shown were evaluated at a depth of 0.25 mm into the material (referenced from the plane of the waveguide flange).

4.3.1.1 Infinite Flange/Infinite Sample. Figure 4.3a shows the magnitude of the electric field distribution inside the dielectric sample. The sample was assumed to have infinite spatial extent in the lateral dimensions and was illuminated by a waveguide probe with an infinite flange. It can be seen that the electric field smoothly transitions away from the aperture. In addition, the electric field distribution is symmetrical across the broad dimension of the waveguide. The strong electric field concentration in the vertical

direction corresponds to the dominant waveguide TE_{10} mode electric field polarization. The electric field distribution has been truncated for graphical purposes; however, due to the infinite flange/sample size, the fields can be assumed to continue to smoothly diverge from the aperture.

4.3.1.2 Finite Flange/Infinite Sample. Figure 4.3b shows the electric field distribution for a sample with infinite lateral dimensions and an interrogating waveguide with a finite-sized flange. The flange was 40 mm x 40 mm, designed to approximate the standard UG 135/U waveguide flange. A square with a dashed line has been inserted into the plot to indicate the footprint of the waveguide flange. It can be seen that there is a strong discontinuity in the electric field at all four edges of the waveguide flange. This is due to a wave impedance mismatch between the fields directly in front of the flange and those in the surrounding space which generates a reflected wave in order to match the impedance boundary conditions. The fields that are reflected back to the aperture are sampled along with the expected reflection from the material, and thus introduce an error in the measured reflection coefficient. The strongest electric field discontinuities, which are along the horizontal edges of the waveguide flange, are due to the fact that the electric field polarization causes stronger fields to be radiated in these directions (as seen in Figure 4.3a for an infinite flange).

4.3.1.3 Infinite Flange/Finite Sample. Figure 4.3c shows the electric field distribution for a finite-sized sample with lateral dimensions of 60 mm x 60 mm and an infinite waveguide flange. This simulation represents the scenario where the flange size extends beyond the sample size. This scenario depicts the effect that a finite-sized sample has on the electric field distribution, assuming there is no discontinuity introduced by the waveguide flange. As is expected, the dielectric-air interface creates a wave impedance mismatch, generating a reflected wave. This is because the dielectric sample is operating as a grounded sheet, guiding surface waves to the edges of the sample where the sheet is abruptly truncated. The reflected fields from the material interface create a standing wave pattern that can be seen in the dielectric material.

4.3.1.4 Finite Flange/Finite Sample. Finally, Figure 4.3d shows the electric field distribution in the dielectric sheet with finite lateral dimensions (60 mm x 60 mm) and a finite waveguide flange (40 mm x 40 mm). This represents a worst case measurement

scenario where the sample extends only 10 mm past the edges of the flange in all directions. In this case, the finite-sized flange creates a strong wave impedance mismatch which, again, generates a reflected wave. Due to this field perturbation, the fields incident at the edges of the finite-sized SUT have much lower amplitudes than for the infinite flange case (Figure 4.3c). Consequently, the reflected fields from the dielectric-air interface have a lesser impact on the overall reflection coefficient. Although there is a discontinuity at the edges of both the flange and the SUT, it can be seen that the discontinuity introduced by the flange edges effectively masks that of the finite-sized SUT.

4.3.2. Dielectric with Conductor Backing. To fully evaluate the effects of a finite-sized flange and sample it is important to inspect their impact on a conductor-backed dielectric as well. This is because it was previously shown the field structures of an air- and conductor-backed dielectric are quite different and therefore it cannot be assumed that the flange and sample will have the same effect on the electric field distributions. Consequently, four more CST simulations were performed to inspect the four previous flange/sample configurations for a conductor-backed sample. The open-ended waveguide was a standard WR-90, terminated into both an infinite flange and a standard (40 mm x 40 mm) flange. The dielectric sheet was identical to that used in the air-backed simulations with the only adjustment being the introduction of a PEC plane behind it (as opposed to an infinite half-space). The conductor backing was assumed to have infinite spatial extent for all four cases. The electric fields that will be shown for the conductor-backed cases were sampled at a depth of 0.25 mm into the dielectric material (referenced to the plane of the flange). As was the case in the previous simulations, the frequency was 10.3 GHz.

4.3.2.1 Infinite Flange/Infinite Sample. The electric field for the infinite flange and infinite conductor-backed sample can be seen in Figure 4.4a. The electric field is seen to smoothly transition away from the waveguide aperture. As was shown in Figure 4.2, the parallel plate structure guides the fields away from the aperture. Since the both the flange and the sample are assumed to have infinite lateral dimensions, the fields indefinitely propagate radially away from the aperture.

(a)

(b)

Flange Footprint

Finite Sample

Finite Sample

(c)

(d)

Flange Footprint
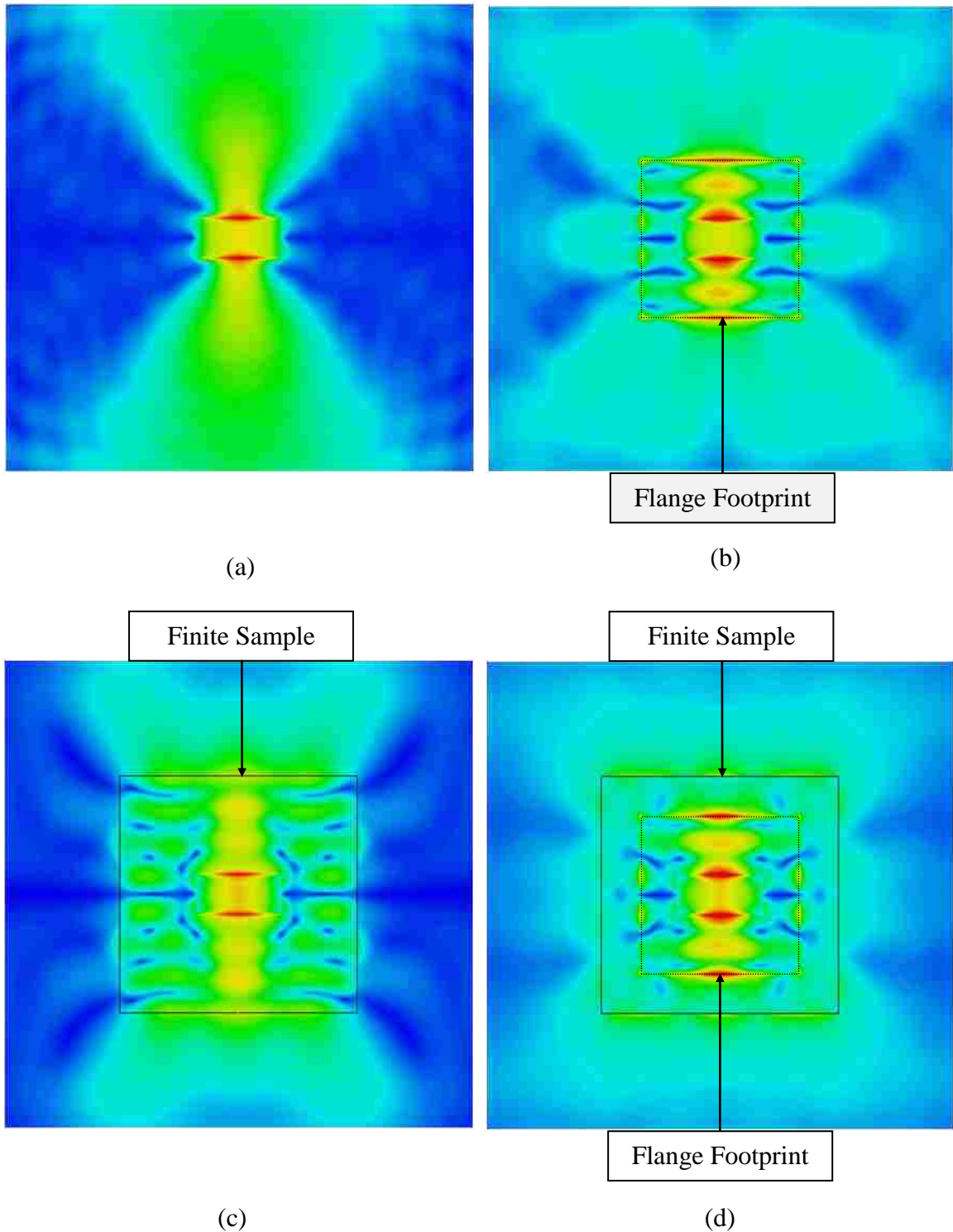
Figure 4.3. Magnitude of the electric field distribution in a 5 mm-thick dielectric with $\varepsilon_r = 5 - j0.05$ and backed by an infinite air half-space for: (a) infinite flange/infinite sample, (b) finite flange/infinite sample, (c) infinite flange/finite sample, and (d) finite flange/finite sample.

4.3.2.2 Finite Flange/Infinite Sample. Figure 4.4b shows the electric field for a finite flange and infinite sample. It can be seen that there is a discontinuity in the electric field along all four edges of the finite-sized flange. The maximum discontinuity is across the horizontal edges of the flange, which is due to the electric field polarization. The fields that radiate out away from the flange are of no concern as there is no mechanism to cause them to be re-directed back toward the aperture (the sample and conductor backing are infinite and will not introduce a reflected wave).

4.3.2.3 Infinite Flange/Finite Sample. Figure 4.4c shows the electric field for an infinite flange and finite-size sample. The practical analogy of this setup is for a sample whose dimensions are smaller than the waveguide flange. Although it would not be recommended to use the open-ended waveguide technique in this scenario it has been included here for completeness. The dielectric-air interface generates a strong reflected field that creates a standing wave pattern inside the dielectric sample. This reflection is due to a wave impedance mismatch. This is because the parallel plate wave guiding structure abruptly changes from being completely filled by a dielectric to being filled only by free-space.

4.3.2.4 Finite Flange/Finite Sample. Finally, Figure 4.4d presents the case where both the flange and the sample have finite lateral dimensions. The electric field can be seen to be perturbed at both the edges of the sample as well as the dielectric-air interface. However, the discontinuity at the edges of the finite-sized sample is shown to have a smaller effect on the electric field. This is because the discontinuity at the edges of the finite-sized flange creates a reflected wave and strongly perturbs the electric field. Consequently, the fields that are radiated to the edges of the finite-sized SUT are at a much lower amplitude.
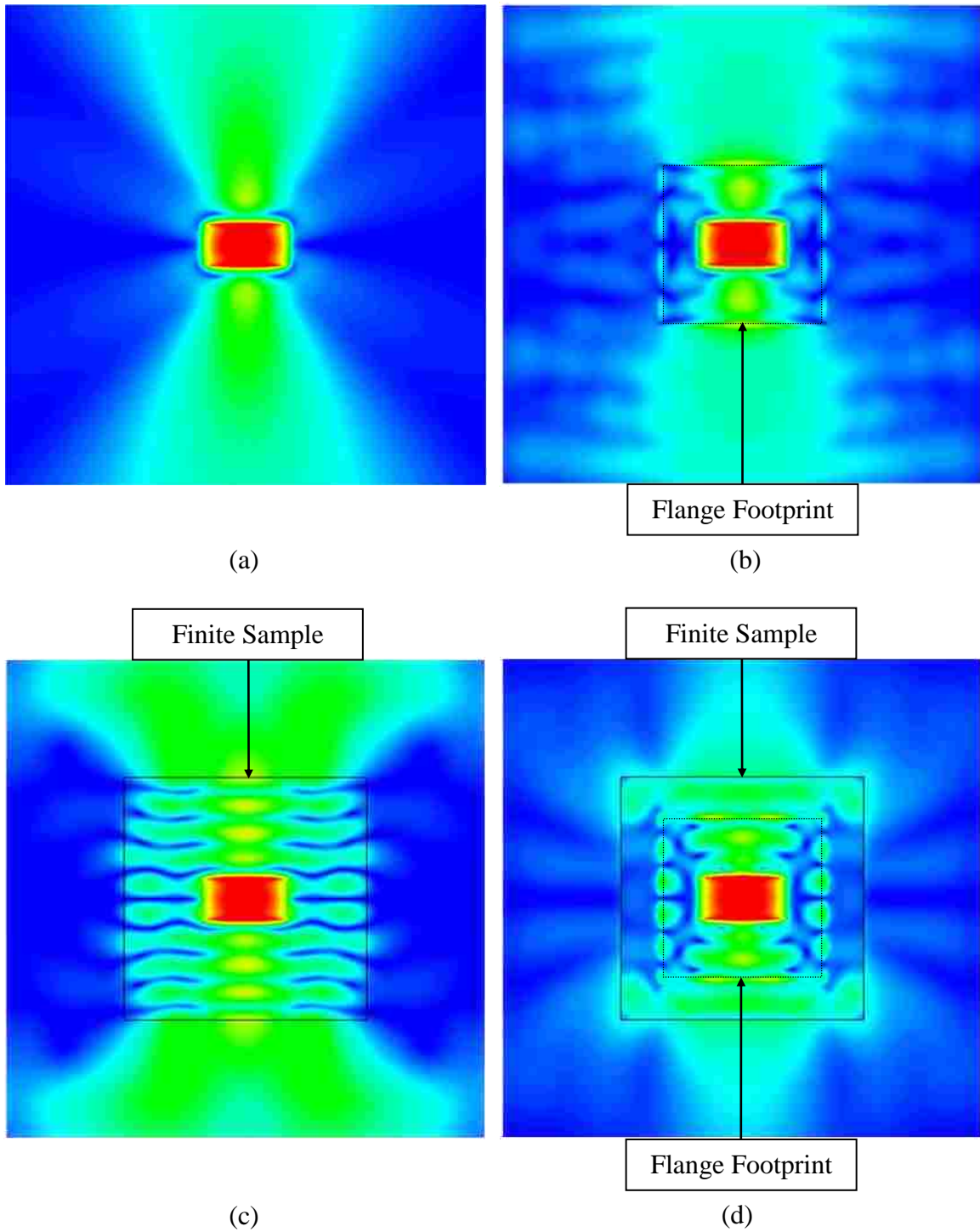
Figure 4.4. Magnitude of the electric field distribution in a 5 mm-thick conductor-backed dielectric with $\varepsilon_r = 5 - j0.05$ for: (a) infinite flange/infinite sample, (b) finite flange/infinite sample, (c) infinite flange/finite sample, and (d) finite flange/finite sample.

4.3.3. Effect of Finite-Sized Flange/SUT on Reflection Coefficient. In order to make a more quantitative evaluation of the effects of a finite-sized flange and finite-size sample on the complex reflection coefficient, additional CST simulations were performed for an open-ended rectangular waveguide radiating into a thin dielectric sheet that is backed by an infinite air half-space. The dielectric sheet was assumed to have a thickness of 0.48 mm, permittivity of ε_r = 3.3, and loss-tangents of $tan\delta$ = 0.01 and 0.1. These values were chosen to represent a fiberglass sheet like those, for example, used in an aircraft radome structure. These simulations were performed with a WR-90 waveguide terminated into both an infinite flange and a standard (40 mm x 40 mm) flange. In addition, the sample size was varied to have small (75 mm x 75 mm), large (150 mm x 150 mm), and infinite lateral dimensions.

Figure 4.5 shows the reflection coefficients simulated for both the infinite and finite-sized flanges radiating into the three dielectric sample sizes. The reflection coefficients are referenced to the aperture of the open-ended rectangular waveguide and have been plotted on the complex plane. In Figure 4.5a, the results can be seen for the low loss case in which the material had a loss tangent of ($tan\delta$ = 0.01). The two finite flange cases, for both a large and a small sample size, produce reflection coefficients that significantly deviate from the infinite flange/infinite sample case. The infinite flange/finite-sized sample cases can also be seen to deviate from the infinite flange, infinite sample case, but not nearly as strongly as the results for the finite-sized flanges. In addition, it can be seen that for a finite-sized flange, the size of the sample plays a small role in the complex reflection coefficient. As was shown in Figure 4.3d, the discontinuity due to the finite-sized flange perturbs the electric field and masks the effects of the finite-sized sample.

In Figure 4.5b, similar results for the more lossy case ($tan\delta$ = 0.1) can be seen. Once again, the reflection coefficients for a finite-sized flange are shown to deviate significantly from the actual reflection coefficient (infinite flange/infinite sample case). Due to the increased loss in the material, the finite-sized samples cause less of an adverse effect in the reflection coefficients (compared to Figure 4.5a). This is because the loss in the material helps to attenuate any signal that reaches and is reflected from the dielectric-air interface.
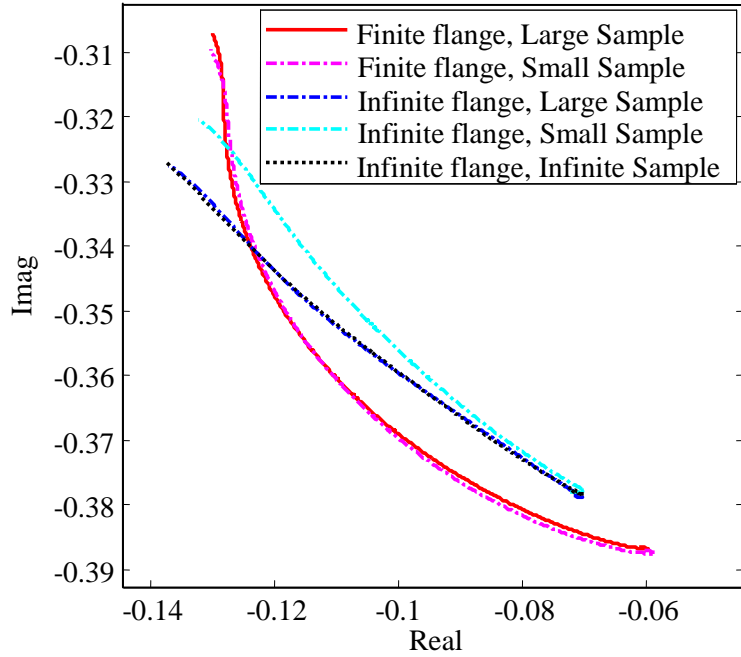
(a)
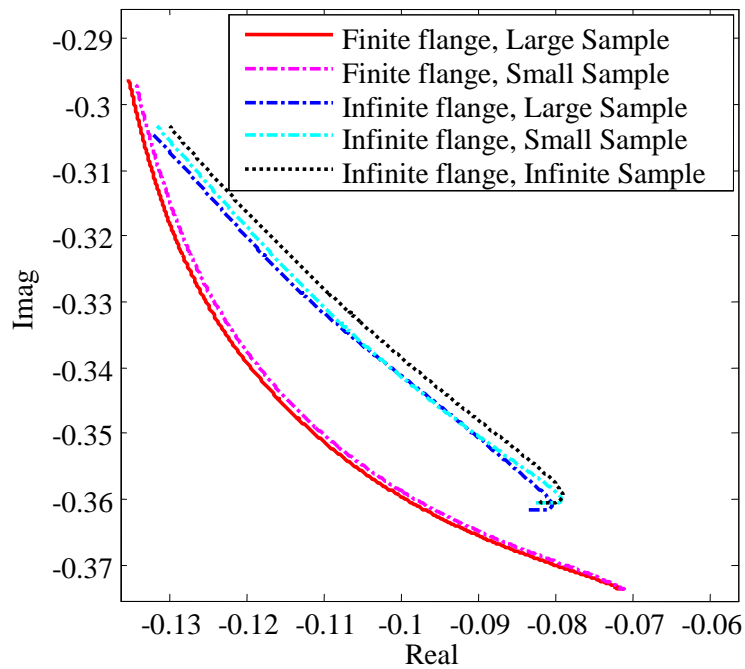
(b)

Figure 4.5. Reflection coefficient, plotted on the complex plane for a waveguide with a finite and infinite flange radiating into a dielectric sheet for loss tangent: (a) $\tan \delta = 0.01$ and (b) $\tan \delta = 0.1$.

It has been shown that a finite-sized sample, as well as a finite-sized flange, introduce errors in a reflection coefficient measurement that are unaccounted for in the full-wave forward electromagnetic model. These reflections will be shown to have a negative effect on the estimated material properties due to the deviations they cause from the theoretical calculated reflection coefficient. The finite-sized flange has been shown to introduce the largest error in simulated reflection coefficients. Therefore, the effects of the waveguide flange will be the focus of the work in this thesis. Consequently, from this point on, the SUT will be assumed to have infinite spatial extent in its lateral dimensions, or be large enough that it does not affect the reflection coefficient.

4.4. INFLUENCE OF FINITE FLANGE DIMENSIONS

Since it has been shown that the finite-sized flange has the most significant contribution to the error introduced by reflections that are unaccounted for in the forward electromagnetic model, it is important to understand how the SUT material properties affect these reflected fields. Consequently, CST simulations were performed for a wide range of materials with varying permittivity and loss factor values as well as for multiple thicknesses. In addition, the effect of both an infinite air half-space and a conductor-backing for the dielectric material were evaluated. The dielectric samples were all assumed to have infinite spatial extents in their lateral dimensions. This subsection is divided into three major parts, the first part investigates air-backed dielectric structures, the second part investigates conductor-backed dielectric structures, and the third part presents measured data to verify the conclusions drawn from the simulations.

To perform these simulations, MATLAB® was used to control CST so that the simulation process could be automated. This was done by using the built in ActiveX commands in MATLAB®. These commands are able to build a component object model (COM) server which is capable of communicating between the two programs. This was coupled with a library built into CST which contains the required object commands to configure and control simulations. Using MATLAB®, the parameters that were desired to be varied were loaded one-by-one to CST, and then a simulation was performed. Upon finishing the simulation, a Touchstone (.s1p) file was exported containing the reflection

coefficient data and the process was repeated. A copy of the MATLAB code required to perform this routine is provided in Appendix A.

The following simulations were performed using the CST Frequency Domain (FD) solver. It was seen that the FD solver offered more accurate results than that of the Time-Domain (TD) solver. This decision was made by simulating and comparing results for the same material structures between the FD and TD solver along with the electromagnetic model employed here. The FD solver and the electromagnetic model provided results that were consistently in good agreement.

4.4.1. Air-Backed Structure Simulations. The first type of structure investigated was single layered dielectric sheets/slabs backed an infinite air half-space. To investigate the effect of a finite-sized flange, WR-90 waveguides, terminated by flanges with square dimensions of 40 mm, 80 mm, and 120 mm were considered. These flange configurations were simulated radiating into an air-backed dielectric sheet with thicknesses varying from 5 mm to 20 mm in 5 mm increments. The relative permittivity was varied to be 2, 5, and 10 while the loss tangent was evaluated at 0.01, 0.1 and 1 resulting in a total of 36 configurations. However, only three cases are presented here as the results from all 36 configurations are very similar.

The reflection coefficient for each of these configurations was calculated, referenced to the aperture of the open-ended waveguide via CST simulations. Then, using the electromagnetic forward model and the forward-iterative optimization procedure outlined in Section 2, the complex dielectric constant was recalculated. In doing so, it was assumed that the exact thickness of the dielectric sheet is known. The recalculated complex dielectric constant was assumed to be a function of frequency and was evaluated at 51 evenly spaced frequencies across the operating band (8.2 -12.4 GHz). In addition, the actual values of dielectric constants were used as the initial guess values,, which helps to ensure convergence to a close solution. Using the actual material values as the initial guess is acceptable because these simulations were not meant to test the capability of the optimization process, but rather to investigate how the finite-sized flange affects the reflection coefficient and estimated material properties. In addition, in practice these values are commonly known *a priori* and their use in this way helps to not only speed up the recalculation process but also the accuracy of recalculation.

The simulated reflection coefficient along with the estimated complex dielectric constant for a permittivity of $\varepsilon_r' = 2$, a thickness of 5 mm and a loss factor of $\varepsilon_r'' = 0.02$, 0.2, and 2 can be seen in Figure 4.6(a-c), respectively. The calculated reflection coefficient for an infinite flange has been included for comparison purposes. In Figure 4.6a ($\varepsilon_r'' = 0.02$), it can be seen that the finite-sized flanges cause the reflection coefficients to deviate from that of an infinite flange. The 40 mm-flange results deviate the most form those with infinite flange. This was expected since this flange has the smallest dimensions and therefore the reflected waves from the flange edges undergo the least attenuation in the material.

As the flange size increases, the phase variation of the reflected signal, due to the increased distance between the flange edges and the waveguide aperture, is apparent as the resonant arcs or loops that encircle the reflection coefficient for an infinite flange on the complex plane. The repetition rate of these arcs is due to the material properties along with the flange size. This effect can be explained with simple vector addition as is illustrated in Figure 4.7. The reflection coefficient measured or simulated at the aperture of the waveguide, Γ_m, is the coherent addition of the reflection coefficient measured by an infinite flange, Γ_c, and the unaccounted for reflections generated at the edges of the finite-sized flange, Γ_e. All three of these quantities are functions of frequency and material properties (complex dielectric constant, thickness, and backing) while the edge reflections are also a function of the flange geometry. In general, it is correct to assume that the reflection from the edges of the flange has a smaller amplitude than the actual/calculated reflection coefficient from the material structure (Γ_c). In addition, as frequency changes, the electrical length between the aperture and the flange edges also changes, causing a phase difference in the fields reflected from the flange edges. Due to the lower amplitude and the phase variation as frequency changes, the reflections from the edges of the flange are expressed as the circular arcs that loop around the reflection coefficient of an infinite flange.

From the recalculated permittivity and loss factor values, shown in right hand column of Figure 4.6, it can be seen that as the flange size increases, the estimated material properties typically become more accurate. The actual values of the material properties have been included in the figures as solid black lines for reference. The

undulating pattern the estimated material properties is related to the phase variation of the fields that are reflected from flange edges. Consequently, as the flange size becomes larger, the reflected signals play a smaller role in the evaluated material properties. However, this process is *not monotonic* with respect to flange size. Although the reflected fields from the edges experience more attenuation as the flange size increases, this does not mean that their interference effects at the waveguide aperture reduces the effect on the reflection coefficient. This can be seen in Figure 4.6a,b as the 80 mm flange provides a better permittivity and loss factor estimate than the 120 mm flange.

In addition, as the loss in the material increases the errors in the reflection coefficient and the recalculated permittivity and loss factor values are seen to decrease. For a specific flange and material geometry, increasing the material loss does provide a monotonically decreasing error in the evaluated material characteristics. This is because the general interference pattern is not changed, but the amplitudes of the reflected waves have decreased. For the case where the loss factor, $\varepsilon_r'' = 2$ (Figure 4.6c), there is a clear offset that can be seen in the recalculated material characteristics. This shift is due to compounding the numerical inaccuracy of the CST model as well as the inaccuracies associated with the numerical integration performed in the electromagnetic forward model and the number of higher-order modes that were evaluated at the waveguide aperture (6 modes in this case).
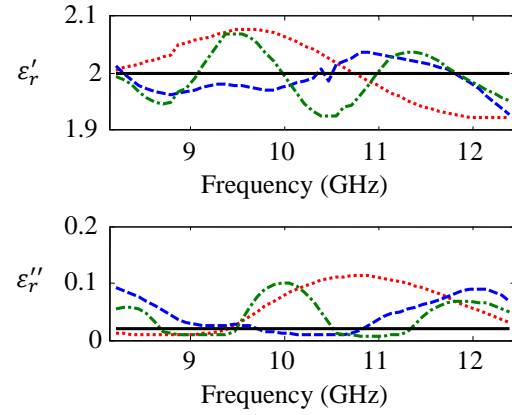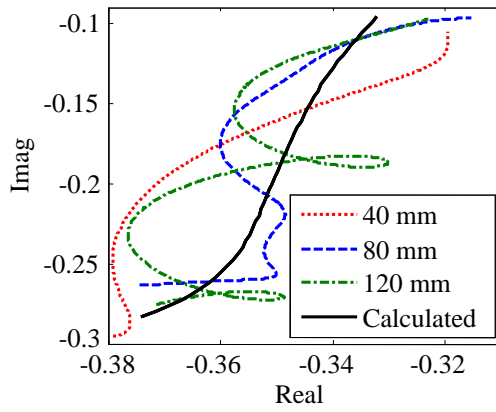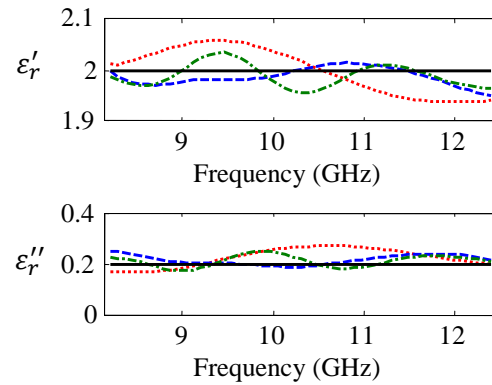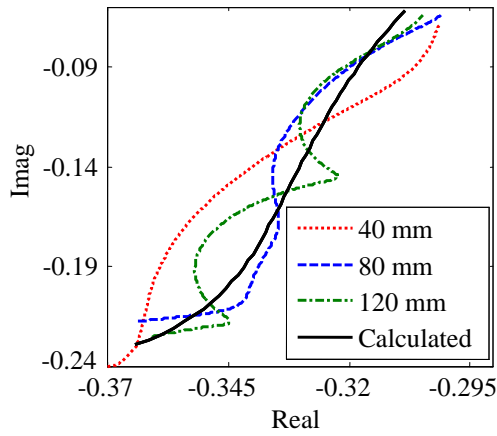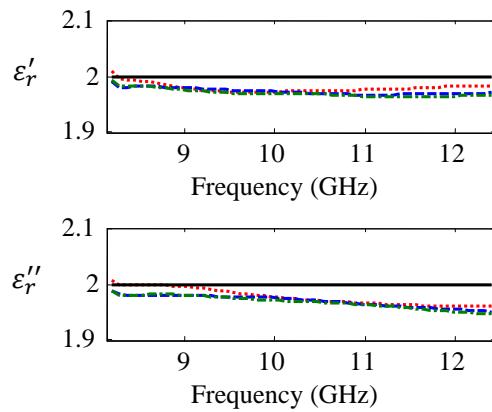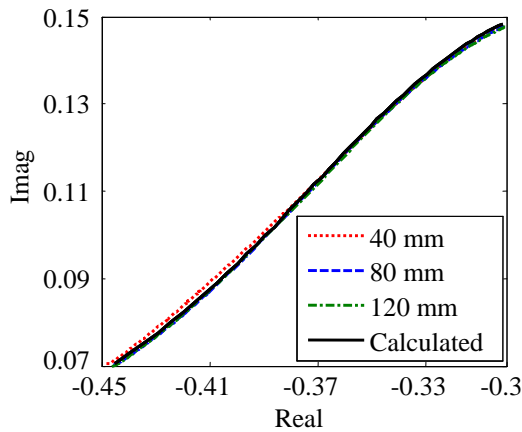
Figure 4.6. Complex reflection coefficient and evaluated material properties for a 5 mm-thick air-backed dielectric sheet with permittivity $\varepsilon_r^{'} = 2$ and loss factors of: (a) $\varepsilon_r^{"} = 0.02$ (b) $\varepsilon_r^{"} = 0.2$ and (c) $\varepsilon_r^{"} = 2$.
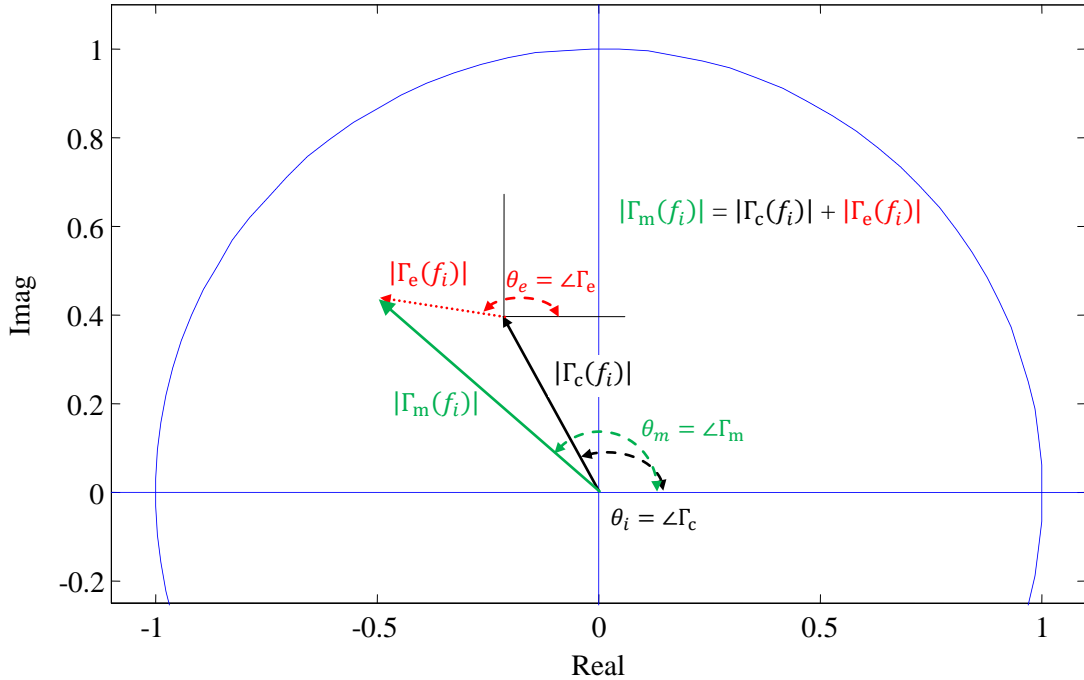
Figure 4.7. Example showing vector addition of reflection coefficient from an infinite flange and the reflected fields from the flange edges.

4.4.2. Conductor-Backed Structure Simulations. Next, single layer dielectric sheets were evaluated when backed by a PEC. The simulations were performed in the same fashion as those in the previous section that were backed by an infinite air half-space. Once again, the interrogating probe was a WR-90 waveguide terminated into a 40 mm, 80 mm, and 120 mm square flange. The material properties were varied with the same values as in the previous section. Once again, the sample, as well as the conductor backing, was assumed to have infinite lateral dimensions.

Figure 4.8 presents the simulated reflection coefficient, referenced to the aperture of the open-ended waveguide for a dielectric with a permittivity of 2, thickness of 5 mm, and loss factors of 0.02, 0.2, and 2 (corresponding to a-c, respectively). The calculated reflection coefficient for an infinite flange has also been included. It can be seen in Figure 4.8, that adding a conductor backing has introduced errors in both the reflection coefficient and the estimated material properties that are larger than when backed by air. The reflection coefficient for the 40 mm x 40 mm flange shows little resemblance to that of an infinite flange. As was the case for the air-backed sheet, the smallest flange

produces the largest amplitude errors in both the reflection coefficient and the evaluated material properties, except for case (c) where the relatively high material loss makes the flange size effect negligible. Once again, increasing the flange size is shown to produce better estimates of the material properties but as was previously mentioned, this is not monotonic. The phase variation introduced by the longer distance the reflected signals must travel for the 80mm and 120 mm flanges is again apparent as the resonant arcs that appear in the reflection coefficient.

As the loss in the material is increased, the standing waves formed in the wave guiding structure become damped and thus have a reduced effect on the reflection coefficient. Consequently, the estimation accuracy of the permittivity and loss factor increase while their standard deviations as functions of frequency decrease. Once again for the highest loss case (Figure 4.8c), there is a constant shift in the estimated loss factor. As was the case for the air-backed structure, this can be attributed to numerical inaccuracies in the CST simulation as well as the electromagnetic model. As was the case for the air-backed configurations, the results from the additional 33 simulated configurations are not included here as they provide very similar results to those shown in Figure 4.8.
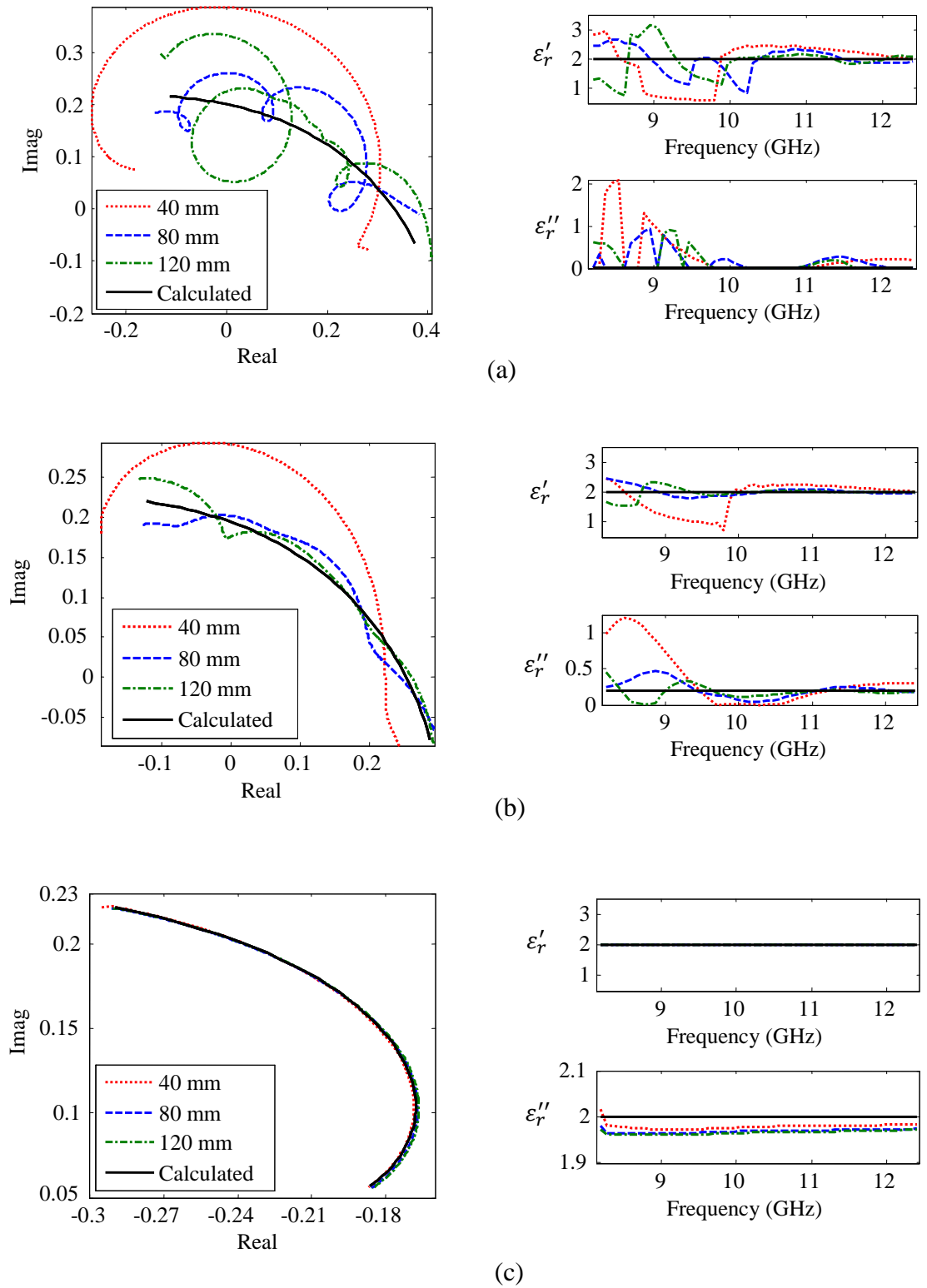
Figure 4.8. Complex reflection coefficient and evaluated material properties for a 5 mm-thick conductor-backed dielectric sheet with permittivity $\varepsilon_r' = 2$ and loss factors of: (a) $\varepsilon_r'' = 0.02$, (b) $\varepsilon_r'' = 0.2$ and (c) $\varepsilon_r'' = 2$.

4.4.3. Open-ended Waveguide Measurements. In order to verify the conclusions drawn from the previous sets of simulation, two measurements were performed. The measurements were performed with standard WR-90 waveguides terminated by a standard UG 135/U flange (41.4 mm x 41.4 mm) and a custom-made square flange with dimensions (152 mm x 152 mm) [28]. The custom-made flange was constructed with a standard UG 135/U flange in which a copper clad dielectric material was cut to form flange extensions. Conductive epoxy was used to attach the flange extensions to the standard waveguide flange. Finally, the conductive epoxy was also used to fill any cracks between the waveguide flange and the extensions, making the transition between the conductors as smooth as possible [28]. A picture of the custom flange can be seen in Figure 4.9.
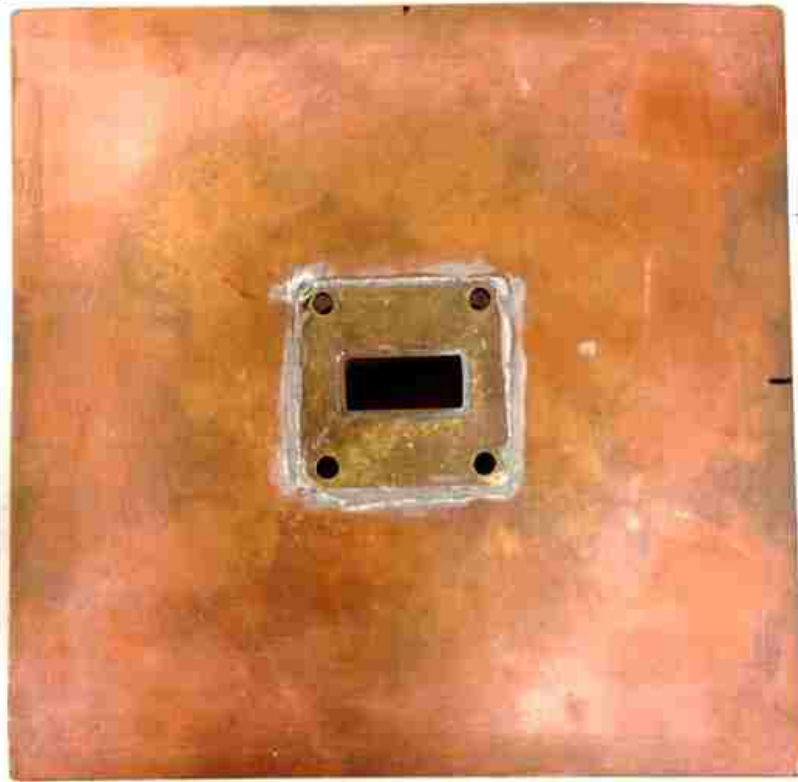
Figure 4.9. Custom-made large flange (152 mm x 152 mm).

The first sample measured was a 4.42 mm-thick rubber composite sheet with $\varepsilon_r = 7.28 - j0.275$ and backed by an infinite half-space of air. The given complex dielectric constant value was measured via the completely-filled waveguide technique and was reported in [28]. The dielectric constant retrieved using the filled waveguide technique showed little variation across the X-band frequency range and thus, was assumed to be constant [28]. To create an infinite half-space of air, the rubber sheet was placed on top of a stiff, low density foam block to add support and rigidity. This stack-up was then suspended over a small anechoic chamber to simulate an infinite half-space of air. A picture of this measurement setup is shown in Figure 4.10. The wooden slats used to hold the measurement setup above the anechoic chamber have been positioned to extend in the direction parallel to the dominant mode electric field to reduce any effect its presence may have on the measurement. For calculating the theoretical reflection coefficient as well as evaluating the complex dielectric constant, the foam block was assumed to have $\varepsilon_r = 1.2 - j1\text{E-}4$. The measured complex reflection coefficient along with the evaluated material parameters can be seen in Figure 4.11.

From the results in Figure 4.11, it can be seen that the measured complex reflection coefficient using the large, custom flange better tracks that of an infinite flange. This can be attributed to the loss in the rubber material. Since the fields reflected from the large flange edges have to travel approximately 56 mm or 5λ (at the mid-band frequency of 10.3GHz and in the dielectric material) longer than the standard flange, their effects on the measured reflection coefficient are much reduced. Consequently, the large custom flange provides a better estimate of the material properties that has a lower standard deviation than the standard flange. The evaluated loss factor for both flanges has large errors. It was previously shown in [28] that this technique is not nearly as accurate at evaluating the loss factor of a material, when compared to permittivity. In addition, it has been shown [28] that the loss factor is typically over-estimated. Part of the over estimation of the loss factor in these measurements may be due to the loss factor that was estimated for and assigned to the foam block.
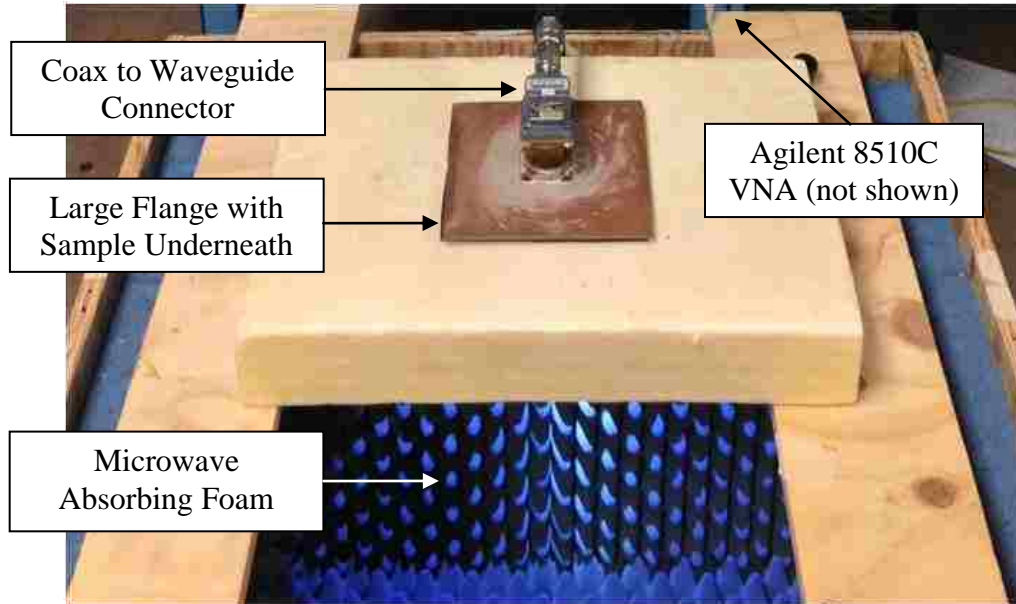
Figure 4.10. Measurement setup to emulate an infinite half-space of air.
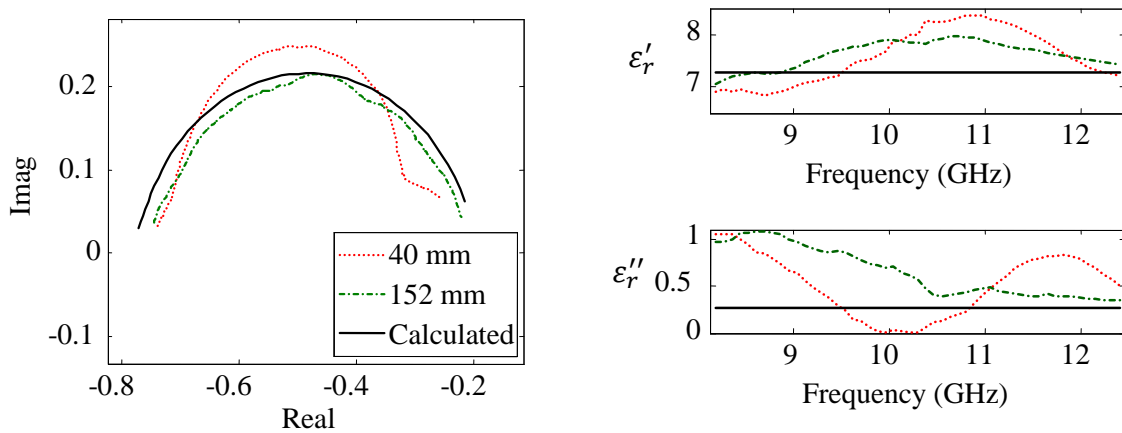
Figure 4.11. Measurement of dielectric sheet backed by an infinite half-space of air.

Next, a 3.175 mm-thick rubber sheet with a complex dielectric constant $\varepsilon_r = 4.8 - j0.17$ and backed by a conductor was measured. The measurement setup was identical to that shown in Figure 4.10, with the exception of a metal plate being inserted on top of the foam block. The measured complex reflection coefficient along with the evaluated complex dielectric constant can be seen in Figure 4.12.
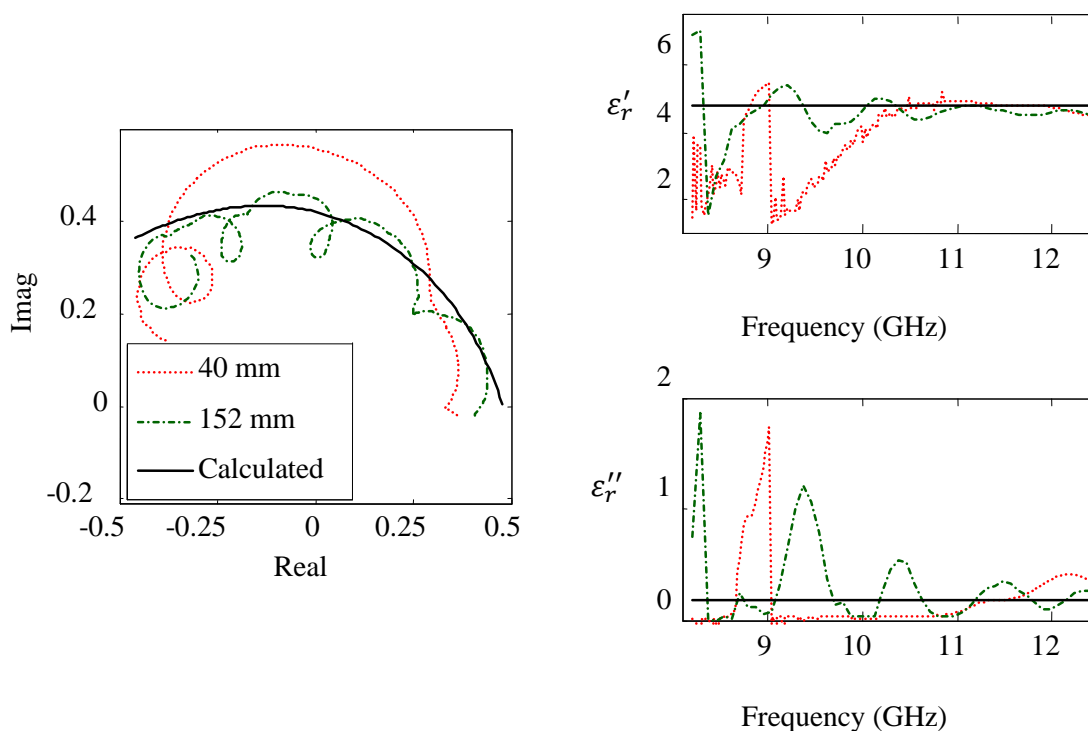
Figure 4.12. Measurement of dielectric sheet backed by a conductor.

The results shown in Figure 4.12 also agree with the simulated data shown previously. The conductor-backed measurement proved to be much more tedious to perform and is shown to have large errors in the measured refection coefficient along with the evaluated material parameters. The standard UG 135/U flange produces the most significant deviations from the actual reflection coefficient, as is expected due to its smaller size. The reflection coefficient from the large flange shows arcs encircling the calculated reflection coefficient that are due to the electrical length between the flange edges and the waveguide aperture (phase variation of the reflected wave). It can be seen that these fast phase variations in the measured reflection coefficient translate to an undulating estimation of material properties.

4.5. PREVIOUS SOLUTIONS TO FINITE-SIZE FLANGE

The problems introduced by a finite-sized flange have been addressed in literature and numerous solutions have been offered. To date, relatively accurate open-ended waveguide measurements have been obtained by either using a very large flange (i.e. > 15λ, where λ is the wavelength at the mid-band frequency) [28]-[29], [39], or by limiting the measurements to lossy materials [37]. However, these solutions limit the capabilities of the open-ended waveguide technique. For instance, many composite materials that are prevalent today are low loss in the microwave and millimeter wave frequency range. For example, any polytetrafluoroethylene (PTFE or Teflon) based material such as microwave printed circuit board materials or glass-fiber reinforced polymers (GFRP) are considered to be low-loss materials [40]. In addition, a sample being tested is required to be locally planar, meaning it must be planar in the region of the flange. By employing a large flange, the region required to be planar becomes significantly larger which has the potential to limit some applications and can be difficult to work with. Complications may arise if the sample size is not larger than the flange where the reflections generated at the dielectric-air interface of the SUT will dominate. Finally, if the large flange is not perfectly flat and in constant contact with the SUT, it has the potential to perturb the electric field distribution and negatively impact the measurement.

Another technique, suggested in [7], utilizes polynomial fitting to model the reflection coefficient of the waveguide. Polynomial fitting has been successful for a waveguide radiating into an air half-space. However, this method is dependent on the dielectric structure being tested. Therefore, for limited applications such as a *known* dielectric sheet, the polynomial fit may be implemented.

It has also been proposed to use a lossy dielectric sheet as a coupling medium to reduce the flange effect by attenuating the reflected signals immediately in front of the aperture [39]. However, this has the potential consequence of reducing the measurement sensitivity due to the extra attenuation introduced by this additional lossy layer. Reducing the sensitivity of the measurement will increase the uncertainty associated with the evaluated material properties, as will be shown in the following subsection.

4.5.1. Lossy Coupling Medium. In order to investigate the potential of using a lossy coupling medium to reduce the effect of a finite-sized flange, simulations very similar to those shown in Section 3 were performed. Using the forward electromagnetic model, the actual reflection coefficient was generated for both a composite structure and the composite structure with an additional lossy coupling layer between it and the waveguide. Next, zero-mean complex Gaussian noise was injected into the two complex reflection coefficients to emulate the noise floor of a calibrated VNA [12], [28]. By adding noise to the reflection coefficient, it introduces a fictitious measurement dynamic range limit (as opposed to simply the numerical precision of the calculations). Next, the material properties of the structure were evaluated at 10 discrete frequencies. The process of adding random noise and recalculating the permittivity was repeated T times (where T is the number of trials). In general, when working with random noise, the greater the number of trials, the more confidence that can be placed in the results. Since the injected noise followed a Gaussian distribution (zero-mean noise), the mean value of the permittivity was expected to converge to the actual permittivity of the material. The standard deviation values represent the uncertainty associated with recalculating the material properties of the structure. More importantly it provides a direct comparison of how the addition of a lossy layer affects the uncertainty of the evaluated material properties.

The results presented here are for a 5-layer structure, designed to mimic an aircraft radome. The structure consisted of three GFRP layers with two low density paper honeycomb layers separating them. The dimensions of each layer along with their complex dielectric constants can be seen in Table 4.1. It was assumed that the structure was backed by an infinite air half-space. The lossy coupling medium that was added to the structure was 5 mm thick with a complex dielectric constant of ($\varepsilon_r = 5 - j0.25$). The material values chosen for the lossy coupling medium were chosen to represent a rubber sheet. The zero-mean complex Gaussian noise was added to the reflection coefficient at -50 dB and -60 dB with respect to a total reflection (magnitude of 1). The noise was added with respect to the maximum reflection coefficient to simulate the noise floor of a VNA. A different approach would be to add noise set a specific signal-to-noise ratio. However,

the former of the two options better represents the noise associated with a reflection coefficient measurement.

Table 4.1 Stack-up of radome structure for coupling medium simulation.

Layer	Material Type	Thickness	ε_r
Layer 1	GFRP	0.762	$3 - j0.050$
Layer 2	Honeycomb	3.023	$1.2 - j0.001$
Layer 3	GFRP	1.295	$3 - j0.050$
Layer 4	Honeycomb	3.023	$1.2 - j0.001$
Layer 5	GFRP	0.762	$3 - j0.050$

Figure 4.13 shows the recalculated average permittivity values for the bottom GFRP skin (Layer 5) along with error bars at ± 3 standard deviations (99% confidence interval) for the structure with and without a lossy coupling medium. There were 50 trials performed for the reflection coefficient with -50 dB noise (Figure 4.13a) and 100 trials performed for the -60 dB case (Figure 4.13b). It can be seen that for both the -50 dB and -60 dB noise powers the mean value of the permittivity is evaluated to be approximately 3, as expected. More importantly, the structure without a lossy coupling medium produces permittivity estimates with smaller uncertainty values across the entire frequency band. These results match expectations and provide a reason to look for an alternative method to reduce the effects of the finite-sized flange without introducing unnecessary loss. In addition, it can be seen that the general shape of the uncertainty envelopes formed by the standard deviations is generally the same between the -60 dB and -50 dB noise. This provides additional confidence in the results.
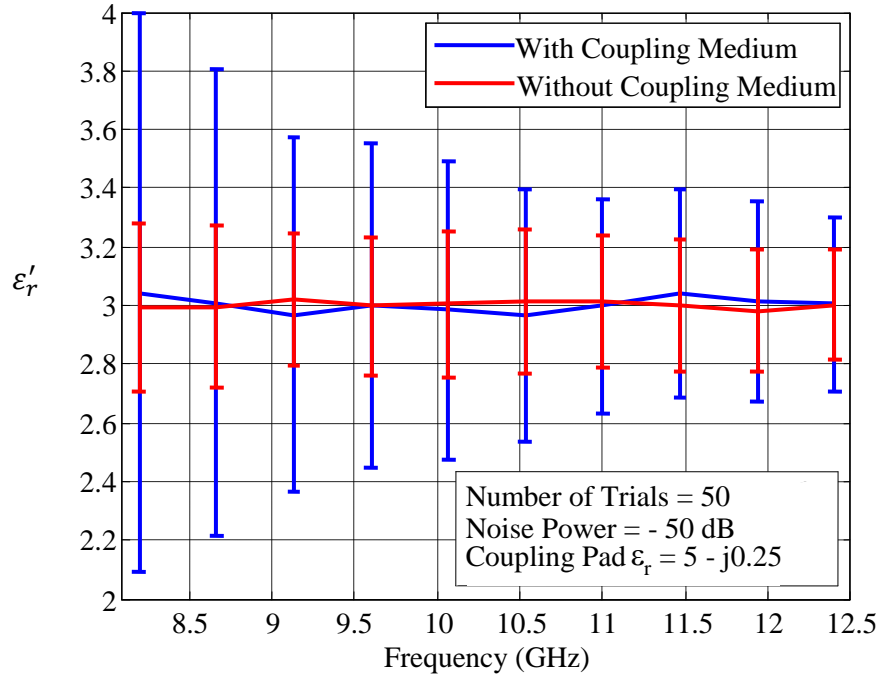
(a)
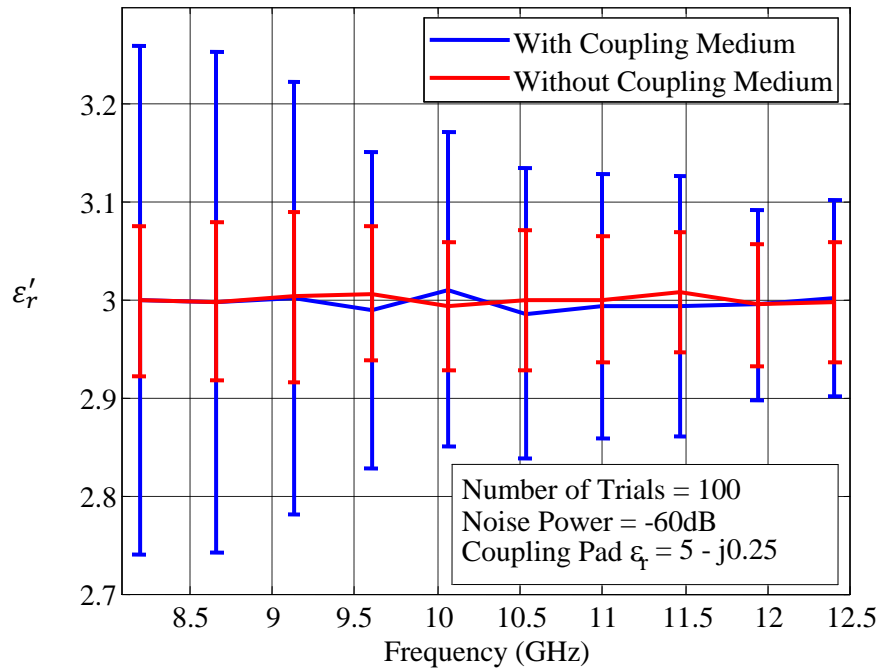
(b)

Figure 4.13. Effect of a lossy coupling medium on the uncertainty in the recalculated permittivity of a five layer low-loss composite structure for: (a) noise power of -50 dB and (b) noise power of -60 dB.

4.6. CONCLUSION

It has been shown that the finite-sized waveguide flange is responsible for errors in the estimate of the complex dielectric constant of a material. This is because the electromagnetic model employed here [28] is assumed to produce the same complex reflection coefficient, referenced to the aperture of the waveguide, as is acquired in measurement. However, it has been shown that a finite-sized waveguide flange and sample introduce reflected fields that are not accounted for in the model. Consequently, when using the forward iterative technique outlined in Section 2 to determine the complex dielectric constant of a dielectric material, these reflections introduce errors. The finite-sized flange causes the most significant errors and tends to mask the effects of a finite-sized SUT.

The flange edges introduce the strongest reflected fields because it plays a role in guiding energy as either surface waves (air-backed cases) or in parallel plate waveguide modes radially away from the aperture. Consequently, when the flange is abruptly terminated a wave impedance mismatch is introduced between the guided waves and the fields radiating out, away from the flange. It is this wave impedance mismatch that generates a reflected wave, propagating back toward the waveguide aperture. These reflected fields are sampled at the aperture along with the expected reflection coefficient and thus introduce differences that are not accounted for in the model.

The solutions to these reflected fields that have been presented in literature limit the capabilities of this technique by making it impractical, less sensitive, or completely avoiding measurements of specific materials. Consequently, an additional solution is needed that takes advantage of the capabilities of this measurement technique without reducing significantly reducing its performance. In the subsequent Sections a novel flange configuration will be presented and shown to markedly reduce the effects of the reflections from the edges of the flange. In addition a comparison of the different variants of the modified flange geometry will be presented.

5. NOVEL WAVEGUIDE FLANGE GEOMETRY

5.1. INTRODUCTION

When using the open-ended waveguide technique for material characterization purposes, it was shown in the previous section that the largest contributor to errors in the estimated material properties is due to the finite-sized waveguide flange [28], [30]. The forward electromagnetic model that is used to evaluate the material properties, given a measured reflection coefficient, assumes the waveguide flange to be infinite in spatial extent. Consequently, the reflected fields generated at the edges of the waveguide flange (as shown in Section 4) introduce deviations from the calculated infinite flange reflection coefficient that may lead to non-negligible errors.

It is possible to account for the geometry of the finite-sized waveguide flange in the electromagnetic model; however, this cannot be accomplished with an analytical solution. Consequently, numerical techniques (e.g., finite-difference time domain or finite element method) would be required to solve for the pertinent equations. The increase in accuracy offered by these methods comes with a significant increase in the required computational resources as well as the computation time. Therefore, a different solution is sought which will not increase the system requirements or the time required for material dielectric and geometrical (thickness) evaluation.

In Section 4, previous solutions to the errors introduced by the finite-sized flange were presented. The first solution given was to avoid measuring low-loss materials [37]. Next, it was proposed to use a waveguide with a relatively large flange so that the fields incident on the discontinuity at the edge of the flange will have a negligible amplitude [7], [28]-[29]. Finally, it was suggested that the utilization of a lossy coupling medium in front of the flange could be help in attenuating the fields near the discontinuities. Nevertheless, implementation of these three solutions still limits or degrades the accuracy of this technique. Using a flange with relatively large dimensions becomes impractical and difficult to work with. In addition, it requires large sample sizes with dimensions as large, or larger, than the flange. Using a lossy coupling medium degrades the sensitivity of the method and increases the uncertainty associated with evaluated material properties.

Consequently, a solution to this problem that does not have severe repercussions on the measurement sensitivity and/or computational requirements was sought. The following section presents the alternative and robust solution of modifying the geometrical configuration of the standard waveguide flange used for these measurements. This technique will be shown to improve the accuracy and capabilities of the open-ended waveguide technique [30]. In Section 4 it was shown that low-loss and thin materials (both air and conductor-backed) have a wave guiding effect on the electromagnetic energy. Consequently, the novel waveguide probe presented here helps to allow the guided fields to efficiently transition away from the guiding structure and into the surrounding environment.

5.2. MODIFIED FLANGE GOALS

Since the electromagnetic model assumes the waveguide to be terminated into an infinite flange, the goal of the novel probe presented here is to emulate the fields of an infinite flange, specifically in the region of the waveguide aperture [30]. In order to accomplish this, the reflected fields from the edges of the waveguide flange must be considerably reduced. This requirement is due to the fact that when the waveguide is terminated in an infinite flange, the fields that are radiated in the lateral directions are assumed to propagate indefinitely as there is no discontinuity or mechanism to generate a reflected field. By emulating an infinite flange, the electromagnetic model will more accurately describe the physical interaction of the electromagnetic fields in the measurement setup. Consequently, the measured reflection coefficient will more closely match that predicted by the forward model and more importantly the material properties will be evaluated with much increased accuracy.

5.3. MODIFIED FLANGE GEOMETRY (2 EDGES)

The largest discontinuity in the electric field is caused by the flange edges that are parallel to the broad dimension of the waveguide aperture. This is true for both air and conductor-backed samples and can be explained by the polarization direction of the dominant mode electric field inside the waveguide. Consequently, these edges are the

foremost concern in designing a probe to achieve the previously mentioned goals [30]. It was shown in Section 4 that the reflections generated at the edges of the flange are due to the wave impedance mismatch between the guided fields (guided by a dielectric waveguide or between the parallel conducting plates) and those radiating into the surrounding medium. Therefore, to achieve an electric field distribution in front of the waveguide flange that mimics that of an infinite flange, a matching technique should be employed to allow these fields to efficiently radiate away from the flange (as opposed to being reflected).

Consequently, a transition section is needed that will gradually transform the wave impedances. This is similar to using a tapered transmission line to match the characteristic impedance of a transmission line with an arbitrary load. In order to achieve this transition, the standard 90°-flange edges have been modified by adding circular cylindrical extensions to the two edges that are parallel to the broad dimension of the waveguide as shown in Figure 5.1. By introducing a round flange edge, the abrupt discontinuity is distributed along the arc of the cylinder which allows for gradual transformation of the wave impedance. As the radius of the cylinder on the edge of the flange increases, the wave impedance transformation becomes more efficient, allowing more energy to radiate away from the flange and not return back to the probing waveguide aperture.

5.3.1. Evaluation of Modified Flange with Two Rounded Edges. To investigate the effectiveness of this technique, CST simulations were performed for WR-90 waveguides operating at 10.3 GHz (mid frequency at X-band, 8.2-12.4 GHz). The waveguides were simulated radiating into a 3 mm-thick dielectric sheet that was backed by both a conductor and an infinite half-space of air. The complex dielectric constant of the sample was chosen to be $\varepsilon_r = 5 - j0.005$, representing a typical low loss polymer. The fact that the material is low in loss presents a worst case scenario where the reflected fields from the flange edges undergo little attenuation. In addition, the lateral dimensions of both the material and the conductor backing were assumed to be infinite.

These simulation were performed for a waveguide with a standard 40 mm x 40 mm flange along with two rounded flanges with base dimensions of Fx = Fy = 40 mm and radii of r = 2.5 mm and 10 mm. A waveguide with an infinite flange was also simulated in CST to provide a comparison between the finite flanges and the fields that are expected in the electromagnetic model. The electric field distribution was also calculated using the electromagnetic model and was seen to be in good agreement with the CST results (not shown here). The results from the CST simulation were presented here so that the four flange configurations could be plotted with the same color scale, providing a one-to-one comparison between the figures.
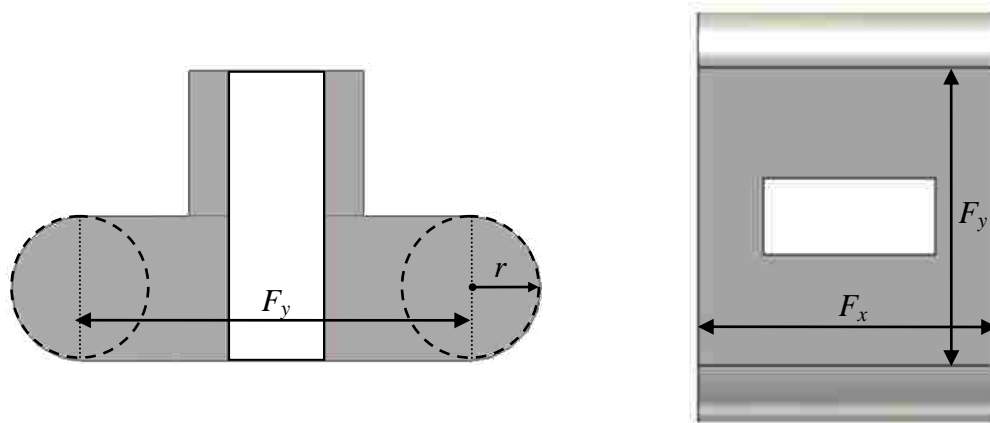
Figure 5.1. Geometry of modified flange with two rounded edges.

Figure 5.2 shows the electric field distribution at a depth of 0.25 mm into the conductor-backed dielectric sheet for the four flange configurations. The electric field distributions have all been plotted on the same scale, allowing for a one-to-one comparison. In Figure 5.2a the electric field for the standard 40 mm x 40 mm flange is shown. As was seen in Section 4, very strong reflections are present at the edges of the flange. These reflections cause strong standing waves in front of the flange that can be approximated as cavity modes. When compared with the electric field distribution of an infinite flange (Figure 5.2d) it can be seen that there is no real resemblance between the two field distributions. Moreover, the electric field around the waveguide aperture, which

is the foremost contributor to the reflection coefficient, is strongly perturbed (as compared to the infinite flange). In Table 1, the complex reflection coefficient for each flange configuration is provided, along with the error associated with it. The error is defined as the Euclidian distance on the complex plane between the reflection coefficient for the waveguide terminated in a finite-sized flange and an infinite flange. This is expressed as,

$$error\left|\Gamma\left(f_i\right)\right|=\left|\Gamma_c\left(f_i\right)-\Gamma_f\left(f_i\right)\right| \tag{10}$$

where Γ_c is the reflection coefficient for an infinite flange, Γ_f is the reflection coefficient for the finite-sized flanges, and f_i is the frequency index (in this example the quantities are scalars as only one frequency was evaluated). In addition, the percent error associated with these values is defined as:

$$\%error\left|\Gamma\left(f_i\right)\right|=100\sum_{i=1}^{N_f}\frac{\left|\Gamma_c\left(f_i\right)-\Gamma_f\left(f_i\right)\right|}{\left|\Gamma_c\left(f_i\right)\right|} \tag{11}$$

where N_f is the total number of frequency points. For this specific structure, the standard flange is shown to introduce an error of 46% in the simulated reflection coefficient.

Figures 5.2b,c show the electric field distribution for the rounded flanges with radii $r = 2.5$ and 10 mm, respectively. In Figure 5.2b, the small radius of 2.5 mm can be seen to have a large impact on the electric field distribution. The amplitude of the standing waves, which is a function of the strength of the reflected fields from the flange edges, is notable reduced. In addition, the strong discontinuity at the edges of the flange has also been reduced; allowing the electric to radiate away from the flange more efficiently. The subtle rounding at the edges of the flange is shown to reduce the error in the reflection coefficient from 46% to approximately 19%.
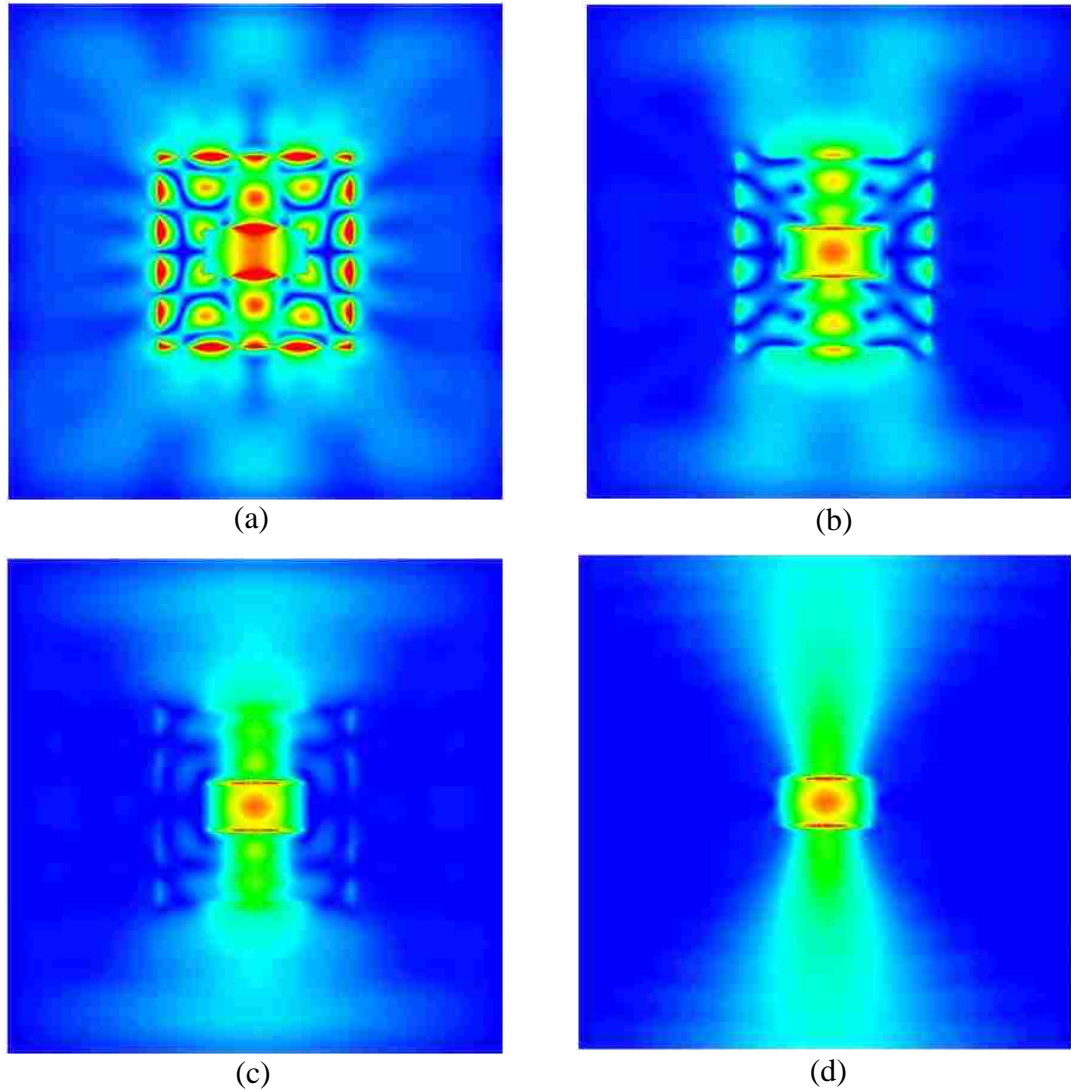
Figure 5.2. Electric field distribution at 0.25 mm into a 3 mm-thick conductor-backed dielectric sheet with complex dielectric constant ε_r = 5 – j0.005 for: (a) standard flange, (b) rounded flange with r = 5 mm, (c) rounded flange with r = 10 mm, and (d) infinite flange.

Table 5.1 Reflection coefficient values and errors: conductor-backed.

Flange Configuration	Γ	$|\Gamma_c - \Gamma_f|$	Percent Error
Standard	0.1857 + j0.3899	0.2094	45.6
r = 2.5 mm	0.0729 + j0.4498	0.0854	18.6
r = 10 mm	0.0224 + j0.4439	0.0351	7.6
Infinite	-0.0121 + j0.4585	-	-

Finally, in Figure 5.2c, the electric field in front of the rounded flange with a radius of 10 mm is shown to substantially reduce the discontinuity at the flange edges. The electric field distribution much more closely resembles that of an infinite flange. The interference pattern of the reflected waves has been significantly reduced to a negligible level. In addition, it can be seen that the tapered transition allowed an increased level of radiation from the flange edges. In this scenario, the radiation from the flange edges describes the fields that efficiently transition from in front of the flange and propagate away from it. The radiated fields are beneficial in helping to emulate the fields of an infinite flange, assuming they are not redirected back toward the waveguide by reflections/scattering from nearby objects. By increasing the radius to 10 mm, the error in the reflection coefficient was further reduced to 7.6%.

Figure 5.3 presents the electric field distributions for the same flange configurations as before, radiating into an air-backed dielectric sheet with identical properties as the previous scenario. Figure 5.3a shows the electric field distribution in front of a standard 40 mm x 40 mm flange. Once again there is a strong discontinuity present at the flange edges. The discontinuity as well as the interference pattern from the reflected waves is not as strong as compared to the conductor-backed case due to the difference in the field structures (shown in Section 4). However, when compared with the electric field distribution for an infinite flange, as shown in Figure 5.3d, the discontinuity due to the flange edges is quite apparent. In Table 2 the simulated complex reflection coefficient and error values for all four flange configurations are presented. The standard flange produces the largest error in the reflection coefficient with a 7.6% deviation from the infinite flange case. Figures 5.3b,c correspond to the rounded flange edges with radii of 2.5 mm and 10 mm, respectively. As was true for the conductor-backed case, when the radius of the flange edges is increased, the electric field distribution is shown to become more like that of an infinite flange. In addition, the error in the simulated reflection coefficient is shown to monotonically decrease as the flange edge radius is increased.
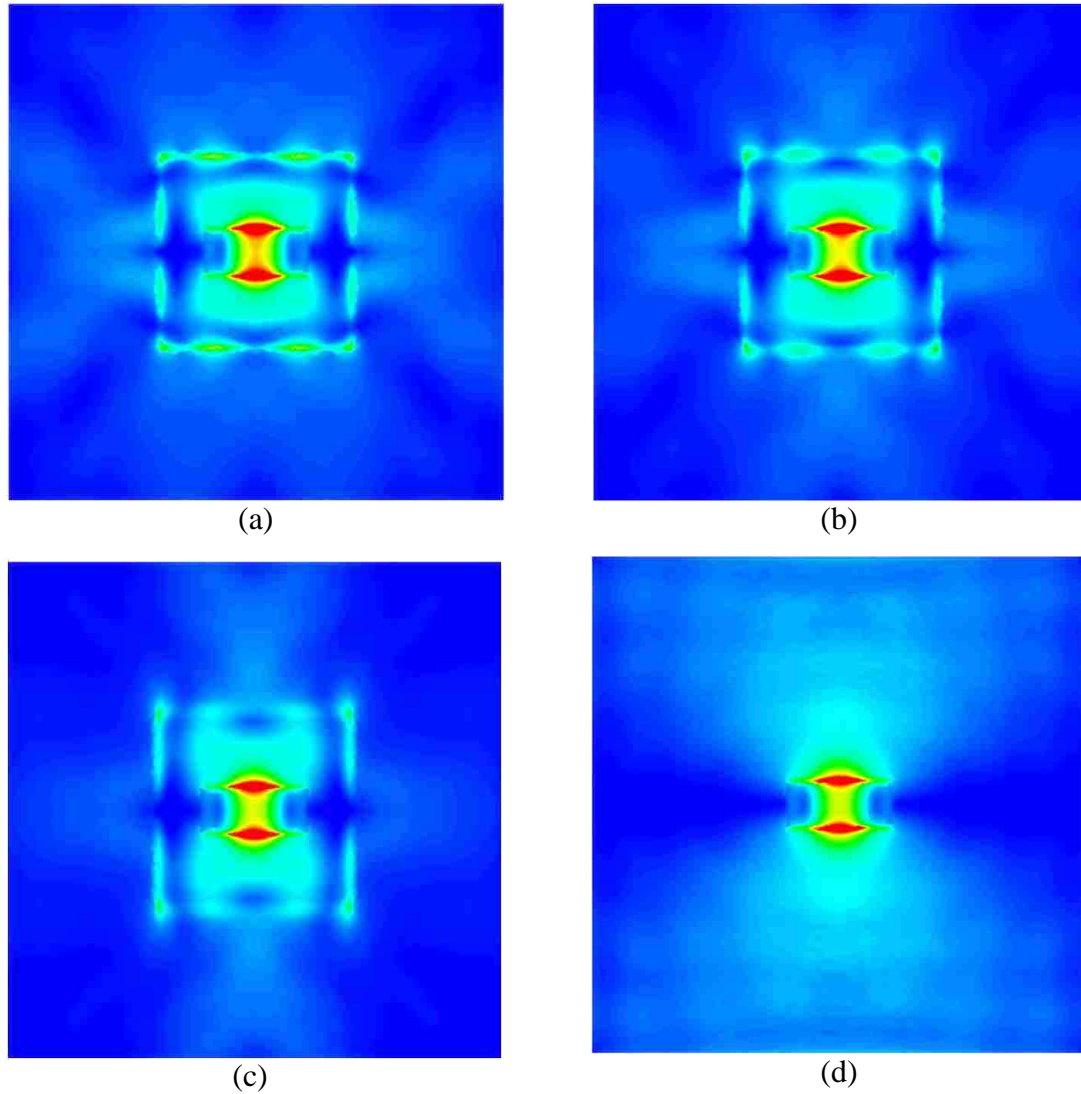
Figure 5.3. Electric field distribution at 0.25 mm into a 3 mm-thick air-backed dielectric sheet with complex dielectric constant $\varepsilon_r = 5 - j0.005$ for: (a) standard flange, (b) rounded flange with $r = 5$ mm, (c) rounded flange with $r = 10$ mm, and (d) infinite flange.

Table 5.2 Reflection coefficient values and errors: air-backed.

Flange Configuration	Γ	$|\Gamma_c - \Gamma_f|$	Percent Error
Standard	-0.6472 - j0.1658	0.0529	7.6
$r = 2.5$ mm	-0.6631 - j0.1690	0.0451	6.4
$r = 10$ mm	-0.6801 - j0.1572	0.0275	3.9
Infinite	-0.6866 - j0.1305	-	-

However, for both the conductor-backed and the air-backed dielectric, the (vertical) flange edges parallel to the electric field polarization vector are shown to perturb the electric field. These perturbations actually become stronger than those along the horizontal edges for the rounded flange with $r = 10$ mm radiating into the air-backed sample. Consequently, the next step in the probe design must take into account all four edges of the flange, as opposed to only two. In addition to rounding all four edges of the flange, another advantage may be gained by generalizing the cross-sectional shape of the flange edges from circular to generally elliptical. This provides more control over the transition geometry which will be shown to improve the accuracy of the simulated reflection coefficient.

5.4. MODIFIED FLANGE GEOMETRY (4 EDGES)

The geometry of the novel waveguide probe that has been designed to further improve the flange with two rounded edges is shown in Figure 5.4. The waveguide aperture dimensions are denoted by a and b, corresponding to the broad and narrow dimensions of the waveguide, respectively. The edge geometry of the flange has been modified by replacing all four standard right angle edges with a generally elliptical cross-section, with radii r_t and r_p, which provide a smoother geometrical transition at the edges. Radius, r_t, denotes the lateral directions which are transverse to (r_p denotes parallel to) the direction of wave propagation in the waveguide. This elliptically-tapered geometry significantly reduces the unwanted reflections at the flange edges, as will be shown later. It may be possible to determine an optimum flange configuration where the general geometries of the four edges on the front of the flange (plane of the aperture) and the four edges of the back of the flange (where the feeding waveguide meets the flange) are not identical. However, the benefits are expected to be marginal. Consequently, all flange edges are assumed to have identical radii. Dimensions F_x (H-plane direction) and F_y (E-plane direction) denote the footprint of the probe while F_t represents the thickness of the flange. The location of the screw holes align with those of a standard waveguide flange, which accommodates VNA calibration referenced to the probing waveguide aperture.

5.4.1. Comparison Between 2 and 4 Rounded Edges. In order to evaluate the advantages of rounding all four edges of the waveguide flange, an additional CST simulation was performed for both the conductor and the air-backed dielectric sample from the last section. The material properties were identical to the previous simulations (3 mm thick with $\varepsilon_r = 5 - j0.005$) and the dimensions of the new flange with all four edges rounded were chosen to be comparable to the flange with two rounded edges and a radius of 10 mm. Consequently, a WR-90 waveguide operating at 10.3 GHz was employed. The edge rounding radii of the flange was $r_t = r_p = 10$ mm (circular cross-section), and the overall flange thickness, $F_t = 20$ mm. The dimensions of the flat face of the flange that is placed against the sample were identical to the previous simulation (40 mm x 40 mm). For these two simulations the screw holes on the flange were filled with PEC because the simulations for the flange with two rounded edges did not include screw holes.
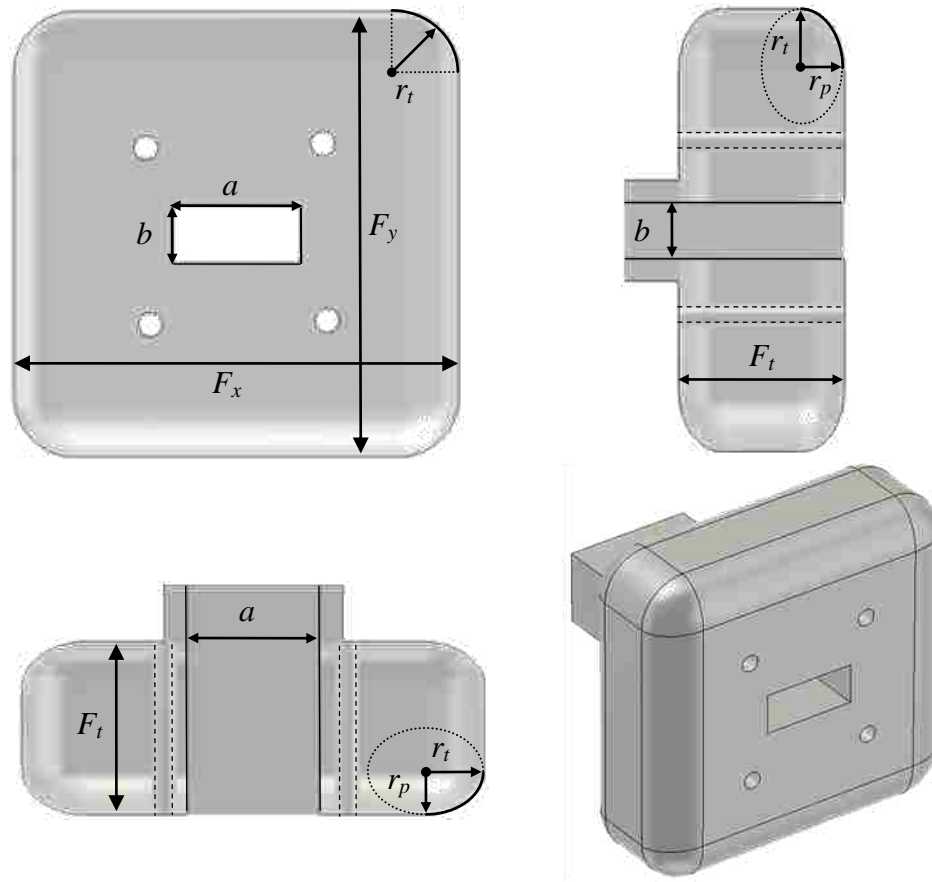
Figure 5.4. Geometry of the modified flange.

Figure 5.5 shows the electric field distribution at a depth of 0.25 mm into the dielectric sheet for the new flange configuration, radiating into the conductor and air-backed dielectric samples (Figures 5.5a,d respectively). The electric field distribution for the previous flange configuration employing two rounded edges (r = 10 mm) has been repeated for both the conductor (Figure 5.5b) and air-backed (Figure 5.5e) cases for comparison purposes. In addition, the field distribution for an infinite flange has also been repeated (Figure 5.5c,f). It can be seen that for both conductor and air-backed cases, the discontinuity along the vertical edges and at the corners of the flange has been further reduced by rounding all four edges. This effect is most noticeable for the conductor-backed case where the discontinuities in the H-plane direction have been removed. However, it can be seen that there is still a small interference pattern in the E-plane direction. Although the rounded edge significantly reduces the reflected fields it does not completely eliminate them. The improvements in the field distribution for the air-backed case are much more subtle; however, that is expected as the deviations due to the finite-sized flanges were much smaller than for the conductor-backed case (Tables 1 and 2). Regardless, the electric field distribution for both cases is shown to improve when all four edges of the flange are rounded.

5.4.1. Evalulation of the Flange Geometry. To further study the influence of the finite flange along with the improvements of the modified flange geometry shown in Figure 5.4, CST was used to simulate a probe with an infinite, standard, and rounded flange. The simulations were performed with the probes radiating into the same 3 mm-thick conductor-backed dielectric sheet (ε_r = 5 - j0.005) as before. The illuminating waveguides were standard WR-90 X-band waveguides (8.2-12.4 GHz) with a cross-section dimension of 22.86 mm x 10.16 mm. The standard flange dimensions were F_x = F_y = 40 mm, with an overall thickness of F_t = 4 mm. The rounded flange had radii r_t = r_p = 10 mm (corresponding to edges with a circular cross-section), a footprint of F_x = F_y = 60 mm, and a flange thickness of F_t = 20 mm. As will be seen later, these dimensions correspond to those for a custom-designed flange used in measurements. In addition, circular edges were employed for simplicity of design and machining while still providing the desired effects.
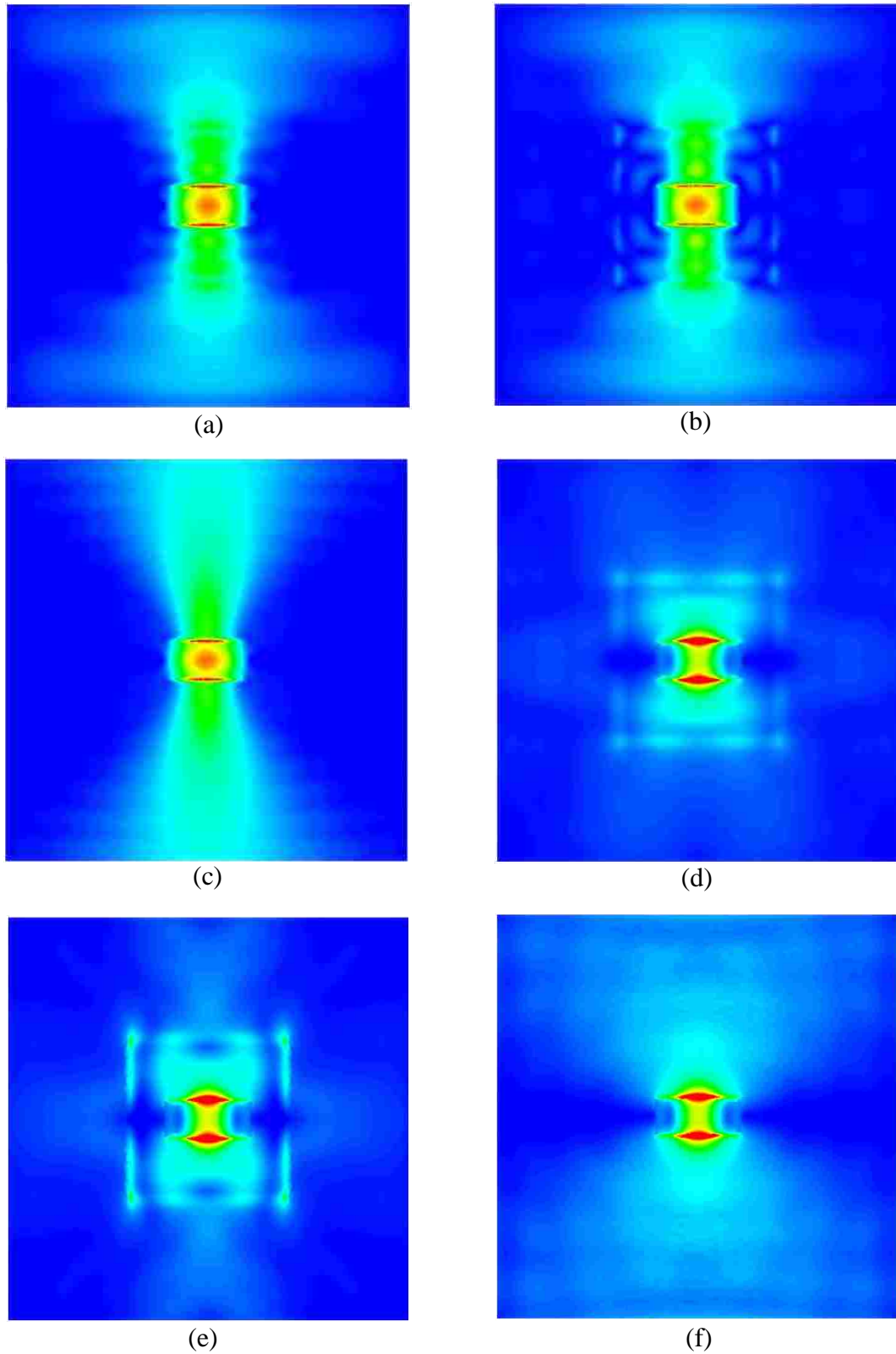
Figure 5.5. Electric field distribution for conductor (a-c) and air-backed (d-f) dielectric sheets for a flange with four rounded edges (a), (d), two rounded edges (b), (e), and infinite spatial extent (c), (f).

5.4.2. Effect of Flange Modification on Surface Current Density. Figure 5.6 shows the simulated surface current densities on the three waveguide flanges radiating into the previously mentioned conductor-backed dielectric sheet (ε_r = 5 - j0.005) at 8.2 GHz, 10.3 GHz and 12.4 GHz, respectively. The current densities in Figure 5.6 are all normalized to the same scale, providing a one-to-one comparison between the different geometries. The surface current densities for the infinite flange (Figures. 5.6a,d,g) have been truncated so that they could be plotted with the same aperture size as the two other flanges. For the infinite flange and for all three frequencies, the current density smoothly transitions away from the aperture. The current distribution is generally frequency independent with the exception that as the frequency increases the majority of the current becomes confined to a slightly narrower region on the flange. Also, the majority of the current flow (i.e., vertically in Figures 5.6a,d,g) corresponds to the direction of the TE_{10} (dominant waveguide mode) electric field polarization, as expected.

The surface current densities on the standard flange (Figures 5.6b,e,h) do not closely match those of the infinite flange. The pronounced variations in the current density distribution are due to the strong reflections generated by the discontinuity at the flange edges. In addition, albeit to a lesser extent, the screw holes on the flange perturb the current density path as well. The coherent addition of the multiple reflected waves (from the flange edges and screw holes) creates an interference pattern that is unique for each frequency. In addition, maximum current density perturbations appear at all four edges for 8.2 GHz and 10.3 GHz. At the upper end of the frequency band the amplitude of the standing waves are reduced and are predominately in the direction of the TE_{10} mode electric field polarization. This is due to the fact that the flange appears electrically larger (the operating wavelength is shorter) and, as was seen for the infinite flange case, the current distribution at higher frequencies tends to concentrate in a narrower region on the flange. Observation of the surface current density on the standard flange shows that the effects of the finite-sized flange are strongly dependent on the operating frequency.
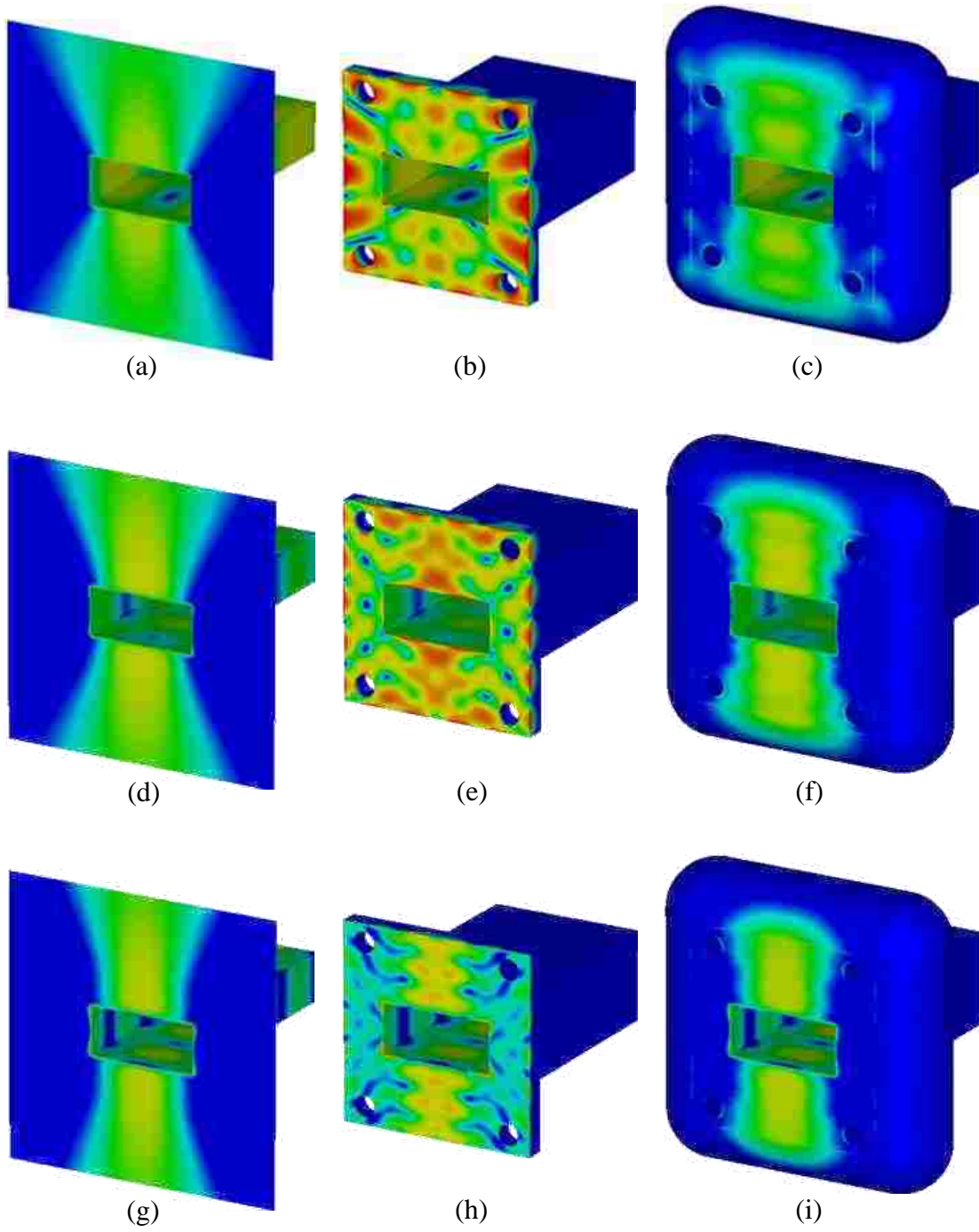
Figure 5.6. Surface current densities on infinite-, standard-, and rounded-flange waveguide probes at: 8.2 GHz (a-c), 10.3 GHz (d-f), and 12.4 GHz (g-i).

For the rounded flange, the current density distributions, for all frequencies, closely mimic those on the infinite flange, as desired. The results show that the variations in the current density in the H-plane direction have been removed across the entire frequency band, as compared to the standard flange. This is due to the fact that the scattering edges were gradually transitioned, thereby allowing the current to flow smoothly onto the rounded edges. These edges effectively create a tapered impedance match, thereby allowing the electric (and magnetic fields) to more efficiently radiate out and away from the sides of the flange as opposed to being reflected back toward the probing waveguide aperture. It must be noted that at 8.2 GHz, corresponding to the lower limit of the operating frequency band, indications of standing waves are present in the E-plane direction but with much smaller amplitudes compared to the standard flange. In addition, at this frequency, only slight surface currents can be seen at the corners of the rounded flange and along the vertical edges, removing the discontinuity that was present when only two edges of the flange were rounded. The screw holes on the rounded flange also cause a minor disturbance to the current density. However, the advantage of being able to directly connect this rounded-flange probe to waveguide calibration standards outweighs the field perturbations that are introduced by the holes. Finally, it is evident that by rounding the edges of the waveguide flange the induced surface current density on the finite-sized flange much more closely emulates the induced surface current density on an infinite flange.

5.4.1. Effect of Flange Modification on Electric Field Distribution. Figure 5.7 shows the magnitude of the electric field evaluated on a line passing directly under the center of the waveguide aperture and normalized to the maximum magnitude of the electric field for an infinite flange along this same line. In addition to the previously-shown standard and circularly rounded ($r_t = r_p = 10$ mm) flanges, the results for a rounded flange with a footprint indicated by $F_x = F_y = 60$ mm and radii rt = 10 mm, rp = 5 mm (corresponding to an ellipse with an axial ratio of 2) is also included in Figure 5.7. These results were evaluated at a depth of 1.5 mm into the same 3 mm-thick, conductor-backed, dielectric sheet ($\varepsilon_r = 5 - j0.005$) at a frequency of 10.3 GHz. The magnitude of the electric field for a flange with infinite spatial extent has also been included for comparison. The standing waves introduced by the flange discontinuity, as was shown in

Figure 5.6, are a function of frequency with the strongest deviations occurring at the lower edge of the band. The mid-band frequency of 10.3 GHz was chosen to give a representative view of the typical electric field deviations that can be expected. The solid bar at the bottom of Figures 5.7a,b illustrates the physical size of the standard flange while the dashed lines show the footprint of the circular and elliptical flanges. The cutout in the solid black bar shows the location of the waveguide aperture.

The results shown in Figure 5.7a were evaluated along a line parallel to the direction of the dominant waveguide mode (TE_{10}) electric field polarization (E-plane). The magnitude of the electric field, simulated for a standard flange, shows that the abrupt discontinuity at the flange edges creates a strong reflected wave that eventually enters the probing waveguide as part of the overall reflected wave. This discontinuity causes the electric field directly in front of the standard flange ($\pm$ 20 mm) to be considerably different than that for an infinite flange with maximum deviations of more than 50% the field strength of an infinite flange. More importantly, the reflected waves have perturbed the electric field directly in front of the aperture causing noticeably higher amplitude than for the infinite flange case, which translates to a substantial difference in the measured reflection coefficient at the aperture, as will be shown later.

The magnitude of the electric fields for both the circularly and the elliptically rounded flanges much more closely follow the magnitude of the electric field for the infinite flange. For these flanges, the amplitude of the standing waves directly in front of the flanges is significantly decreased (maximum deviations of approximately 8% from the infinite flange case) and the field distribution directly in front of the aperture is very similar to that of the infinite flange. Outside the edges of the finite flanges, for both the standard and the rounded edges, the electric field intensities significantly deviate from those of the infinite flange. This is due to the fact that the parallel plate guiding structure between the flange and the conductor backing is no longer present in this region, as compared to the infinite flange. Consequently, the fields are no longer bounded within the dielectric sheet and are able to propagate as surface waves in the dielectric and radiate into free-space around the probe.

Figure 5.7b shows the magnitude of the electric field on a line perpendicular to the direction of the TE_{10} electric field (H-plane). Again, the standard flange displays an

average electric field intensity that significantly deviates from both the infinite and the rounded flanges. There is a noticeable increase in field strength outside the footprint of the standard flange, which is representative of the scattered field caused by the current maxima along the edges of the flange (Figure 5.6e). Both rounded flanges are shown to closely match the fields of the infinite flange especially at the aperture location, which is the foremost contributor to any measured reflection coefficient. However, the electric fields for all the finite-sized flanges show less variation in this direction. This can be attributed to the radiation pattern of the open-ended waveguide as the majority of the energy is directed along the E-plane direction as opposed to the H-plane direction.

5.4.1. Impact of Flange Dimensions on Simulated Complex Reflection Coefficient. In order to further investigate the relationship between the radii of the flange edges on the simulated reflection coefficient, CST simulations were performed for an open-ended waveguide radiating into a 1.52 mm-thick conductor-backed dielectric sheet with a relative dielectric constant of ($\varepsilon_r = 3.3 - j0.0025$) and for several flange configurations. This was chosen to model a typical microwave printed circuit board material. First, the X-band waveguide probe (WR-90) was assumed to have edges with circular cross sections (rt = rp), while the effect of overall flange dimensions (Fx = Fy) of 60 mm, 80 mm, and 120 mm were investigated. These dimensions correspond to Fx = Fy of 3.75λ, 5.0λ and 7.5λ (normalized to the mid-band wavelength in the dielectric). The overall flange thickness, Ft, was 20 mm and the circular edge radius was varied from 2 mm to 10 mm. The error in the simulated reflection coefficient, as a function of frequency, is defined as the Euclidian distance between the reflection coefficient for an infinite flange and the reflection coefficient for a finite-sized flange on the complex plane, as was given in (1).
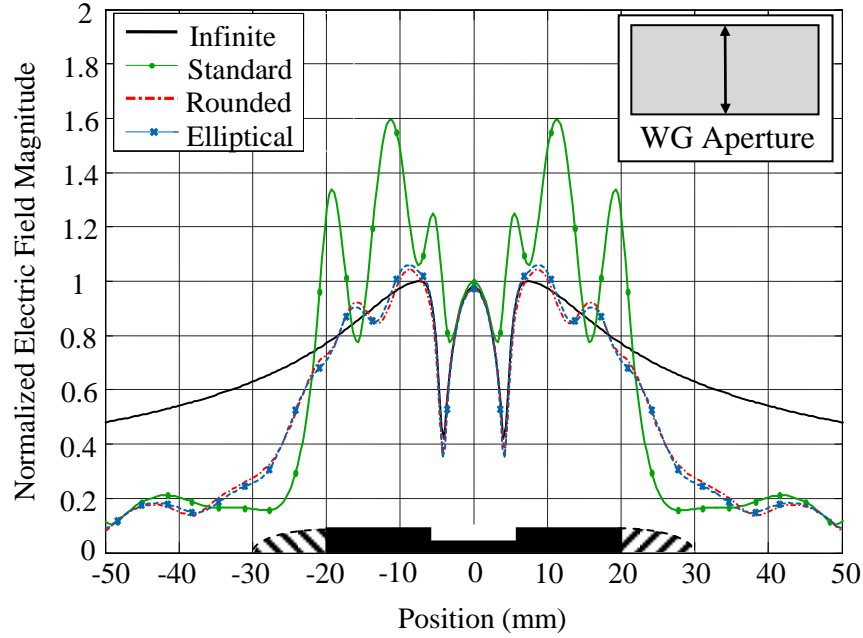
(a)
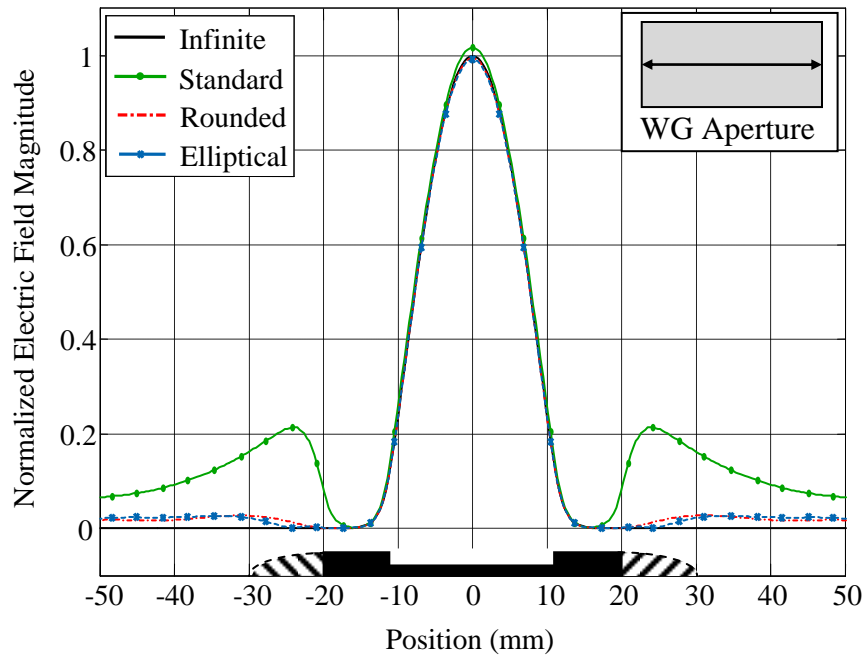
(b)

Figure 5.7. 1D-slice of the electric field 1.5 mm into a 3 mm-thick conductor-backed dielectric sheet at 10.3 GHz across: a) narrow dimension of the waveguide aperture and b) broad dimension of the waveguide aperture.

Figure 5.8 shows the error versus frequency for the flange with four different circular edge radii, and an overall size of 60 mm x 60 mm. A radius of (0λ) corresponds to a standard 90°-edge. These results show that the error in the reflection coefficient, especially for flanges with little or no rounding on the edges, is highly frequency dependent. This frequency dependence stems from the unique standing wave pattern that is set up in front of the flange (see Figure 5.2a). Furthermore, it can be seen that as the radius of the circular edges increases, the magnitude of errors decrease and show less variation across the frequency band. This can be attributed to the impedance transformation that allows the fields to more efficiently radiate away from the flange. In addition, the tapered edges provide a broadband impedance match which helps to reduce the frequency dependence of the errors. For $F_x = F_y = 80$ mm and 120 mm, similar behaviors were observed (not shown here).
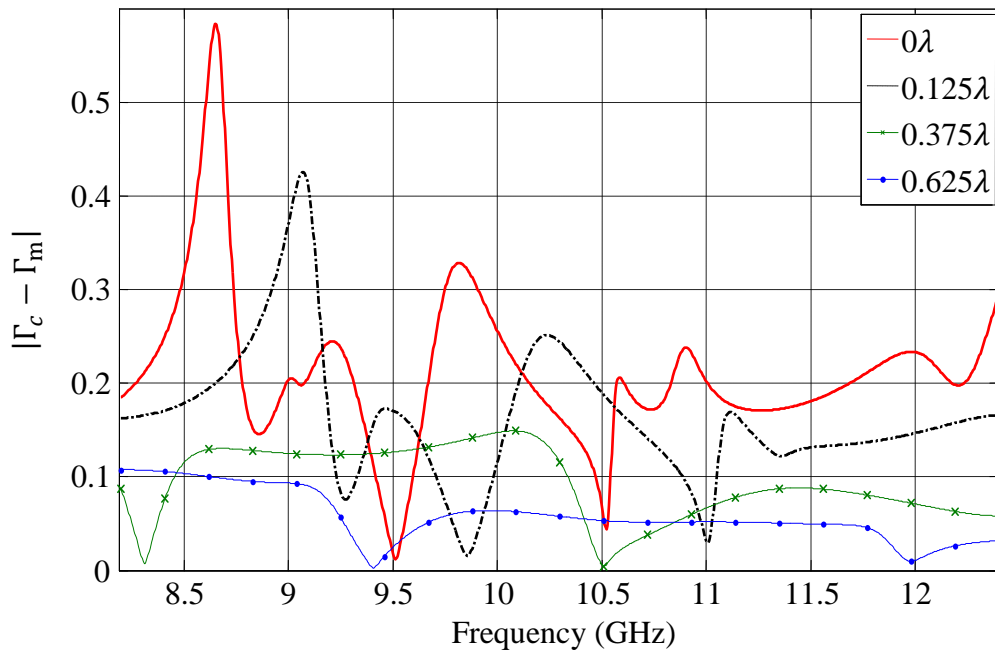
Figure 5.8. Error in the simulated reflection coefficient for a rounded flange with $F_x = F_y = 60$ mm for various flange edge radii ($r_t = r_p$)

In addition to edges with circular cross-sections, elliptical edges were evaluated for three flanges with the same F_x, F_y, and F_t dimensions as in the previous case. Radius r_t was held constant at 10 mm while the radius r_p was varied. Figure 5.9 shows the root-mean-square (RMS) error for the simulated vector reflection coefficient for both the circular and the elliptical rounded flanges with respect to that of an infinite flange, terminated in the same dielectric structure as before. The RMS error is defined as:

$$RMS\,Error\,|\Gamma| = \sqrt{\frac{1}{N_f}\sum_f \left(\left|\Gamma_c(f_i) - \Gamma_f(f_i)\right|^2\right)} \qquad (12)$$

The RMS errors for the circular edges are denoted by a solid line while the RMS errors for the elliptical edges are denoted with a dashed line. The circular and elliptical edged RMS errors are equal for a standard flange (i.e., 0λ), and for $r_p = 0.635\lambda$ where the elliptical cross-section becomes a circular cross-section ($r_t = r_p$). The RMS error for the circular edges is shown to monotonically decrease. As the circular radius is increased, the edge of the flange becomes smoother and, consequently, provides a more gradual wave impedance transition. However, the RMS error for the elliptical edges does not monotonically decrease and is shown to reach a minimum for a value of approximately 0.3λ (an axial ratio of approximately 2). This is due to the fact that the elliptical shape provides the most gradual impedance transition across the frequency band for these flange dimensions. However, the taper with these dimensions is optimized for these material properties. For a dielectric sheet with a different thickness and relative dielectric constant, the taper dimensions may have to be changed to obtain minimum RMS error.

The optimal flange rounding parameters from Figure 5.9 were used to investigate the effect of the overall flange dimensions on the complex reflection coefficient. Simulations were performed for a flange with $F_t = 20$ mm, $r_t = 10$ mm and $r_p = 5$ mm radiating into the same conductor-backed dielectric structure ($\varepsilon_r = 3.3 - j0.0025$). In addition to $\varepsilon_r'' = 0.0025$, two other relative loss factors of 0.05 and 0.1 were also simulated, as shown in Figure 5.10. The results indicate that the RMS error in the reflection coefficient does not monotonically decrease as a function of increasing flange size. Although the signal reflected from the edges of the flange travels a longer electrical

distance and therefore experiences higher attenuation, this does not ensure that the standing wave pattern generated from the edge reflections will have a reduced influence on the reflection coefficient. The peaks in error correspond to flange dimensions whose standing wave patterns generate maxima directly in front of the waveguide aperture. It can be seen, however, that as the loss factor increases the RMS error for a specific flange size decreases. For a specific standing wave pattern, increasing the loss dampens the amplitude of this interference.
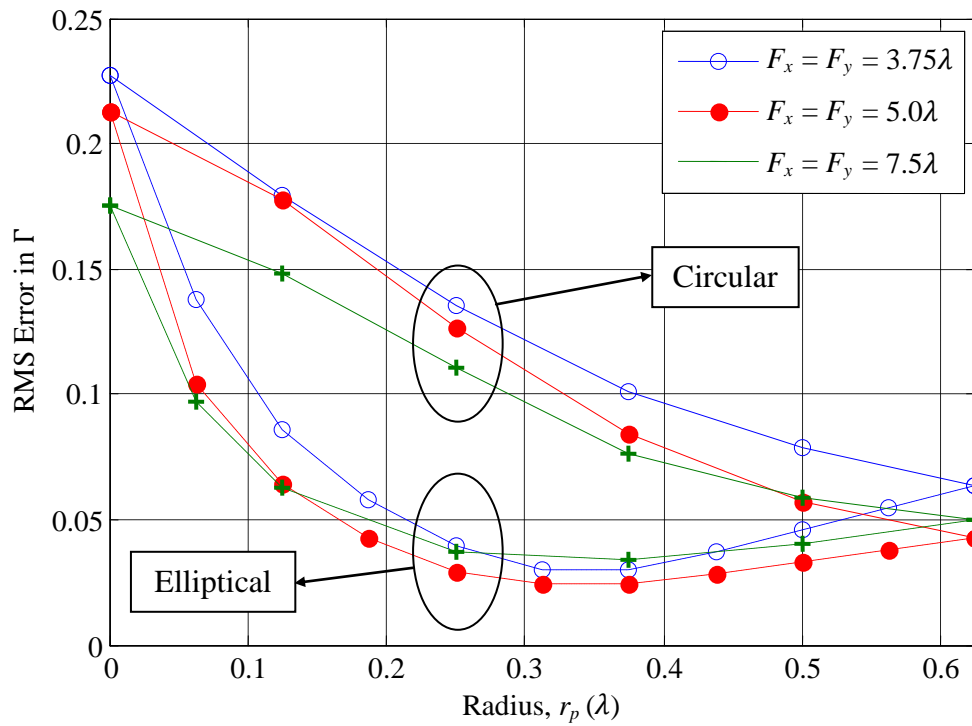
Figure 5.9. RMS error in reflection coefficient for waveguide flanges with circular (solid line) and elliptical (dashed) cross-sections for varied values of r_p.
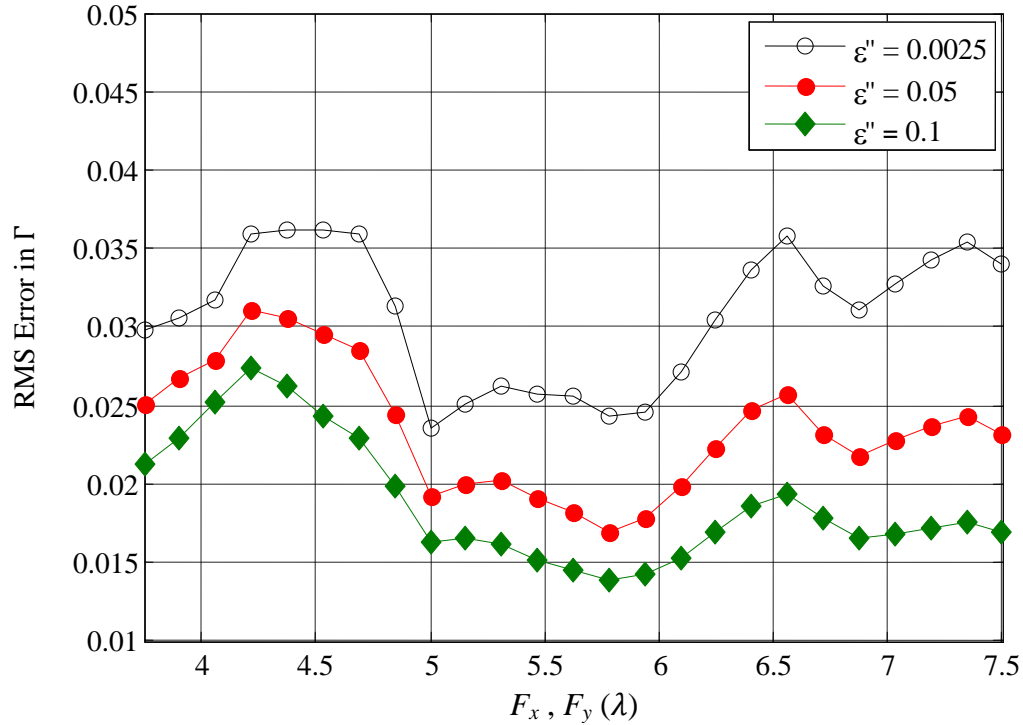
Figure 5.10. RMS error in reflection coefficient for varying flange sizes and loss factors.

5.5. SIMULATED MEASUREMENT OF RUBBER SHEET

To further investigate the effectiveness of the new waveguide probe shown in Figure 5.4, an additional conductor-backed scenario was simulated in the X-band frequency range and for a 3.175 mm-thick dielectric sheet with ($\varepsilon_r = 4.8 - j0.17$), corresponding to a rubber compound available in the laboratory whose dielectric properties were measured using the method in [8]. The simulation was performed for two standard waveguide flanges that will be referred to as standard ($F_x = F_y = 40$ mm) and large ($F_x = F_y = 152$ mm) along with two circularly rounded waveguide flanges with radii, $r_t = r_p = 10$ mm that will be referred to as small rounded ($F_x = F_y = 60$ mm) and large rounded ($F_x = F_y = 100$ mm). These flanges were later manufactured for conducting subsequent measurements. The dielectric sheet and conductor backing are assumed to be infinite in spatial extent.

Figure 5.11 presents the simulated complex reflection coefficient at the aperture of each waveguide terminated in the respective flanges (shown on the complex plane). The reflection coefficient for a flange with infinite spatial extent is also included for comparison. It can be seen that the reflection coefficient for the waveguide terminated in a standard flange has the largest deviations from that of an infinite flange. The reflection coefficient for the waveguide with a large standard flange also deviates from that of an infinite flange but with less deviation compared to the standard flange. This is due to the increased attenuation of the reflected waves as they travel a larger electrical distance between the flange edges and the waveguide aperture. In addition, the repetitive arcs in the reflection coefficient are due to the rapid phase variation of the reflected signal as it travels to and from the flange edges. Finally, it can be seen that the small and large rounded flanges provide increasingly accurate reflection coefficients, respectively. Herein lies the major advantage of the rounded flange edges: since the reflected wave due to the discontinuity at the flange edges is significantly reduced the result is a more accurate measurement of reflection coefficient.
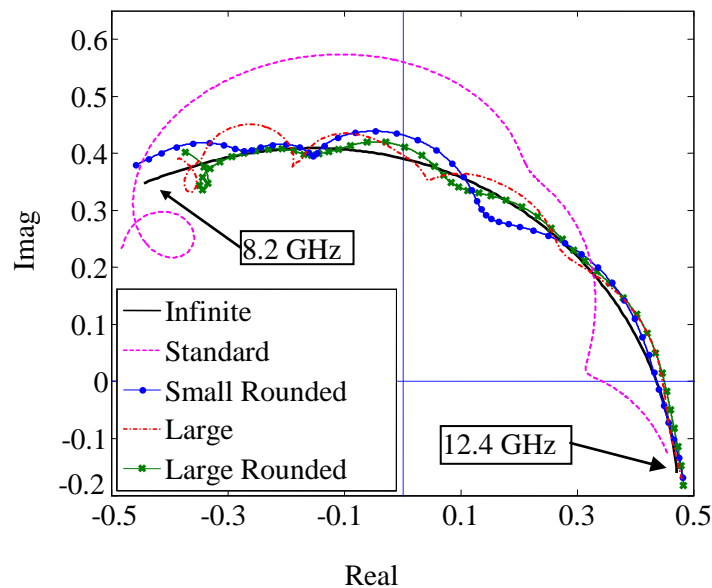
Figure 5.11. Simulated reflection coefficient of a 3.175 mm-thick conductor-backed dielectric sheet with $\varepsilon_r = 4.8 - j0.17$.

Figure 5.12 shows the Euclidian error in the reflection coefficient as a function of frequency, as expressed in (1). The standard flange has the largest amplitude error due to the strong edge reflections and a shorter electrical distance between the aperture and the flange edges (as compared to that of the large flange). The error for all flanges undulates across frequency due to phase variations in the reflected waves. The error associated with the rounded flanges, in general, have smaller amplitudes and less variation, as expected. In addition, the large rounded flange is shown to produce smaller errors than the small rounded flange, except at the lower edge of the frequency band (for this particular case).
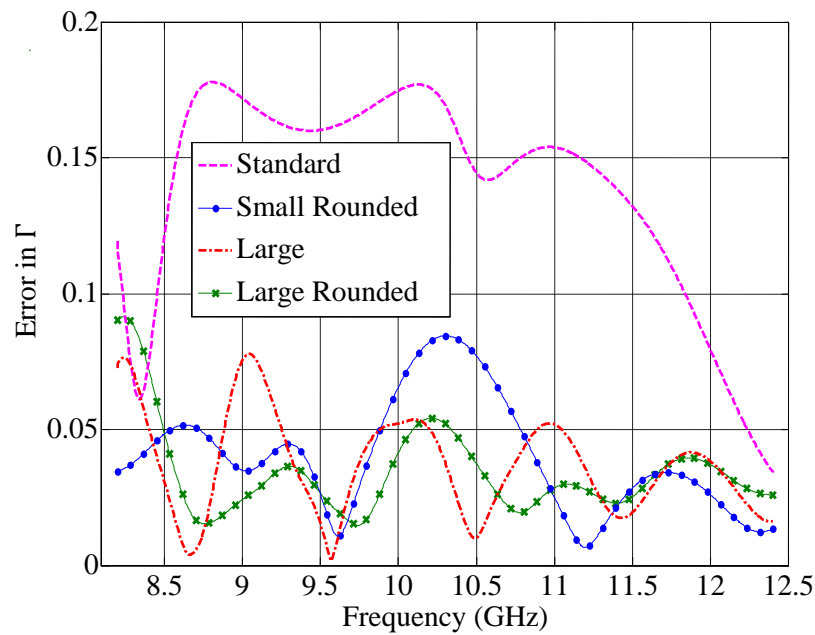
Figure 5.12. Error in the simulated reflection coefficient shown in Figure 5.11 plotted versus frequency.

The optimization technique outlined in Section 2 was used to estimate the complex dielectric constant from the reflection coefficient data in Figure 5.11. Figure 5.13 shows the estimated complex dielectric constant calculated from the simulated data, as a function of frequency. The results show that the standard flange introduces significant errors in the estimation of the relative permittivity and loss factor, as expected. This error is larger in estimating the loss-factor, as is also reported in [28]. Modifying the flange geometry reduces these errors and produces closer estimations of the relative

permittivity and the loss factor. The large rounded flange produces the most accurate estimation of the complex dielectric constant; with the exception of the first 100 MHz of the band. This corresponds to the peak in the Euclidian error, shown in Figure 5.12. Due to the complex relationship between the desired material properties (electrical and geometrical), the operating frequency, and the reflection coefficient, it can be seen in Figure 5.13 that the error in the estimated relative permittivity and loss factor is not necessarily proportional.
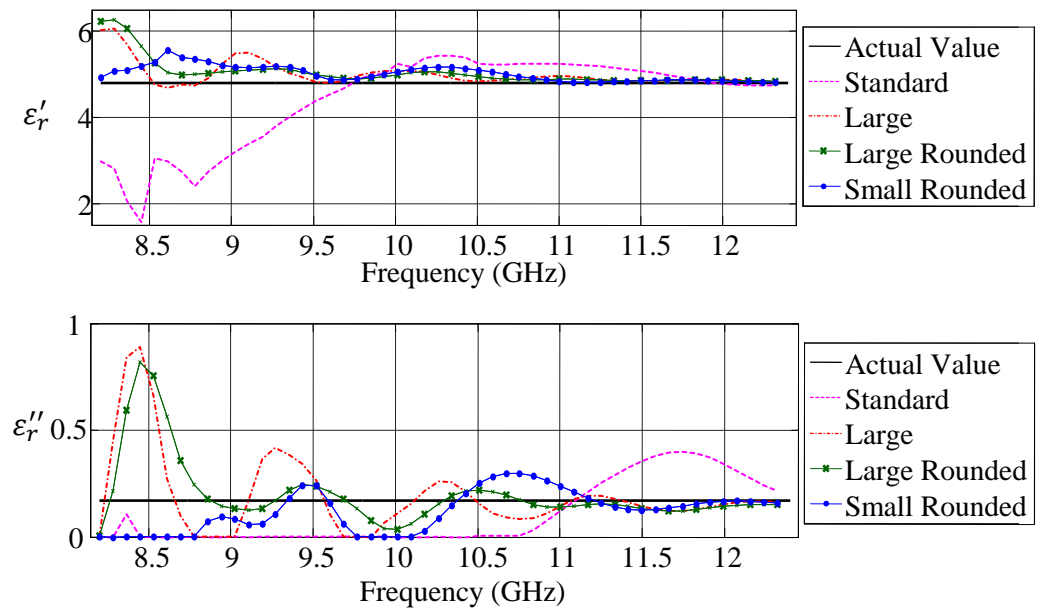
Figure 5.13. Calculated complex dielectric constant for various flange configurations for a conductor-backed dielectric sheet with $\varepsilon_r = 4.8 - j0.17$

5.6. MEASUREMENTS USING MODIFIED FLANGE

To verify the simulation results, four open-ended waveguide probes with the aforementioned flange geometries were constructed, as shown in Figure 5.14. These waveguide probes were used to evaluate the dielectric properties of the same rubber compound used in the simulations described above along with other samples.

(a)

(b)

(c)

(d)
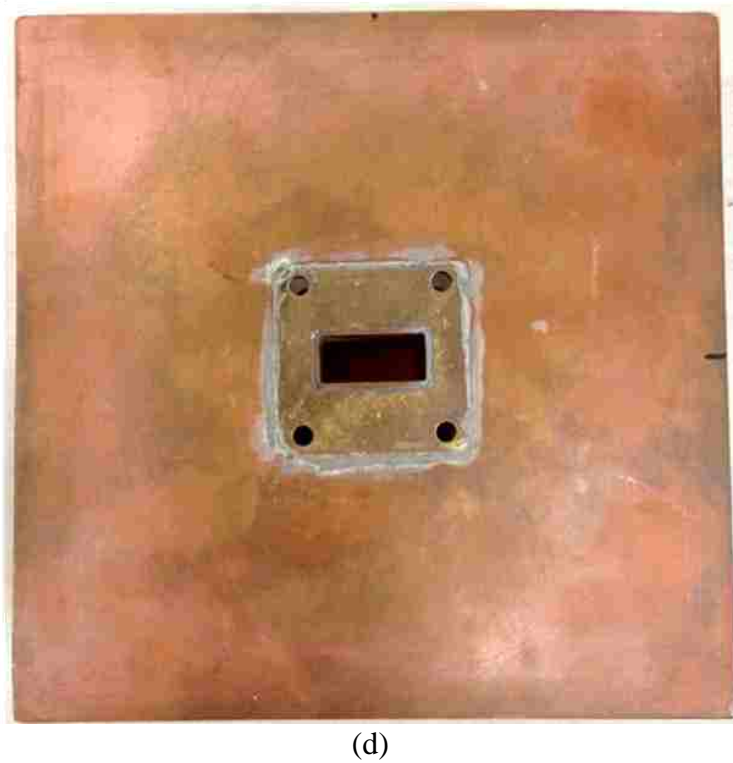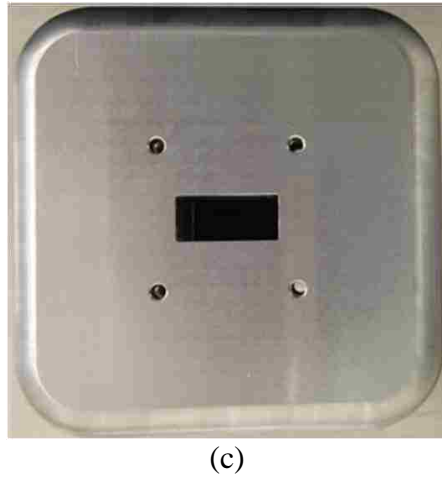
Figure 5.14. Flange geometries used for X-band measurements: (a) standard flange (40 mm x 40 mm), (b) small rounded flange ($F_x = F_y = 60$ mm) with rounded edges of radius 10 mm, (c) large flange (152 mm x 152 mm), (d) large rounded flange ($F_x = F_y = 100$ mm) with rounded edges of radius 10 mm.

Measurements of the reflection coefficient at the aperture of the open-ended waveguides were performed at X-band (8.2-12.4 GHz) using an Agilent 8510C VNA.

5.6.1. Complex Dielectric Constant Evaluation of a Conductor-Backed Rubber Sheet. Figure 5.15 shows the measured vector reflection coefficients plotted on the complex plane. As was seen in simulation, the standard small flange produces the largest errors in the measurement. The large flange follows the reflection coefficient of an infinite flange more closely, and, finally, the flanges with rounded edges produce a smooth reflection coefficient more closely matching the simulated infinite flange curve. It is important to note that all four of the measured complex reflection coefficients closely follow the corresponding simulated ones, as shown in Figure 5.11. In general, for the two rounded flanges (particularly the large one), measurement very closely matches the simulated results obtained by the infinite flange. Slight deviations from the simulated values for the infinite flange are attributed to measurement-related issues.
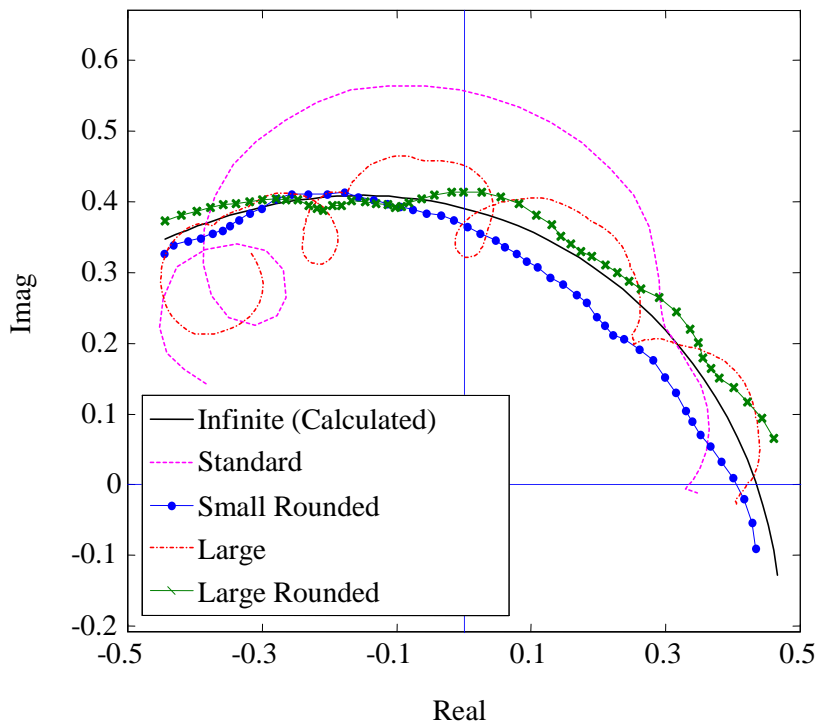
Figure 5.15. Measured vector reflection coefficient of conductor-backed 3.175 mm-thick dielectric sheet with $\varepsilon_r = 4.8 - j0.17$.

The measured data shown in Figure 5.15 was used to estimate the relative permittivity and loss factor of the dielectric sheet. The calculated data can be seen in Figure. 5.16. Once again, the rounded flanges provide increasingly accurate relative permittivity estimates. The worst case error of 18% for a standard flange was improved to approximately 2% for both rounded flanges. In addition, even though the estimated loss factors have significantly higher error margins with respect to the actual value, the rounded flanges provided much improved results compared to the non-rounded small and large flanges. It can be seen that the large rounded flange provides the best loss factor estimate, as is expected since it best approximates the fields of an infinite flange. However, it is known that this technique is not as accurate for measuring loss factor, when compared to permittivity, and typically overestimates loss factor values [28]. Once again, the results from the measurements follow those obtained in simulation (see Figure 5.13).
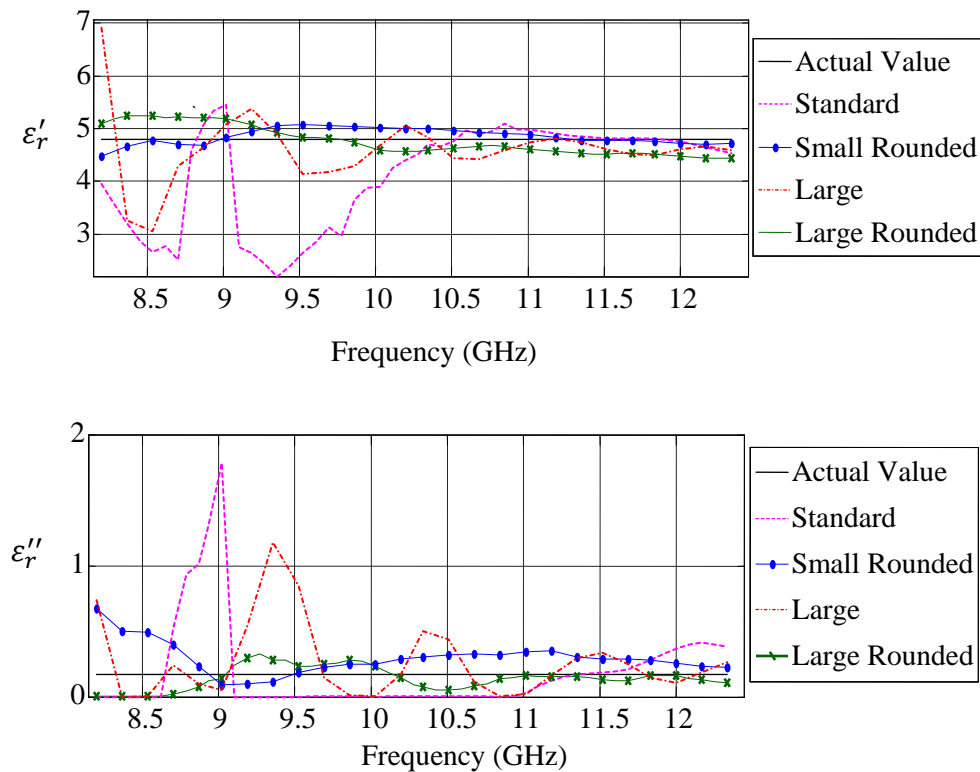
Figure 5.16. Calculated complex permittivity values for the measured reflection coefficients seen in Figure 5.15.

5.6.2. Complex Dielectric Constant Evaluation of a Conductor-Backed Acrylic Sheet (Low Loss). To provide an additional conductor-backed example that has proven to be difficult to measure due to its low loss properties, a conductor-backed acrylic (plexiglass) sheet was evaluated. Using the completely-filled waveguide technique [8], [19] and reported in [28], the dielectric constant of the 11 mm-thick Plexiglas material was evaluated to be $\varepsilon_r = 2.6 - j0.02$. The complex dielectric constant evaluated from the completely-filled waveguide technique showed little variation as a function of frequency and consequently, was assumed to be constant. Due to the lower permittivity than the previous rubber material that was evaluated, the electrical dimensions of the waveguide flanges are reduced by a factor of approximately 35%. In addition, the loss factor has been reduced by approximately 8.5 times. Using the large standard flange as well as the large rounded flange, the complex dielectric constant was evaluated at 51 frequency points. The resulting permittivity and loss factor values can be seen in Figure 5.17. Once again the rounded flange is shown to provide a more accurate estimation of both the permittivity and the loss factor values, although the errors associated with the loss factors is much greater.
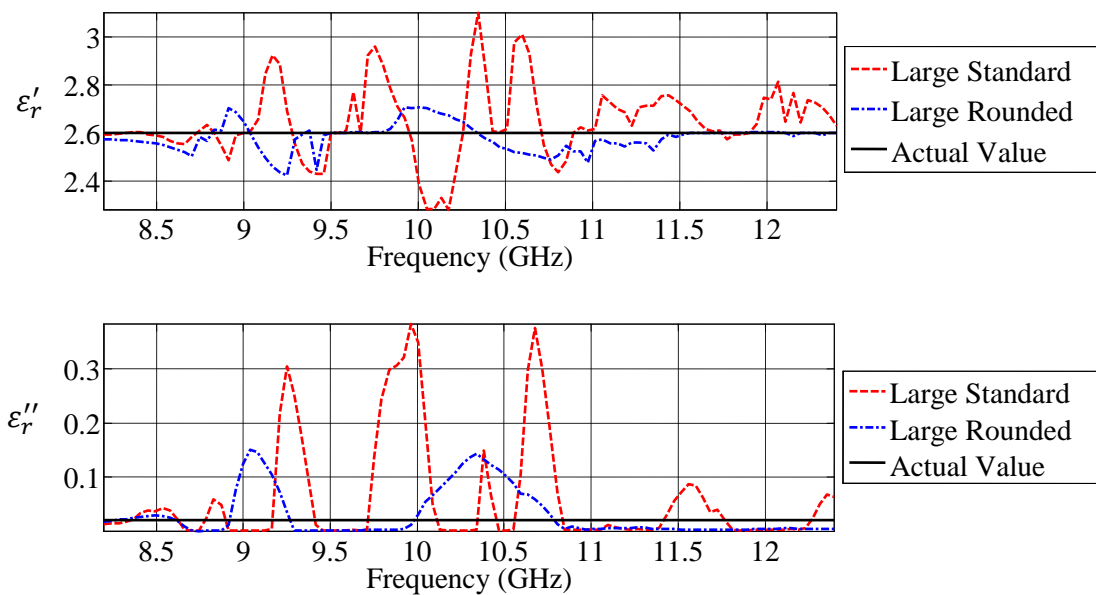
Figure 5.17. Evaluated complex dielectric constant of a low-loss acrylic sheet.

5.6.3. Complex Dielectric Constant Evaluation of an Air-Backed Stratified Composite Structure. A valuable characteristic of this technique is its nondestructive nature in evaluating material characteristics. Consequently, this technique lends itself well to structural health monitoring of stratified composites. Therefore, a stratified composite structure was evaluated using the previously described small-rounded edge waveguide probe. The structure contained five layers: three layers of glass fiber reinforced polymers (GFRP) separated by two identical low-density, low-permittivity paper honeycomb layers. The small rounded probe was chosen because this composite structure was backed by an infinite air half-space. The completely-filled waveguide technique [8] was used to evaluate the dielectric properties of the GFRP layers (used as the measured ground-truth data). These values were used as the initial guess for the forward-iterative optimization technique. Due to the brittle composition of the paper honeycomb, accurate loaded waveguide measurements were not possible. Consequently, it was assumed that the honeycomb layers would have a relative permittivity near unity, and a very small loss-factor. The assumption of using the actual value of the GFRP layers as the initial guess value is justified since for structural health monitoring purposes the goal is to detect changes in the material properties of a stratified composite whose ideal characteristics are assumed to be known.

Ten reflection coefficient measurements of this stratified structure were conducted and the complex dielectric constant of all five layers was simultaneously estimated. In addition, when evaluating a large number of parameters (10 parameters in this example), the system of equations becomes severely under-determined. Subsequently, the complex dielectric constant was assumed to be constant as a function of frequency. This allows the frequency diversity of the measurement to be exploited, which makes the multiple-parameter evaluations more robust. This assumption is acceptable for this structure, because, it has been shown that the dielectric constant of low-loss materials is quite constant as a function of frequency [41].

The calculated complex dielectric constant values for each of the five layers, along with two standard deviations (i.e. 95% confidence interval) are listed in Table 3. Even though all three GFRP layers were essentially identical in dielectric properties, given their relative locations within the stratified composite and slight variations in their

properties (i.e., slight thickness variation) as a function of multiple measurements, their recalculated permittivity values are not expected be identical. However, considering the standard deviation associated with the recalculated dielectric constants for the GFRP layers, these values are for all practical purposes (statistically) identical. Similarly, the relative permittivity of the honeycomb layers is nearly identical. The loss factor calculated for the honeycomb layers is below the dynamic range of this technique and therefore do not have practical value beyond agreeing with the original low loss assumption.

Table 5.3 Estimated complex dielectric constant values of the stratified composite structure.

Layer	Loaded Waveguide Actual ε_r	Actual Thickness (mm)	Estimated ε_r
Layer1	$3.0 - j0.025$	0.76	$(3.03\pm0.05) - j(0.023\pm0.009)$
Layer 2	-	4.95	$(1.15\pm0.007) - j(9E\text{-}5\pm1E\text{-}5)$
Layer 3	$3.0 - j0.025$	1.30	$(3.04\pm0.13) - j(0.025\pm0.001)$
Layer 4	-	4.95	$(1.23\pm0.01) - j(1E\text{-}4\pm1E\text{-}5)$
Layer 5	$3.0 - j0.025$	0.62	$(3.07\pm0.16) - j(0.027\pm0.013)$

5.7. CONCLUSION

A modification to the standard waveguide flange has been introduced that markedly improves the accuracy capabilities of the open ended waveguide technique for material characterization. First, the standard waveguide flange was modified by adding circular extensions to the two flange edges that generate the largest reflected fields. In order to improve upon this flange, all four edges of the waveguide flange were rounded with generally elliptical cross-sections. By rounding all four edges of the waveguide flange, the electric field distribution around the waveguide aperture as well as the induced surface currents on the flange much more closely match those of an infinite flange. In addition, by adding a generally elliptical cross section to the flange edges, an ideal geometry may be designed for a specific application. The axial ratio of the ellipse that is

employed is dependent upon the properties of the sample and should be designed accordingly.

Most importantly, by modifying the flange geometry the accuracy by which material properties may be evaluated is significantly improved. This improvement is most notable for low loss, thin, and conductor-backed samples which have generally proven difficult to measure. The flange modifications presented here have been shown in both simulation and measurement to surpass the accuracy of a custom flange whose footprint requires significantly larger area. By rounding the edges of the waveguide flange, the reflections generated at the flange edges have been significantly reduced. Consequently, the electric field around the probe more accurately matches that of an infinite flange which, in turn, allows for material properties to be evaluated with much improved accuracy.

6. SUMMARY AND FUTURE WORK

6.1. BACKGROUND

The open-ended waveguide technique has proven to be versatile and applicable to many NDT applications when dealing with stratified (layered) composite structures. The major benefits of this technique are its non-invasive nature, simple measurement setup, and ability to simultaneously evaluate the material properties (e.g. complex dielectric constant and/or layer thickness) of multiple layers in a stratified composite. Recently, an electromagnetic model that accounts for higher-order modes generated at the waveguide aperture has been developed and was briefly described in Section 2. Accounting for these higher-order modes has shown to improve the accuracy by which material properties may be evaluated [28]. The goal of this thesis was to investigate the additional sources of inaccuracy in evaluating material properties, starting with measurement system noise. However, it was shown that the primary source of errors is due to the reflected fields generated by the finite-sized waveguide flange that is used in measurements.

6.2. SYSTEM NOISE

In Section 3, the effect of system noise, which contaminates the measured reflection coefficient, on the evaluated material properties was investigated. In order to do so, simulations were developed that estimate the uncertainty a specified level of noise power introduces into the evaluated material properties. This was accomplished by using the electromagnetic model to calculate the exact reflection coefficient for a given dielectric structure and operating frequency. Next, noise adhering to a complex Gaussian distribution was injected into the exact reflection coefficient to simulate the noise introduced by a measurement system. Finally, the desired material properties were evaluated using the iterative procedure detailed in Section 2. The results of these simulations showed that the uncertainty introduced by the measurement system is a function of the material properties as well as the operating frequency. In addition, the uncertainty in the permittivity was generally quite small, with respect to the nominal

value. However, the loss factor showed large uncertainty values, rendering its measurement mostly ineffective.

To verify these simulations, measurements were performed using an Agilent 8510C VNA. By cascading a variable attenuator between the VNA port and the open-ended waveguide, the noise-floor of the 8510C VNA could be manipulated. When the attenuation was increased, the signal power available at the open-ended waveguide was decreased. Consequently, the power in the reflected signal would also be decreased while the sensitivity of the VNA receiver remained unchanged. As a result, the noise floor of the measurement system could be controlled. It was shown that the measured noise floor of the 8510C VNA was be comparable to the noise levels approximated in the simulations. However, the measured reflection coefficient was seen to strongly deviate from the reflection coefficient predicted by the electromagnetic model. These deviations were observed to be deterministic as they were consistently present in multiple measurements as well as for multiple calibrations. Moreover, the evaluated material properties were shown to deviate well beyond the uncertainty bounds generated from the simulation procedure. These deviations were due to the reflections generated at the edges of the finite-sized flange that was employed. These reflected fields are not accounted for in the electromagnetic model which assumes the waveguide to be terminated into an infinite flange.

A comparison between the 8510C VNA and an in-house built VNA with a non-coherent detection scheme was also presented in Section 3. Due to the architecture of the in-house built VNA, the noise performance was sacrificed for an economical and compact design. Four different dielectric structures were measured with both systems and the complex dielectric constants were evaluated. The dielectric structures that were chosen to be measured were high in loss so that the effects of the finite-sized flange could be negated (strong attenuation for any fields that propagate to and from the flange edges). It was shown that, in general, the two systems were in good agreement in their dielectric constant estimations. However, the noisier in-house built VNA consistently produced material estimations with larger standard deviations than the 8510C. Regardless, it was shown that for open-ended waveguide measurements, the more economical choice provided results that were quite similar to the expensive 8510C VNA.

6.3. EVALUTION OF THE FINITE FLANGE

In Section 4 the effect of the finite-sized waveguide flange was further evaluated. Using CST simulations it was shown that both air and conductor-backed structures have wave guiding properties. Air-backed dielectric sheets were shown to support surface waves along the flange while the conductor-backed structure operated as a parallel plate waveguide. Both of these configurations were shown to guide the electromagnetic energy toward the edge of the finite-sized flange where a reflected field was generated. The reflected field is due to a wave impedance mismatch between the guided fields and those radiating away from the flange where the guiding structure is no longer present.

In addition, the effect of material properties on these guided fields was evaluated. It was shown that the errors introduced in the reflection coefficient by the finite-sized flange were strongest for low loss materials. This can be attributed to the fact that higher loss materials attenuate the fields that reach and are reflected from the flange edges. Similarly, increasing the flange dimensions typically improves the accuracy of the measured reflection coefficient, although this improvement is not monotonic with respect to flange size. Increasing the flange dimensions requires the guided fields to travel a longer electrical distance and to incur more attenuation. However, due to the unique interference pattern that is a function of the flange dimensions, the material properties, and the operating frequency, the increased flange size does not ensure the reflected fields will have a decreased effect on the overall electric field at the location of the waveguide aperture.

6.4. MODIFICATIONS TO THE FINITE FLANGE

Finally, Section 5 introduced a novel waveguide probe that was designed to remove the discontinuity introduced by the finite-sized waveguide flange. The goal of this probe was to emulate the electric field distribution as well as the surface current density of a waveguide terminated in an infinite flange. The solution presented here replaced the standard 90° flange edges with a generally elliptical cross section. The resulting elliptical edges operate as a wave impedance transformer, helping to better

match the wave impedance of the guided fields with those propagating away from the waveguide. Simulated data using CST was presented and showed that this flange modification allowed the surface current density as well as the electric field distribution in front of the flange to much more closely emulate those of an infinite flange. In addition, an optimal axial ratio of the elliptical edges is possible which minimizes the RMS error in the reflection coefficient (as a function of frequency). However, this optimum axial ratio is dependent on the properties of the material being evaluated. When the edges have an axial ratio of 1 (i.e. a circular cross-section) the errors in the reflection coefficient are seen to monotonically decrease as the edge radius is increased. Like the standard flange, increasing the lateral dimensions of the flange typically improves the performance, although it is not a monotonic improvement. This is due to the unique interference patterns generated in front of the waveguide flange due to the fields reflected from the flange edges.

Finally, the advantages of rounding the flange, as were seen in simulated data, were confirmed via measurements. Two waveguides with modified rounded flanges were machined and used to make reflection coefficient measurements. These measurements were compared with a standard waveguide flange as well as a custom, large waveguide flange that had standard 90° edges. The two flanges with rounded edges were shown to consistently measure the reflection coefficient more accurately (with respect to that calculated by the electromagnetic model). Consequently, the rounded flanges provided significantly more accurate estimations of the material characteristics. In addition, the evaluated material characteristics exhibited a markedly reduced standard deviation. By rounding the edges of the waveguide flange, the electric field distribution in front of the finite-sized waveguide flange much more closely mimics that of an infinite flange, allowing for more accurate reflection coefficient measurements. Consequently, since the measurement setup is more accurately described in the electromagnetic model, the accuracy by which material properties are characterized is significantly improved.

6.5. FUTURE WORK

The novel waveguide probe presented here has many aspects which may be refined and tuned to achieve the best possible performance. First, it was shown in Section

5 that the electromagnetic fields which are radiated away from the flange are assumed to propagate away from the flange without any mechanism to scatter/reflect the fields back toward the aperture. However, in practice, it is quite likely that objects will be near the waveguide probe or discontinuities in the sample (e.g. sample edges or curvature) may generate reflections. Consequently, an absorbing material may be employed near the rounded flange edges to dissipate the radiated fields near the waveguide probe before they reach a scattering/reflecting discontinuity.

Next, it was stated in Section 5 that the modified edge geometry was assumed to be identical on all four edges as well as symmetric on the front (plane of the aperture) and back (location were feeding waveguide meets the flange) of the waveguide flange. However, in order to minimize the dimensions and tune the waveguide flange for a specific application, these conditions may be relaxed. For instance, the edges on the back of the waveguide flange play a reduced role in the operation of the modified flange (shown by the fact that the surface current density on the back of the flange has considerably lower amplitude when compared to the front). Consequently, the most effective probe geometry may have more gradual edges on the front of the flange than on the back of the flange. Simply stated, the volume the flange occupies may be more efficiently used if the rounded edges are not assumed to all be identical.

Other flange modifications such as a choke on the back of the flange to prevent surface currents or corrugating the rounded edges (increase their effective dimensions) may provide additional performance improvements. However, any additional flange modification is expected to provide marginal improvements as the impedance transformation the rounded edges introduce eliminate the most significant reflected fields.

APPENDIX

Matlab Code

A.1 INTRODUCTION

This appendix contains examples of the Matlab® programs detailed in this thesis. The object, *nlayer*, that is used in the noise simulations contains the solver for the electromagnetic model [28] as created by Dr. Mohammad T. Ghasr and refined by Dr. Toby Case. The program outlining the procedure to control CST via Matlab® has been generalized but could be employed with an arbitrary number of for loops to step multiple parameters through an arbitrary number of values.

A.1.1 Matlab Script for Evaluating Uncertainty Introduced by Measurement Noise.

```matlab
clear all; close all; clc;

% Set number of frequencies and noise power in dB
NF = 21;
NoisePower = [-50]

% Convert dB noise power to linear
NP = 10.^(NoisePower./10);

% Define layer(s) whose properties are to be evaluated
Layer = [1];

% Set start and stop frequencies in GHz
F_Start = 8.2;
F_Stop = 12.4;

% Set permitivity and loss tangent(s)
Erp = 5;
tand = [0.2];

% Set Thickness(es) as fraction of mid-band wavelength in material
Thickness = [0.25]

% Calculate mid-band wavelength in mm
Lambda = 3e11/((F_Start+(F_Stop-F_Start)/2)*1e9*sqrt(Erp));
Thickness = [0.25]*Lambda

% Set convergence tolerance for permittivity (delta mean and delta
% standard deviation)

meantol = 0.005*Erp
stdtol = 0.005*Erp
```

```matlab
% Set minimum number of trials
mintrials = 480

% Set number of consecutive trials that must pass convergence
% criteria AFTER the minimum number of trials has been satisfied.
numconvergecheck = 20

%Set NLayer convergence criteria
NL_ConergeTestTol = 1e-3;

% Set fminsearch tolerances and maximum number of
%iterations/evaluations.
opt = optimset('TolFun',1e-6,'TolX',1e-6,'Display','iter',...
               'MaxIter',1e3,'MaxFunEvals',1e3);


% Define Frequency vector
F =  linspace(F_Start,F_Stop,NF);

% Generate noise to add to S11
rnoise = sqrt(NP/2).*randn(NF,1)+1i*sqrt(NP/2).*randn(NF,1);

% Set trial counter to 1.
iT = 1;

% For loop to set through thicknesses (if vector)
for iTK = 1:length(Thickness)


    % For loop to set through loss tangents (if vector)
    for iTD = 1:length(tand)

        % Define Nlayer object with specified parameters and 6 modes.
        NL = nlayer('x',F,[Erp-1i*Erp*tand(iTD)],[Thickness(iTK)],3,2);

        % Set starting value for # of Gaussian Intergration points.
        NL.DesiredNumRho = 100;
        NL.ConvergeTestTol = NL_ConergeTestTol;

        % Run NLayer convergence test.
        NL.ConvergeTest();

        % Store number of Gaussian Intergration points required for
        %convergence.
        NL_NumRho(iTK,iTD) = NL.DesiredNumRho;

        % Store the calculated reflection coefficient.
        ActualRef(:,iTK,iTD) = NL.CalcRef();

        % Plot calculated reflection coefficient on complex plane.
        figure()
        plot(ActualRef)
```

```matlab
hold on
zplane([])

% For loop to set noise power (if vector)
for iN = 1:length(NoisePower)

    % Clear the exit flag
    exitflag = 0;

    % Clear the convergence counter
    convergecounter = 0;

    % While loop for convergence of results.
    while (exitflag ~= 1)

        % Create complex noise vector for specific trial.
        rnoise = sqrt(NP(iN)/2).*randn(NF,1)...
            +1i*sqrt(NP(iN)/2).*randn(NF,1);

        % Store noise vector to it is accessible
        %after simulations.
        noise(:,iT,iTK,iTD,iN) = rnoise;

        % Contaminate actual ref. coefficient with noise.
        NoiseRef(:,iT,iTK,iTD,iN) = ActualRef(:,iTK,iTD)...
            +noise(:,iT,iTK,iTD,iN);

        % Create NLayer object and make it identical to
        % that which was used to calculate the
        %actual ref. coef.
        NL = nlayer('x',F,[Erp-1i*Erp*tand(iTD)],...
                                    [Thickness(iTK)],3,2);
        NL.DesiredNumRho = NL_NumRho(iTK,iTD);

        % Find the complex dielectric constant with noisy
        % Reflection coefficient as the given ref.
        NL.FindErF(NoiseRef(:,iT,iTK,iTD,iN),1,[1,1],opt)

        % Store the evaluated dielectric constant.
        Er(:,:,iT,iTK,iTD,iN) = NL.Er;

        % Clear object for next trial.
        clear NL

        % Create temporary matrix containing Complex
        % dielectric value from every trial.
        clear tempEr
        tempEr = squeeze(Er(:,1,1:1:iT,iTK,iTD,iN));

        % Calculate average and Std of permittivity for each
        % frequency across the trials.
        meanEr(:,iT,iTK,iTD,iN) = mean(real(tempEr),2)
        stdEr(:,iT,iTK,iTD,iN) = std(real(tempEr),0,2)
```

```matlab
            % Plot the average and std permittivity values for
            % each trial iteration.
            figure(2)
            subplot(2,1,1)
            plot(linspace(1,iT,iT),squeeze(...
                meanEr(:,1:1:iT,iTK,iTD,iN)),'o-')

            subplot(2,1,2)
            plot(linspace(1,iT,iT),squeeze(...
                stdEr(:,1:1:iT,iTK,iTD,iN)),'o-')

            % Plot the current uncertainity errorbars for
            % permittivity
            figure(3)
            errorbar(F,real(meanEr(:,iT)),std(real(squeeze(...
                Er(:,1,:))),0,2)*3,...
                -3*std(real(squeeze(Er(:,1,:))),0,2))
            drawnow;

            % If mintrials are reached, check convergence
            % criteria and make appropriate update
            % to check flags.
            if (iT>=mintrials)
                deltamean(:,iT,iTK,iTD,iN) = abs(...
                    meanEr(:,iT,iTK,iTD,iN)-...
                    meanEr(:,iT-1,iTK,iTD,iN))

                deltastd(:,iT,iTK,iTD,iN) = abs(...
                    stdEr(:,iT,iTK,iTD,iN)-...
                    stdEr(:,iT-1,iTK,iTD,iN))

                if ((deltamean(:,iT,iTK,iTD,iN) <= meantol)...
                        &(deltastd(:,iT,iTK,iTD,iN) <= stdtol))

                    convergecounter = convergecounter + 1;
                else
                    convergecounter = 0;
                end

                if (convergecounter > numconvergecheck)
                    exitflag = 1;
                end

            end

            % Increment the trial counter.
            iT = iT+1;

        end

    % Clear the trial counter.
    iT = 1;

    % Save the current data.
```

```matlab
        save('NoiseSensitivity_Erp5_CB3Lossy.mat')
        end
    end
end
```

A.1.2 Example of Controlling CST via a COM Server

```matlab
clear all; close all; clc;

% CST Model Filename
CSTFile = 'Filename_of_CST_model.cst');

% Filename for S-Parameters
SParameterFile 'Filename_for_SParameters.s1p');

% Set values for CST parameters that should be changed.
CST_Parameter1_Value = 1.000;
CST_Parameter1_Value = 22.86;

% Open CST via COM Interface
cst = actxserver('CSTStudio.Application');

% Open specified CST Project
project = cst.invoke('OpenFile',CSTFile);

% Using current project, create solver object
solver = project.invoke('FDSolver');

% Define results object for Touchstone (.s1p)
results = project.invoke('TOUCHSTONE');

% Do not renomalize S-Parameters to 50 Ohms
results.invoke('Renormalize','False');

% Using project object, update necessary parameter values
project.invoke('StoreParameter','CST_Parameter1',CST_Parameter1_Value);
project.invoke('StoreParameter','CST_Parameter2',CST_Parameter2_Value);

% Rebult CST Model to update the parameters.
project.invoke('Rebuild');

% Start simulation with settings defined in CST Model. These settings
% are the frequencies, adaptive meshing settings, convergence critera,
etc.
solver.invoke('Start');

% When simulation is finished, set location for exporting S-Parameters.
results.invoke('Filename',SParameterFile);

% Export S-Parameters to location set in previous step.
results.invoke('Write');
```

BIBLIOGRAPHY

[1]   S. Ganchev, N. Qaddoumi, E. Ranu and R. Zoughi, "Microwave Detection Optimization of Disbond in Layered Dielectrics with Varying Thicknesses," *IEEE Transactions on Instrumentation and Measurement*, vol. IM-44, no. 2, pp. 326-328, April, 1995.

[2]   S. Bakhtiari, S. Ganchev, N. Qaddoumi and R. Zoughi, "Microwave Non-Contact Examination of Disbond and Thickness Variation in Stratified Composite Media," *IEEE Transactions on Microwave Theory and Techniques*, vol. 42, no. 3, pp. 389-395, March, 1994.

[3]   V. Teodoris, T. Sphicopoulos, and F. E. Gardiol, "The reflection from an open-ended waveguide terminated by a layered dielectric medium," *IEEE Trans. Microwave Theory Tech.,* vol. MTT-33, pp. 359–366, May 1985.

[4]   R. H. MacPhie and A. I. Zaghloul, "Radiation from a rectangular waveguide with infinite flange-exact solution by the correlation matrix," *IEEE Transactions on Antennas Propagation*, vol. AP-28, pp. 497–503, July 1980.

[5]   M. Abou-Khousa, and R. Zoughi, "Disbond Thickness Evaluation Employing Multiple-Frequency Near-Field Microwave Measurements," IEEE Transactions on Instrumentation and Measurement, vol. 56, no. 4, pp. 1107-1113, August 2007.

[6]   S. Kharkovsky, A.C. Ryley, V. Stephen and R. Zoughi, "Dual-Polarized Near-Field Microwave Reflectometer for Non-Invasive Inspection of Carbon Fiber Reinforced Polymer (CFRP)-Strengthened Structures," *IEEE Transactions on Instrumentation and Measurement*, vol. 57, no. 1, pp. 168-175, January 2008.

[7]   C-W. Chang, K-U. Chen and J. Qian, "Nondestructive Determination of Electromagnetic Parameters of Dielectric Materials at X-band Frequencies Using a Waveguide Probe System," *IEEE Transactions on Instrumentation and Measurement*, vol. 46, no. 5, pp. 1084-1092, October 1997.

[8]   K. Bois, L. Handjojo, A. Benally, K. Mubarak and R. Zoughi, "Dielectric Plug-Loaded Two-Port Transmission Line Measurement Technique for Dielectric Property Characterization of Granular and Liquid Materials," *IEEE Transactions on Instrumentation and Measurement,* vol. 48, no. 6, pp. 1141-1148, December 1999.

[9]   A. Sivohla, *Electromagnetic Mixing Formulas and Applications*. IEE Electromagnetic Series 47, 1999.

[10]   F. T. Ulaby, R. K. Moore, and A. K. Fung, *Microwave Remote Sensing: Active and Passive*. Dedham, MA: Artech House, 1986, vol. 3, pp. 2017–2025.

[11]   S. Gray, S. Ganchev, Qaddoumi N., G Beauregard, D. Radford and R. Zoughi, "Porosity Level Estimation in Polymer Composites Using Microwaves," *Materials Evaluation*, vol. 53, no. 3, pp. 404-408, March, 1995.

[12]   M. Ghasr, S. Kharkovsky, R. Zoughi and R. Austin, "Comparison of Near-Field Millimeter Wave Probes for Detecting Corrosion Precursor Pitting under Paint," *IEEE Transactions on Instrumentation and Measurement*, vol. 54, no. 4, pp. 1497-1504, August 2005.

[13]   N. Qaddoumi, A. Shroyer and R. Zoughi, "Microwave Detection of Rust Under Paint and Composite Laminates," *Research in Nondestructive Evaluation*, vol. 9, no. 4, pp. 201-212, 1997.

[14]   Peer, S., J.T. Case, E. Gallaher, K.E. Kurtis and R. Zoughi, "Microwave reflection and Dielectric Properties of Mortar Subjected to Compression Force and Cyclically Exposed to Water and Sodium Chloride Solution," *IEEE Transactions on Instrumentation and Measurement*, vol. 52, no. 1, pp. 111-118, February 2003.

[15]   Case, J.T., S. Peer, and R. Zoughi, "Microwave Reflection Properties of Concrete Periodically Exposed to Chloride Solution of 3% Salinity and Compression Force," *IEEE Transactions on Instrumentation and Measurement*, vol. 53, no. 4, pp. 1000-1004, August 2004.

[16]   Peer, S., K.E. Kurtis and R. Zoughi, "An Electromagnetic Model for Evaluating Temporal Water Content Distribution and Movement in Cyclically Soaked Mortar," *IEEE Transactions on Instrumentation and Measurement*, vol. 53, no. 2, pp. 406-415, April 2004.

[17]   Peer, S. and R. Zoughi, "Comparison of Water and Saltwater Movement in Mortar Based on a Semi-Empirical Electromagnetic Model," *IEEE Transactions on Instrumentation and Measurement*, vol. 53, no. 4, pp. 1218-1223, August 2004.

[18]   Balanis, Costantine A. *Advanced Engineering Electromagnetics*. 2nd ed. Hoboken, NJ: Wiley John & Sons Limited Distribution Center, 2012. Print.

[19]   J. Baker-Jarvis, M. D. Janezic, J. H. Grosvenor, and R. G. Geyer, "Transmission/reflection and short-circuit line method for measuring permittivity and permeability," NIST Tech. Note 1355-R, U.S. Dept. Commerce, Boulder, CO, pp. 52-57, December 1993.

[20]   E.J. Vanzura, J. Baker-Jarvis, J. H. Grosvenor, and M. D. Janezic, "Intercomparison of permittivity measurements using the transmission/reflection method in 7-mm coaxial transmission lines" *IEEE Transactions on Microwave Theory and Techniques,* vol.42, no.11, pp.2063-2070, Nov. 1994.

[21]   J. Baker–Jarvis, C. Jones, B. Riddle, M. Janezic, R. G. Geyer, J. H. Grosvenor, Jr., and C. M. Weil, "Dielectric and magnetic measurements: A survey of nondestructive, quasinondestructive, and process-control techniques," *Res. Nondestruct. Eval*., vol. 7, pp. 117–136, Aug. 1995.

[22]   K. J. Bois, A. D. Benally, and R. Zoughi, "Multimode solution for the reflection properties of an open-ended rectangular waveguide radiating into a dielectric half-space: the forward and inverse problems." *IEEE Transactions on Instrumentation and Measurement,* vol. 48, no. 6, pp. 1131-1140, December 1999.

[23]   Krupka, Jerzy. "Frequency Domain Complex Permittivity Measurements at Microwave Frequencies." *Measurement Science and Technology* 17.6 (2006): R55-70.

[24]   Ghodgaonkar, D.K.; Varadan, V.V.; Varadan, V.K., "Free-space measurement of complex permittivity and complex permeability of magnetic materials at microwave frequencies," *Instrumentation and Measurement, IEEE Transactions on* , vol.39, no.2, pp.387,394, Apr 1990.

[25]   Bakhtiari, S.; Ganchev, S.I.; Zoughi, R., "Analysis of radiation from an open-ended coaxial line into stratified dielectrics," *Microwave Theory and Techniques, IEEE Transactions on* , vol.42, no.7, pp.1261,1267, Jul 1994.

[26]   R. Zoughi, *Microwave Non-Destructive Testing and Evaluation*, Kluwer Academic Publishers, The Netherlands, 2000.

[27]   Tantot, O.; Chatard-Moulin, M.; Guillon, P., "Measurement of complex permittivity and permeability and thickness of multilayered medium by an open-ended waveguide method," *Instrumentation and Measurement, IEEE Transactions on* , vol.46, no.2, pp.519,522, Apr 1997.

[28]   M.T. Ghasr, D. Simms and R. Zoughi, "Multimodal Solution for a Waveguide Radiating into Multilayered Structures - Dielectric Property and Thickness Evaluation," *IEEE Transactions on Instrumentation and Measurement*, vol. 58, no.5, pp.1505-1513, May 2009.

[29]   M. Fallahpour, H. Kajbaf, M. T. Ghasr, J. T. Case and R. Zoughi, "Simultaneous Evaluation of Multiple Key Material Properties of Complex Stratified Structures with Large Spatial Extent," *Proceedings of Review of Progress in Quantitative Nondestructive Evaluation*, vol. 1430, AIP Conference Proceedings, edited by D.O. Thompson and D.E. Chimenti, American Institute of Physics, pp. 561-565, Melville, NY, 2011.

[30]   Kempin, M., M.T. Ghasr, and R. Zoughi, "Finite flange Correction for Microwave and Millimeter-Wave Nondestructive Material Characterization," *Proceedings of the IEEE International Instrumentation and Measurement Technology Conference* (I2MTC), pp. 1435-1440, Minneapolis, MN, May 6-9, 2013.

[31]   K. Yoshitomi, H.R. Sharobim, "Radiation from a rectangular waveguide with a lossy flange," *Antennas and Propagation, IEEE Transactions on* , vol.42, no.10, pp.1398,1403, Oct 1994.

[32]   Pozar, David M. *Microwave Engineering*. 3rd ed. Hoboken, NJ: J. Wiley, 2005. Print.

[33]   Lagarias, J. C., J. A. Reeds, M. H. Wright, and P. E. Wright, "Convergence Properties of the Nelder-Mead Simplex Method in Low Dimensions," *SIAM Journal of Optimization*, Vol. 9, Number 1, pp. 112–147, 1998.

[34]   Agilent Technologies, Appl. Note 1363-1, pp. 2-8.

[35]   Hughes, Ann J., and Dennis E. Grawoig. *Statistics: A Foundation for Analysis*. Reading, MA: Addison-Wesley Pub., 1971.

[36]   Abou-Khousa, M.A.; Baumgartner, M.A.; Kharkovsky, S.; Zoughi, R., "Novel and Simple High-Frequency Single-Port Vector Network Analyzer," *Instrumentation and Measurement, IEEE Transactions on* , vol.59, no.3, pp.534,542, March 2010.

[37]   N. Moade, S. Yong, Y. Jinkui, F. Chenpeng and X. Deming "An Improved Open-Ended Waveguide Measurement Technique on Parameters e_r and m_r of High-Loss Materials," *IEEE Transactions on Instrumentation and Measurement*, vol. 47, no. 2, pp. 476-481, April 1999.

[38]   CST - Computer Simulation Technology, http://www.cst.com.

[39]   Balanis, Constantine A. *Antenna Theory: Analysis and Design*. 3rd ed. Hoboken, NJ: Wiley Interscience, 2005.

[40]   D. F. Williams, M.T. Ghasr, B. Alpert, Z. Shen, A. Arsenovic, R. M. Weikle, II, and R. Zoughi, "Legendre Fit to the Reflection Coefficient of a Radiating Rectangular Waveguide Aperture," *IEEE Transactions on Antennas and Propagation,* vol.60, no.8, pp.4009-4014, Aug. 2012.

[41]   A. K. Jonscher, "Dielectric relaxation in solids", *Journal of Physics D: Applied Physics,* vol. 32, no. 14, pp.57 -70 1999.

VITA

Matthew Alan Kempin was born in Wichita, Kansas on January 24, 1989. He graduated from Trinity Academy in 2007 and received his Associates Degree in Liberal Arts from Des Moines Area Community College in 2009. Matthew received his Bachelors of Science degree in Electrical Engineering as well a Minor in Mathematics from Missouri University of Science and Technology in the fall of 2011. He graduated Summa Cum Laude.

In the spring of 2012, Matthew began his graduate studies at Missouri University of Science and Technology where he joined the Applied Microwave Nondestructive Testing Laboratory (amntl). His research was supported by a grant from the Department of Defense as well as the from Missouri University of Science and Technology Chancellor's Fellowship. Matthew received his Master's of Science degree in Electrical Engineering from Missouri University of Science and Technology in August of 2013.

Matthew was a member of Eta Kappa Nu and IEEE while at MS&T. He was also a member of the MS&T Miners baseball team in 2009-2010.